Theory and Applications of VHF Meteor Radar Observations

Joel P. Younger

Thesis submitted for the degree of
Doctor of Philosophy
in
Physics

Supervisors
Prof. Iain M. Reid and Prof. Robert A. Vincent
The University of Adelaide
School of Chemistry and Physics

submitted
25 October, 2011

Contents

Abstract

This thesis examines the operation and observations made by VHF interferometric radar. Broad topics include the operation of interferometric meteor radar, the physics of meteor ablation, the formation and diffusion of meteor trails, and meteor astronomy.

The performance of the basic radar configuration is examined with particular attention paid to the source and mitigation of positional errors introduced by hardware. Sources include random errors in phase and range estimates, mutual coupling between antennas, and biases in the phase measurements used to determine the angle-of-arrival of incident radiation. A new method for post-statistical steering is presented, using height dependent ambipolar diffusion coefficients as a reference.

The physics of meteor flight and ablation in the atmosphere is examined in detail. The heating and vaporization of meteoroids as they enter Earth's atmosphere is modeled and the effect of sputtering on the formation of meteor ionization is assessed. These calculations are performed for a variety of meteor types, sorted by velocity, angle-of-entry, composition, and size. The results are then used in conjunction with atmospheric models to produce predictions of meteor radar performance.

The effect of the atmosphere on the ablation and subsequent detection of meteors is considered and used to construct new metrics for the characterization of the atmospheric density profile in the meteor region. The effects of constant density level and density scale height are assessed with regards to the peak detection height and range of heights over which a radar detects meteors.

The formation of the underdense meteor echo is examined in detail. New contributions to the understanding of this topic include an assessment of the effects of variable electron line density in the trail, deceleration, and fragmentation on the eventual measurement of the decay time of meteor echoes. Estimates of ambipolar diffusion coefficients are examined by determining the effect of anomalous diffusion resulting from electron absorbing aerosols and multi-constituent trail chemistry.

Meteor astronomy techniques used to overcome the limitations of interferometric meteor radars are implemented in order to search for discrete streams of solar system debris that result in meteor showers. The results include a significant number of previously undiscovered shower systems.

I certify that this work contains no material which has been accepted for the award of any degree or diploma in any university or tertiary institution and, to the best of my knowledge, contains no material previously published or written by another person, except where due reference has been made in the text.

I give consent to this copy of my thesis, when deposited in the University of Adelaide Library, being made available for loan and photocopying, subject to the provisions of the Copyright Act of 1968.

I also give permission for the digital version of my thesis to be made available on the internet, via the University of Adelaide digital research repository, the University of Adelaide Library catalogue, the Australasian Digital Theses Program (ADTP) and through internet search engines.

Signed .... date ....

Joel P. Younger, BSc (Hons.)

Acknowledgments

The process that takes a graduate student from application to the submission of a thesis is one that cannot occur without the generous help and professional, emotional, and financial support of a huge number of people. I would be remiss if I did not take the opportunity to thank as many of them as possible, although I suspect that I will inevitably miss some in this brief note.

My supervisors during the last three and a half years, Professor Iain Reid and Professor Robert Vincent have provided the support, guidance, and freedom that I feel has enabled me to mature as a scientist, rather than simply accomplish the feat of writing a thesis. They have given me a degree of independence in my research that less confident supervisors might balk at, allowing me to focus on new and productive lines of inquiry. With their encouragement to undertake a PhD in the first place, careful contributions when I became lost, and tireless efforts to assist me in establishing a place in the broader scientific community, it has been a pleasure and an invaluable learning experience to be under their tutelage. Good bosses are rare. I have had two.

Perhaps most of all, my partner Josie deserves credit for the successful completion of this thesis, for putting up with me playing grad student when by all rights I should have been out getting a real job. She has put up with the absence and absent-mindedness that are inherent to the scientifically minded. To our beautiful son Miles, you make the simple act of walking through the door an event. Whatever you grow up to be I hope that you discover some of the joy of finding things out that I have come to know. In the mean time, you can have as many bananas as you want.

Without the support and the values instilled by my family, I would not have even

considered nor been able to begin down this path. My father Stephen and my mother Mari did an exceptional job in teaching me to find something I enjoy and work hard at it. They have always supported me in my education and otherwise, and for that I cannot thank them enough. My brother James has always been a steadfast friend, as comfortable in inane banter after a year away as after an hour away.

It is perhaps a sign of how lucky I am to be surrounded by good people that I find the usual stigma associated with in-laws to be so foreign. While I have been busying myself with research and conferences and thesis writing, they have supplied a steady stream of dinners, barbecues, and child minding. To Dianne and Michael, Frank and Julia, Marina, Todd, and Oli, Bianca and Nathan, Nonna, the wider Barbaro clan, and the Hibberts, thank you for all the help you have provided to Josie, Miles and myself. You may not realize it, but you have been an essential component of this research.

Over the course of the work described in this thesis, it has been my pleasure to work with some exceptional scientists. Damian Murphy of the Australian Antarctic Division has been generous beyond reason with data, which made much of the work in this thesis possible in the first place. David Holdsworth has provided the answers to many of my questions on the obscura of meteor radar, and his work in the field provides a foundation for much of my own.

The Atmospheric Physics Research group at the University of Adelaide also deserves some mention (or perhaps blame?). Like any good graduate student environment, it has been a rotating crew of motley figures, all good company and offering something to learn, a strange blend of calculus, pretty graphs, and beer. Dr. Andrew MacKinnon stands out as perhaps one of the most helpful postdocs in the history of professional science. He has had the answers to so many questions on the minutia of radar design and operation, it has been like having a personal help-line just down the hall. Of course, there are also my co-conspirators in grad school life, Dr. Peter Love, Dr. Bronwyn Dolman, and Ray Oermann, as well as special guest appearances by Octavianus Cakra Satya, Dr. Sujata Kovalam, and Dr. Jens Lautenbach.

A special mention must be made of the legendary Dr. Graham Elford, who has been kind enough to periodically venture out of retirement to assist me with comments and conversation. Few grad students are fortunate enough to be able to talk with someone who has been so integral to their field of research, let alone someone as approachable and helpful as Dr. Elford.

I have been lucky to be just a short drive away from the manufacturer of most of my equipment, ATRAD Pty. Ltd. They have been more than accommodating in my requests for their time and resources, as well as making some fine radars when grad students are not pestering them. Chris Adami showed profound patience as I tried to grasp the functions of basic components and Richard Mayo pretended to not notice when I nearly broke the brand new vectore impedance meter that he drove out to BP for me to fool around with.

This research would not have been possible without significant financial support. The University of Adelaide School of Chemistry and Physics and the Australian Research Council provided a generous scholarship that enabled me to take the time to complete this work. Much of the actual research was made possible by ASAC grant 2529 and ARC grants DP0878144 and DP0558361. I would also like to thank the Australian Institute of Physics for the STSP Student Paper prize and the organizers of the MST 12 conference for the Student Award.

In addition to the people I can mention by name, I would like to thank the anonymous reviewers of my published work. Your unattributed efforts have helped me to grow as a scientist and your comments and suggestions have provided valuable contributions to my research.

A number of my former colleagues from the United States Navy are perhaps unaware of the contribution they made towards the completion of this research. It was the imparted skills of systematic analysis and the exposure to so many different types of sensors that inspired me to study physics in the first place, as well beginning my fascination with radar. The experience of working hard, over long hours in difficult conditions, taught me lessons not available in any educational institution that have been invaluable over the years. I would therefore like to make special mention of my classmates and instructors from Recruit Training Center Great Lakes, Naval Aircrewman Candidate School, Aviation Rescue Swimmer School, AW ‘A’ School, Airborne Acoustic Mission Course, HSL-41, and SERE. It was my pleasure and honor to serve among the talented pilots, aircrewmen, and maintainers of HSL-37, especially Detachment 9 ‘Night Wizards’ and Detachment 7 ‘War Dawgs’, as well as the crews of the USS Lake Erie and USS Fletcher, and the special operators that spent the summer of 1999 in the NAG. I am still, to this day, learning from those five years. IYOYAS.

Finally, I would like to thank Kelley, for what is my favorite piece of academic prose: “The immediate and incredulous conclusion was that the rocket had penetrated a meteor trail, an event so unlikely as to be embarrassing to report.” [Kelley et al., 1998]. Charged dust in the mesosphere is not typically a source of comedy, but I laugh every time I read that passage. Bravo, sir. Bravo.

If anyone has not been mentioned, or not mentioned by name, I apologize. There are so many that deserve my thanks.

Chapter 1

Introduction

This thesis will examine the use of meteor radar to study the atmosphere and meteors themselves. Meteors present the unique opportunity to observe *in-situ* processes in the middle atmosphere using remote sensors. The ablation of meteors makes the atmosphere itself a meteor detector. The trails left behind by ablating meteoroids act as tracers in the atmosphere, drifting with the background wind and diffusing at a rate governed by the local temperature and pressure.

Meteor radar, along with VHF radar and MF radar, fills a void in the capabilities of other sensor systems. The area around the mesopause is too high for balloons to reach; lidars are typically limited to operations at night and only function with clear skies; airglow measurements are similarly limited to clear weather conditions at night; satellites can return a wealth of data, but can only observe individual locations a few times a day if at all; rockets provide the opportunity to directly measure the atmosphere, but cost and logistics make them impractical for routine surveillance.

Meteor radars operate day and night in all weather conditions. All that is required for observations is the presence of ionized meteor trails, which are more than plentiful. Thus, meteor radars sit quietly detecting a constant precipitation of celestial debris, regardless of the presence of daylight or weather. The following work describes recent advances concerning the theoretical background and interpretation of the results of meteor radar.

1.1 Meteors

Consider a small object in orbit around the Sun. It is most likely composed of stone, but could also be metal, ice, or a combination of materials. As the body moves under the influence of the Sun's gravity, Earth moves in an independent orbit that happens to intercept that of the small body.

Approaching the surface of Earth at a relative speed of tens of kilometers per second, the body begins to collide with atmospheric molecules. In each collision, a portion of kinetic energy is converted to heat. Deeper into the atmosphere, the density of atmospheric molecules increases, accelerating the rate at which the body is heated.

Eventually, the small body is heated at a rate that exceeds the loss of thermal energy due to radiation. Material then evaporates from the surface of the body, leaving behind a trail of vapor that is ionized by subsequent collisions with atmospheric molecules.

The preceding narrative is a simple description of the process by which meteors are formed. The word "meteor" itself comes from ancient Greek, meaning "raised beyond". A body that enters the atmosphere from space is a meteoroid. The term meteor is generally reserved for the trail of material left in the wake of an evaporating meteoroid. Sometimes this material is dense and energetic enough to be visible as a glowing trail. If a meteoroid survives the rigors of atmospheric entry long enough to impact the ground, it is known as a meteorite (see, e.g., McKinley [1961]).

Meteoroids have their origins in a number of sources. They can be castoff material from comets or asteroids, the remnants of a disintegrated parent body, or small particles left over from the planetary nebula that formed the solar system. Large meteoroids may actually be comets or asteroids themselves, as there is no upper size limit in the definition (see, e.g., Ceplecha et al. [1998]).

Small bodies do not orbit the Sun indefinitely. Solar radiation is absorbed by a small body and re-emitted uniformly in the frame of reference of that body. Taken in the frame of reference of the Sun, however, the relativistic radiation pattern is biased towards the direction of motion of the body. The Poynting-Robertson effect, as this is called, decelerates small bodies in the frame of reference of the Sun. Over time, this results in a reduction in the semi-major axis and eccentricity of the orbit of objects orbiting the Sun. The Poynting-Robertson effect is more pronounced for smaller bodies, given their smaller mass to surface area ratio. Eventually, the orbit of small particles will decay to the point at which they are consumed by the Sun [Wyatt and Whipple, 1950].

Meteors may be classed broadly according to their originating orbits as either shower meteors or sporadic meteors. Shower meteors are the result of narrow filaments, called streams, of debris that follow an orbit that intersects the orbit of Earth. This results in an enhancement in the number of meteors originating from a particular direction when Earth passes through the debris stream.

Sporadic meteors comprise the overwhelming majority of the meteors observed in the atmosphere. There are six major sources of sporadic meteors, as mapped in relation to the direction of the orbital motion of Earth and the direction to the Sun from Earth. The helion and antihelion sources lie in and away from the direction of the Sun from Earth, respectively. The north and south apex sources lie about 15° above and below the direction of orbital motion of Earth. Finally, the north and south toroidal sources are located at about 60° above and below the direction of the orbital motion of Earth. Each of these sources is a diffuse concentration about 15-20° wide [Jones and Brown, 1994].

Each sporadic source is fixed in relation to the orbital geometry of Earth. Changes in the angle between the axis of rotation and direction of travel of Earth through the year cause seasonal variations in the relative strength of different sporadic sources at different locations on the surface of Earth. This effect also produces an annual variation in the detection rate of sporadic meteors at fixed observing locations.

1.2 The Atmosphere

Earth is surrounded by a thin envelope of gases that decreases in density approximately exponentially with height, due to hydrostatic forces. The atmosphere is a dynamic structure driven by the balance of incoming solar radiation and outgoing terrestrial radiation, the rotation of the planet, interactions with terrain features, the hydrological cycle, chemical reactions, and tidal forces.

The atmosphere can be broadly separated into layers by the different temperature gradients present, as illustrated in figure 1.1. At the bottom lies the troposphere with decreasing temperature with respect to height, where most weather occurs. At the tropopause, about 10 km above the surface, the temperature begins to increase with height. This marks the start of the stratosphere, which is characterized by convective stability. The next point of inflection at around 50-60 km marks the lower boundary of the mesosphere which extends to about 80-90 km. The mesosphere has the distinction of hosting the coldest temperatures in the terrestrial environment, as low as 130 K in polar summer conditions . Most meteors occur near the mesopause. Above the mesosphere lies the thermosphere, the outermost layer of the atmosphere. Temperatures in this region can be in excess of 2,000 K [Houghton, 1977].

1.3 Meteor Observations

Larger meteoroids produce luminous trails that can be observed with the naked eye. Records of intense meteor showers and spectacular individual fireballs are present in literature from ancient civilizations across the globe.

The modern study of meteors can be traced to the suggestion by Chladni that meteors are the result of frictional heating of celestial particles in the atmosphere. In 1798, Brandes and Benzenberg used triangulation of visual observations to estimate the height and speed of meteors. The 19th century witnessed a number of intense shower events that were widely observed by the general public, leading to further

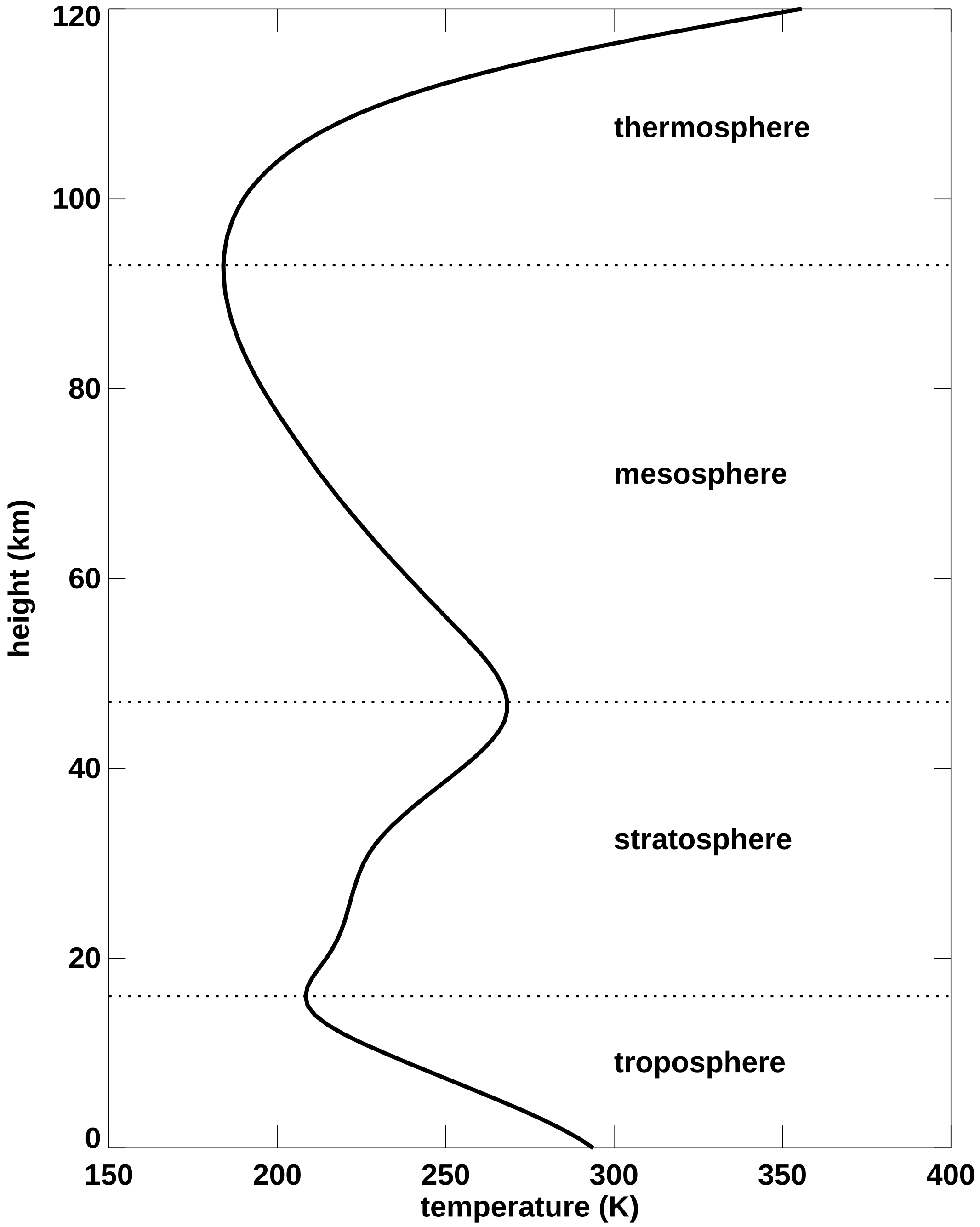

Figure 1.1: Atmospheric temperature profile taken from the NRLMSISE-00 model for 35 S during the vernal equinox.

interest in the burgeoning field of meteor science. In particular, the remarkably intense 1833 appearance of the Leonid shower was viewed with great interest by both academia and lay observers across North America. Drawing on observations of a similar outburst in 1799, a number of astronomers, including Schiaparelli in his landmark work *Sternschnuppen* ("snuffed stars"), accurately predicted a repeat performance in 1866. Through the latter half of the 19th century, astronomers also began to note the similarity between the orbits of certain meteor showers and known comets.

Beyond the simple mapping of visually observed meteor paths on a map of the sky, photographic means provided a significant advance in the early 20th century. Early campaigns relied on crude cameras pointing skyward, which eventually evolved to specialized devices such as the Super-Schmidt camera developed by Baker at Harvard. As early as 1896, attempts were made to determine the the composition of meteoroids from the spectra of meteor trails (see e.g., McKinley [1961]).

1.4 Early History of Meteor Radar

The use of radio methods for the detection of meteors represented a fundamental leap in the ability to detect, understand, and exploit meteor phenomena. At the most basic level, radio meteor detection is accomplished by transmitting radio waves and observing the scatter from meteor trails. This can be done with the transmitter at or near the receiving antenna, as in the case of a traditional radar (from the contraction: RAdio Detection and Ranging). Alternatively, forward scatter systems detect the scatter of a meteor located between the receiver and a distant transmitter. McKinley [1961] and Baggaley [2009] present detailed descriptions of the development of meteor radar, a summary of which is provided below.

In the late 1920s, researchers studying the ionosphere with 1-4 MHz systems observed so-called sporadic E-layer activity, wherein short duration increases in ionization are detected. Of particular interest were detections of increased ionization at night, when the normal mechanism for atmospheric ionization, the Sun, was absent

[Appleton, 1930].

As early as 1929, Nagaoka [1929] theorized that meteors could be detected using radio methods. However, he erroneously postulated that detection would be possible because the passage of a meteor would deplete the background ionization to produce a detectable gradient in the refractive index of the atmosphere.

A number of studies throughout the 1930s including those by Skellet [1935b] and Eckersley [1937] increasingly made the connection between sporadic-E activity and meteors. Skellet [1935a] made an early attempt to estimate the ionization produced by the ablation of a meteoroid in the atmosphere. Pierce [1938] went further, positing that a meteor produces a cylindrical column of ionized material that expands over time, leading to a reduction in observed scatter intensity. Watt et al. [1937] obtained the first recording of a meteor radar echo using a 6 MHz vertical sounder.

The current theory of meteor radio scatter is attributed to Blackett and Lovell [1941]. They theorized that cosmic rays would produce trails of ionization that could be detected by radio scatter. The intensity of the scattered radio waves could be described by a Fresnel diffraction pattern. While this proved not to be the case for cosmic rays, the Fresnel description of the observed diffraction pattern proved applicable to meteor trails.

The development of radars for defense purposes during the Second World War provided a boon for radio studies of meteors. During the war, radar operators routinely detected meteors with aircraft direction and gun leveling radars, although these detections constituted interference.

Following the war, the large number of available radars and personnel familiar with radar translated into a number of vigorous research efforts, most notably from 1945 at Jodrell Bank in the United Kingdom. Lovell and Clegg [1948] presented a summary of the advances made in the theoretical understanding of meteor scatter over the preceding decade, including a detailed description of the meteor trail reflection coefficient. The initial work at Jodrell Bank was followed by significant activities by the National Research Council, Ottawa, Canada, the University of Adelaide, Australia, and Canterbury University College, New Zealand.

Meteor radar work has since expanded to institutions around the world. It now encompasses the study of winds and diffusion in the mesosphere, meteor ablation, and meteor astronomy to name but a few topics.

1.5 Thesis Structure

This thesis examines the use of interferometric VHF meteor radar for atmospheric and astronomical research. Each chapter provides an overview of a particular sub-topic and discusses new progress made in the course of this research. Chapters are ordered so as to step through the logical progression of radar function, meteor trail formation, meteor trail detection, characteristics of the meteor echo, and deviations from the case of an ideal echo. Additionally, the use of meteor radar for meteor astronomy is discussed.

Chapter 2 describes the design and operation of an all-sky VHF meteor radar with an interferometric receiving antenna array, including the estimation of backscatter angle-of-arrival via the comparison of antenna pair phase differences. The meteor response function is reviewed in order to assess the impact of different radar and meteor parameters on the detectability of different meteors. Mutual coupling between antennas is assessed for the impact on angle-of-arrival estimates, including measurements of coupling taken from a working radar. A new method of calibration is presented, whereby diffusion coefficient estimates from meteor detections are used in a post-statistical steering scheme. It is shown that this method produces equivalent results to echo phase based methods, allowing for the calibration of meteor detection data without the original phase data.

Chapter 3 discusses the physical processes responsible for the formation of trails of ionized meteoric material, including heating by collision with atmospheric molecules, radiation, evaporation, and sputtering. The results of numerical simulations of meteoroid ablation are used to explain a number of different phenomena including the ionization profile of different meteor types, the initial size distribution of detected meteors, the deceleration of meteoroids, and the significance of sputtering in trail formation.

Chapter 4 combines the meteor response function presented in Chapter 2 with the ablation physics covered in Chapter 3 to provide a description of the mechanics determining the height distribution of detected meteors. The range of heights over which meteors are detected is shown to be a nearly linear function of the density scale height of the atmosphere. A correlation between the height of constant density contours and the peak height of meteor detection will also be demonstrated.

The evolution over time of individual meteor echoes is described in Chapter 5. Starting with the Fresnel diffraction pattern, modifications to echo intensity are introduced in the form of the initial radius of the trail and diffusion of ionized material away from the meteor trail axis. Deviations from the ideal meteor trail are examined, including non-Gaussian trail cross-sections, non-constant electron density along the trail axis, and fragmentation. Methods for estimating meteor velocity from the meteor echo are reviewed.

Chapter 6 examines the impact of anomalous diffusion phenomena on the decay times of meteor echoes. The effect of multiple ionic species is demonstrated through numerical simulations of differential diffusion, including cases where each ionic species has a unique initial distribution radius. Modification to echo decay times due to aerosol absorption of electrons are examined using numerical simulations for a range of VHF meteor radar wavelengths. Data from co-located radars with different operating frequencies are compared with the predictions of simulations to illustrate consistency of observations with the presence of absorbing aerosols.

Chapter 7 deviates from the previous chapters by discussing meteor radar astronomy. The limitations of single station meteor radars for the determination of meteor trajectories are discussed, along with statistical methods for the detection of meteor showers. The results of a two-year survey of meteor showers conducted using radars at different locations are presented, including the discovery of a number of previously unreported showers. Data for each meteor shower system are used to calculate the orbital parameters for the parent stream of debris.

A closing chapter provides a summary of the advances presented in each of the preceding chapters. The thesis closes by outlining opportunities for further research.

1.6 Summary of Original Research

The original research presented in the following chapters answers the following questions:

Chapter 2: What is the effect of mutual coupling of antennas on angle-of-arrival estimates of meteor radar echoes?

How can meteor echo decay times be used to infer phase measurement biases in a meteor radar receiver?

Chapter 3: What is the distribution of initial meteoroid sizes that produce detected meteors?

What is the magnitude of deceleration during the detection phase of meteors?

What role does sputtering play on the formation of meteoric ionization?

Chapter 4: How does the density scale height affect the height distribution of detected meteors?

How is the peak meteor detection height affected by changes in the height of constant density levels?

Chapter 5: What is the effect of non-constant meteor trail electron line density on the decay time of a meteor radar echo?

How is the meteor echo decay time affected if the diffusion coefficient varies along the length of a meteor trail?

What effect does fragmentation have on the decay time and diffraction pattern properties of a meteor echo?

Chapter 6: What is the decay time of an echo from a meteor trail composed of multiple ionic species?

How are meteor echo decay times affected if each ionic species has a unique initial distribution?

What is the wavelength-specific effect of aerosol absorption on the decay time of meteor echoes?

How do numerical predictions of aerosol absorption compare with the observations of co-located radars with different wavelengths?

Chapter 7: What meteor showers can be detected using single station meteor radar observations in the southern hemisphere?

How can shower meteors be used to estimate the precision of the Fresnel transform velocity estimation technique?

What are the orbital characteristics of debris streams responsible for meteor showers?

These questions represent new lines of inquiry, as well as long-standing issues with the use of meteor radar. The answers obtained by the original research described in this thesis provide mitigation strategies for dealing with systematic errors, a detailed examination of the different factors affecting meteor radar observations, new metrics for atmospheric characterization, explanations for anomalous meteor radar echo phenomena, and new results from established methods. The closing chapter of this thesis provides a synopsis of the answers found for each question.

Chapter 2

Interferometric Meteor Radar

The detection of meteors using radar can be accomplished with a variety of hardware configurations. The radars considered in this study are all comprised of a single, all-sky-illuminating transmit antenna and multiple pairs of receive antennas that are used to deduce the angle to received echoes by means of interferometry.

The design and operation of these radars are considered with an emphasis on the limitations of the positional accuracy of meteor detections. Whether used for meteor astronomy or atmospheric observations, it is critical to understand the precision to which the position of particular detections are known. Atmospheric observations in particular require that attention is paid to the precision of height estimates.

Once the sources of uncertainty and possible biases are known, data sets can be refined based on the reliability of individual detections. Knowledge of the mechanisms responsible for introducing biases into measurements allows calibration techniques to be developed.

2.1 Hardware Configuration

2.1.1 Antenna Array

Jones et al. [1998] describe what has become the standard configuration for interferometric meteor radars. Two baselines, each consisting of three antennas are laid out

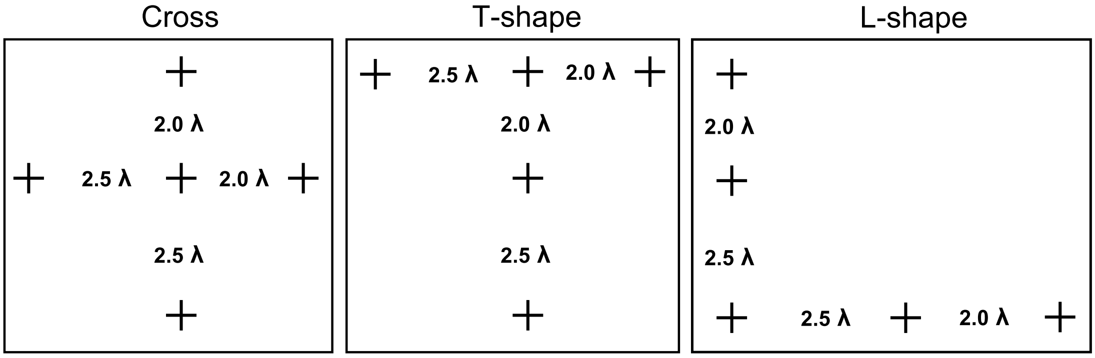

Figure 2.1: Possible interferometer configurations.

perpendicular to each other, sharing a common antenna. A cross pattern is usual, but L and T-shaped arrangements are also possible, as shown in figure 2.1. It is also possible to construct two separate baselines containing three antennas each, without the shared common antenna of the other configurations. In all cases, the target meteoroids are illuminated by an all-sky transmit antenna located near the receiving array. A typical site layout is illustrated in figure 2.2.

2.1.2 ATRAD Meteor Radar General Configuration

All observations detailed in this study were conducted using interferometric meteor radars produced by ATRAD Pty. Ltd. While there are some differences between individual systems, such as the addition of switching to operate an additional ST (Stratospheric-Tropospheric wind profiler) array from the same transmit/receive unit or the use of vacuum tube versus solid-state amplifiers, all systems conform to the same general design in terms of transmission and reception for meteor detection purposes. The specifications of the radars are summarized in table 2.1.

The internal componentry of the radar can be broadly divided into a control and analysis component and an RF component. Control and analysis duties are performed by an acquisition PC running Microsoft Windows 2000. The RF component is comprised of a transmit/receive unit called an STX if solid state amplifiers are used or a VTX for the case of vacuum tube amplifiers.

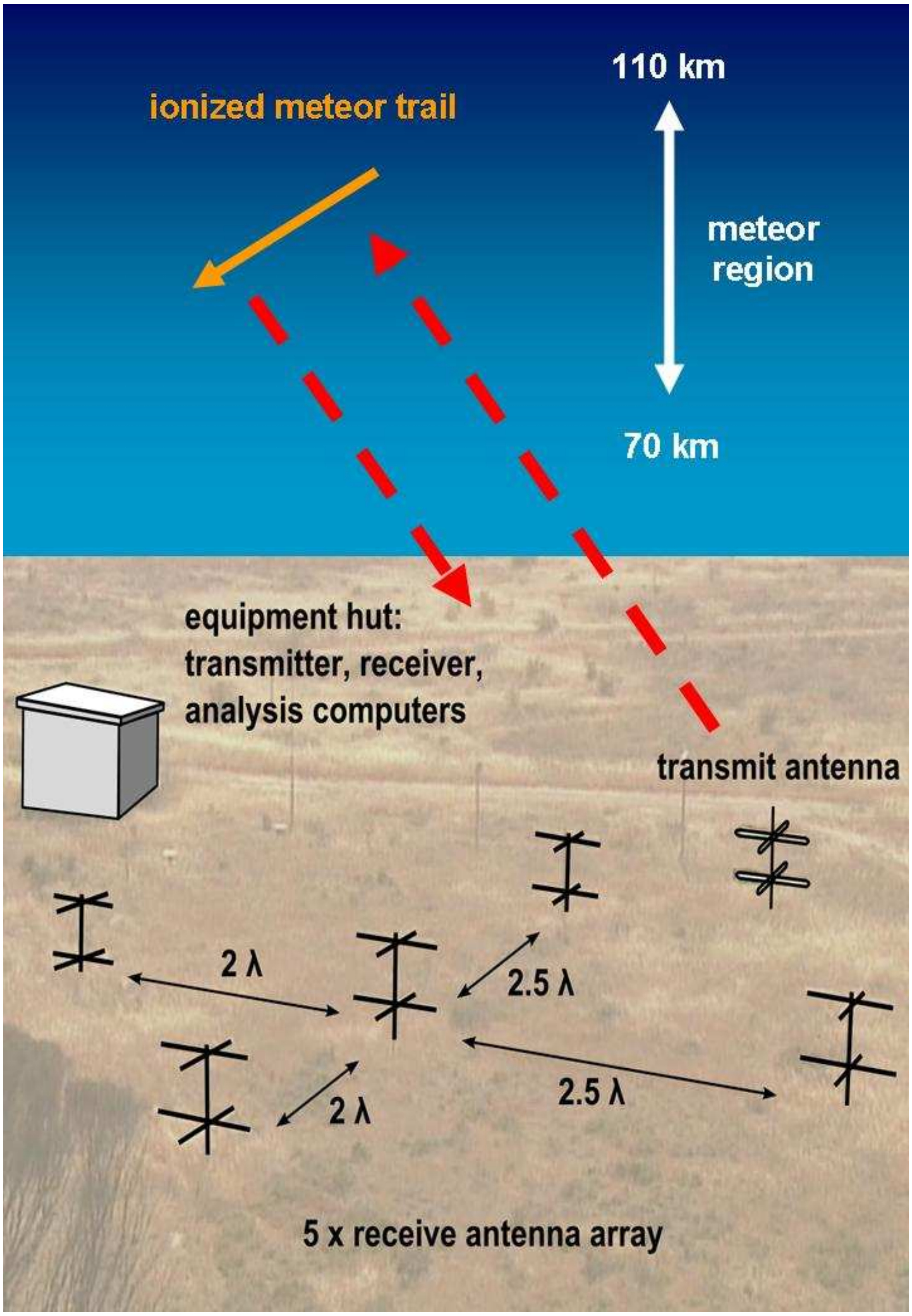

Figure 2.2: Site layout of the Buckland Park, Australia meteor radar.

peak power	7.5-40 kW
maximum duty cycle, uncoded pulse	5%
maximum duty cycle, coded pulse	8.3%
operating frequency	30-60 MHz
typical PRF	430 Hz
maximum PRF	20,000 Hz
typical HPFW pulse length	3.6 or 7.2 km
HPFW pulse length	0.1-9 km
HPFW receiver filter width	18-404 kHz

Table 2.1: Summary of ATRAD meteor radar specifications (adapted from Holdsworth et al. [2004a]).

Four radars were used in this study, shown in figure 2.3: A 33 MHz radar is located at Darwin, Australia using a 7.5 kW STX. Buckland Park, Australia has a 55 MHz, 40 kW STX II, upgraded through a 20 kW STX from a 7.5 kW VTX. Both of these radars are operated by The University of Adelaide. Davis Station, Antarctica, hosts a 7.5 kW STX 33 MHz system operated by the Australian Antarctic Division and a 14 kW STX 55 MHz system operated jointly by the Australian Antarctic Division and The University of Adelaide. Both the Buckland Park radar and the 55 MHz radar at Davis Station are hybrid systems that share a single transmit/receive unit between a meteor array and an ST wind profiling array. Due to time sharing between the two arrays, detection rates are lower for these systems than for a dedicated meteor radar.

The acquisition PC performs overall command and control functions for the radar, including triggering, initiation of the RF drive, and recording of time series information from the receiver paths. The transmit/receive unit handles the generation of transmitted signals and the reception of received signals. In this component, outgoing pulses are generated, modulated, and amplified. Received signals are amplified and phase determination is performed by quadrature analysis.

Typical meteor detection modes transmit with a 430 Hz pulse repetition frequency, but the radars have the ability to transmit with a PRF of up to about 20 kHz, as limited

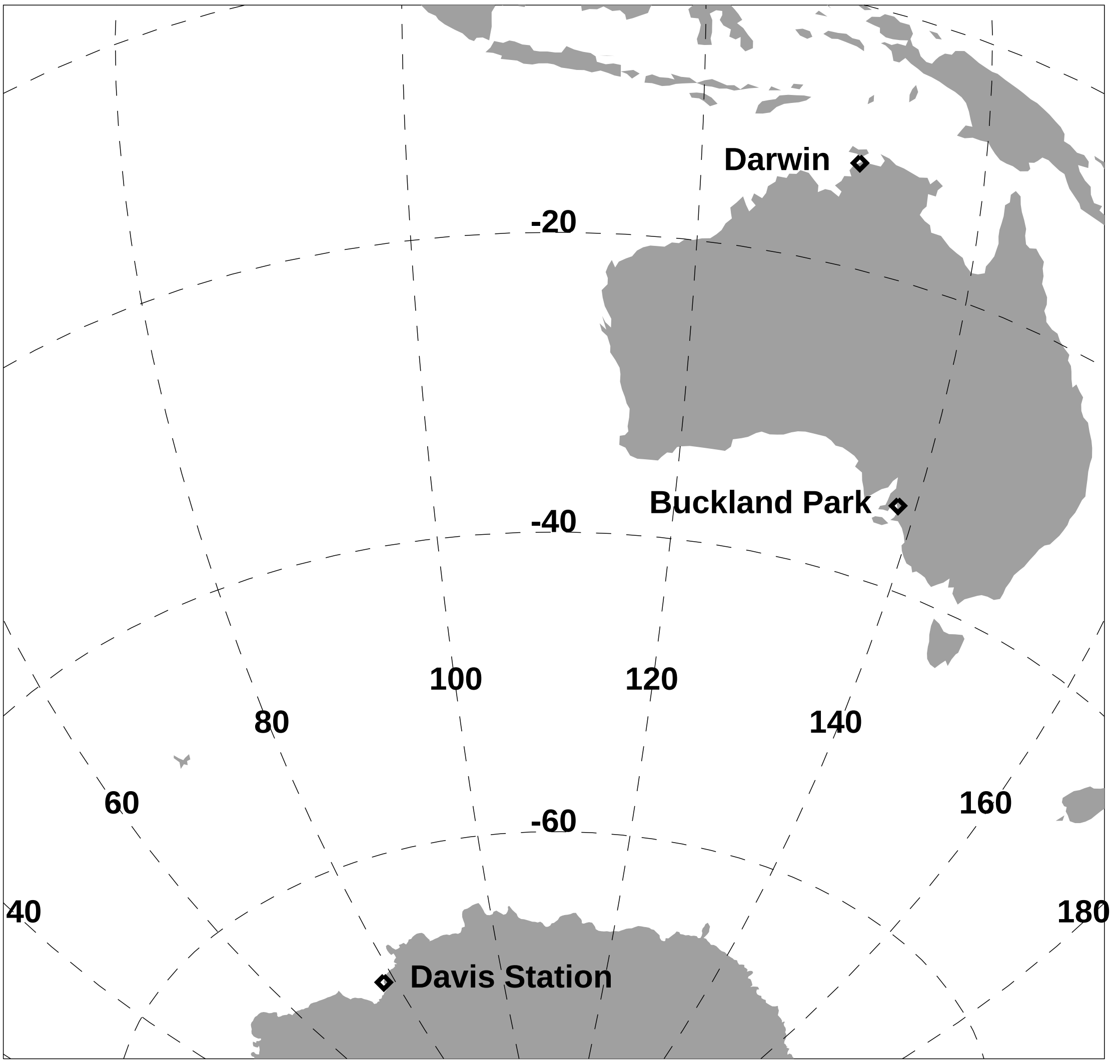

Figure 2.3: Locations of meteor radars used in this study: Darwin, Australia (12.46 S, 130.93 E), Buckland Park, Australia (34.62 S, 138.47 E), and Davis Station, Antarctica (68.57 S, 77.97 E).

by the duty cycle capabilities of the individual radars. Due to the return trip time-of-flight of pulses to and from meteors, higher PRFs can result in range aliasing, whereby an echo from a previous pulse is received during the listen period of a subsequent pulse. This can be mitigated by further analysis of the pulse, such as determining if the height of candidate returns occur in a realistic meteor ablation zone.

Pulses are Gaussian shaped with a usual full-width-at-half-maximum (FWHM) of 3.6 km, with the option of a 7.2 km long pulse. Upon reception, pulses are subject to four pulse coherent integration to improve the signal-to-noise ratio [Holdsworth et al., 2004a].

2.1.3 Transmission Signal Flow

The acquisition PC controls the overall function of the transmission path. Commands sent from the acquisition PC to the STX are handled by the Power Amplifier (PA) subsystem of the transmit/receive unit. The PA controller also performs system monitoring and fault protection, shutting down the system in the event of overheating or mismatch outside of tolerances.

Generation of the initial RF carrier is initiated by commands from the COM2 port of the acquisition PC to a synthesizer in the transmit/receive unit, which produces a ± 3 V continuous wave RF drive signal at the operating frequency of the radar. Trigger pulses sent by the acquisition PC to a microcontroller in the PA controller subsystem of the STX generate the specified pulse envelope, which is passed through a digital to analogue converter before being applied to the carrier frequency, which is also amplified to $\pm$ 6 V. By varying the height of the pulse envelope, the power of the outgoing pulse can be controlled, allowing for control of the final transmitted power.

For the example of a 20 kW STX system, the modulated pulse is then sent to the driver module, which splits the signal into 6 lines, each of which is sent through a 4 kW amplifier. This nominally produces 24 kW of output power. Accounting for losses within the entire system, this produces approximately 20 kW of actual output power. These numbers are taken from the documentation for a 20 kW system, but the specifications of radars with different transmitted powers are simply a matter of scale. The six amplified signals are then combined into a single feed before being split into two separate transmission lines to the transmit antenna, one of which incorporates a 90° delay line.

At the transmit antenna, each transmission line is connected to one arm of a folded cross dipole antenna. The addition of a 90° delay on one of the arms produces circular polarization. The transmit antenna itself is a crossed folded dipole constructed from stainless steel tubing. A balun is used to reduce the antenna's 200 Ω impedance to the 50 Ω impedance of the transmission line.

2.1.4 Reception Signal Flow

The receive antennas are crossed dipoles constructed from aluminium tubing connected to the transmission lines by means of a gamma match that adjusts the antennas to 50 Ω impedance and zero reactance. The received signals are first sent through low noise amplifiers, supplied by a 15 V source, which add approximately 20 dB to the signals.

Inside the transceiver, each channel passes through a receiver module with variable gain controlled by the acquisition PC. Here, the signals are converted to an intermediate working frequency of 80 MHz. Each channel is then passed to a detector module, including a programmable receiver filter with an adjustable bandwidth from 18.1 to 404.0 kHz. The effective bandwidth is adjusted to suit the pulse length used in order to optimize the signal-to-noise ratio. Each channel is then split into in-phase and quadrature components for phase measurement.

Background noise levels are determined by dividing the combined receiver time series into 4 s blocks and the noise is defined as the mean amplitude in each block. The bin size is well in excess of the typical underdense meteor decay time, eliminating any substantial effect of meteor echoes occurring within the bin.

Meteors are detected from the recorded time series using a noncoherent or coherent detection method. Nocoherent detection is performed by combining the receiver time series within each range gate and searching for candidates that exceed a preset multiple of the background noise for two successive samples. Three point smoothing is performed and the echo candidate is then characterized by the time of the first sample above the noise threshold, time of peak amplitude, and time of the last sample above the noise threshold.

For coherent detection, complex time series is divided into 1 s blocks and the cross-correlation functions for different receiver pairs are calculated. If the RMS phase difference between the cross-correlation functions and the linear least squares fit of the cross-correlation functions is less than 25°, then the complex time series are combined coherently. The detection process then follows as for the noncoherent case [Holdsworth et al., 2004a].

2.1.5 Phase Determination

A local oscillator in the detection module produces a continuous wave 80 MHz signal that is split into two portions, the in-phase component, which is left intact, and the quadrature component which is delayed by 90°. Both in-phase and quadrature components are normalized to the input channel strength and mixed with the signal. The output are then sent to the acquisition PC for recording by a data acquisition card. The separation of each channel into in-phase and quadrature components allows the phase of the signal relative to a reference oscillator to be inferred from a comparison of the amplitudes of the in-phase and quadrature components.

2.2 Angle-of-Arrival Estimation

An interferometer baseline is constructed by placing two antennas at a separation d and observing the difference in phase of an incident wave as measured at the two antennas. For an antenna baseline formed by two antennas and a series of wavefronts with wavelength λ approaching from angle-of-arrival ψ as shown in Figure 2.4, the

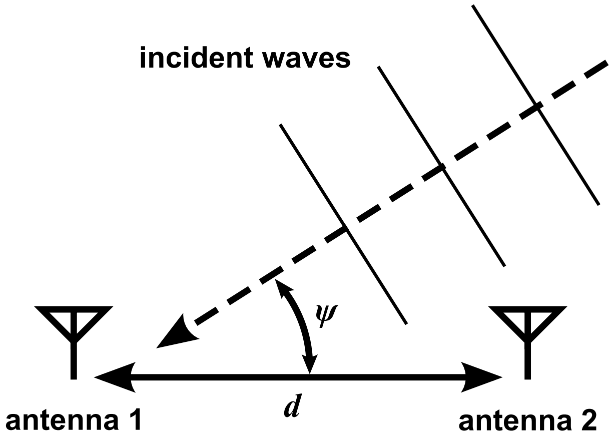

Figure 2.4: Basic interferometer geometry.

phase difference between the two antennas is given by

$$\chi = 2\pi \frac{d}{\lambda} \sin\psi. \tag{2.1}$$

Upon measurement of χ, this relationship can be inverted to obtain the angle-of-arrival of the incident waves. This inversion, however, only yields a unique value for ψ when $d \leq 0.5\lambda$.

Unfortunately, the placement of antennas in such close proximity can introduce significant errors into phase difference estimates due to mutual coupling between antennas. This effect can be overcome by increasing d, but this in turn produces an ambiguous set of candidate values for ψ. This ambiguity can be removed while maintaining increased antenna spacing by placing three antennas along the same baseline with inter-antenna separations of d_1 and d_2, such that $|d_1 - d_2| \leq 0.5\lambda$.

2.2.1 0.5/2.0/4.5 method

The use of increased spacing has the additional benefit of increased accuracy when comparing the phase differences of antennas spaced at greater values of d. The current implementation uses a progressive approach to the estimation of the angle-of-arrival, comparing successively larger values of d to obtain more accurate estimates of ψ, while maintaining unambiguous selection criteria. Along each baseline, the three antennas

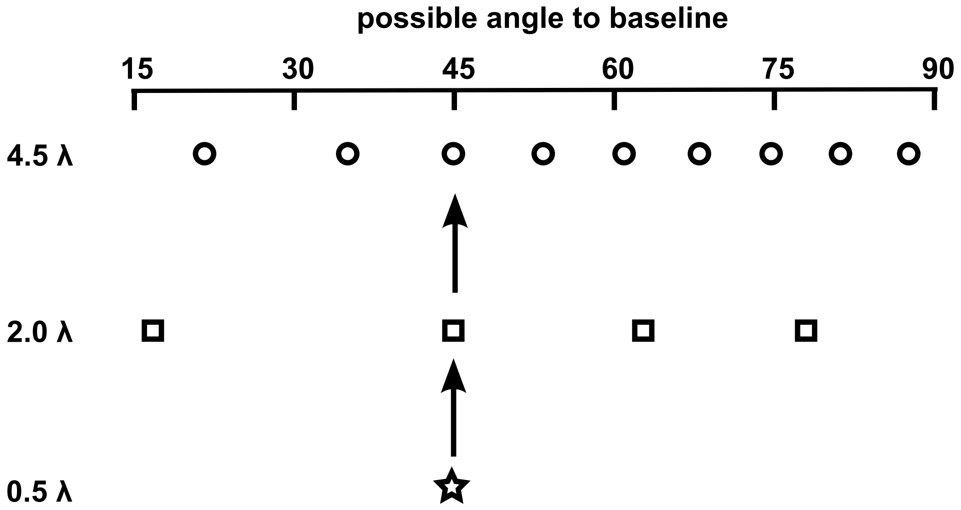

Figure 2.5: 45° example of the process for selecting the correct angle-of-arrival from candidates generated by 2.0λ and 4.5λ phase differences.

are spaced so that one pair is 2.0 λ apart and the adjacent pair is 2.5 λ apart. This creates a combined spacing of 4.5λ, as well as a virtual 0.5λ spacing.

By combining the phases of each antenna on a baseline, combined phase differences can be constructed as $\chi_{4.5\lambda} = \chi_{2.5\lambda} - \chi_{2.0\lambda}$ and $\chi_{0.5\lambda} = \chi_{2.5\lambda} + \chi_{2.0\lambda}$. In this way, unambiguous estimates of the angle-of-arrival can be made using antennas at spacings greater than 0.5λ. Furthermore, $\chi_{4.5\lambda}$ provides a more accurate estimate of the angle-of-arrival than the individual pair spacings, once ambiguity in the estimate has been removed by comparison with $\chi_{0.5\lambda}$.

An initial estimate of the angle between the direction of propagation of the incident wavefronts and the antenna baseline is made using the 0.5λ phase difference. This is then used to select the closest ambiguous candidate angle-of-arrival from the set produced by the next antenna spacing to be considered.

Due to the possibility of large errors in the 0.5λ phase pair, the angle-of-arrival may be erroneously assigned to the wrong 4.5λ candidate. This can be overcome by a more gradual progression, including an intermediate comparison with the 2.0λ phase difference. Thus, the correct angle-of-arrival is determined by using the 0.5λ phase difference to obtain an initial estimate of the angle-of-arrival. This is then used to select the appropriate value from the possible angles of arrival generated from the 2.0λ phase difference by selecting the candidate that produces the smallest value of $|\psi_{0.5\lambda} - \psi_{2.0\lambda}|$. $\psi_{2.0\lambda}$ is then used to select the appropriate value of $\psi_{4.5\lambda}$ for the more accurate 4.5λ phase pair.

Holdsworth [2005] improves upon this process, noting that the phase differences are linear in the cosine of the angle-of-arrival. Therefore, the more appropriate quantity to minimize when selecting a candidate angle-of-arrival is $|\cos\psi_{0.5\lambda} - \cos\psi_{2.0\lambda}|$, and similarly for $\psi_{4.5\lambda}$. This method provides a small increase in the accuracy of angle-of-arrival estimation, especially for large zenith angles. This is the method applied in the simulations and observations used in this study.

2.2.2 Conversion to azimuth, zenith, and height

Once the angle-of-arrival to each baseline is obtained, the two angles are used in concert with the range of the detection to determine the position of the meteor in the sky relative to the receiving station. The zenith angle θ is obtained from the direction cosine relation

$$\cos^2\theta = 1 - \cos^2\psi_1 - \cos^2\psi_2. \tag{2.2}$$

The azimuth from a particular baseline is then calculated using

$$\phi = \cos^{-1}\left(\frac{\cos / \sin\psi}{\sin\theta}\right), \tag{2.3}$$

where the sine or cosine is used depending on which baseline is being used. If azimuth is measured relative to the baseline supplying a value of ψ to equation 2.3, then the $\cos\psi$ is used.

When determining the height of a meteor using the zenith angle and slant range, it is necessary to account for the curvature of the Earth to obtain the true local height of the meteor above the ground. For a meteor at range R, as depicted in Figure 2.6, the height above the surface of the Earth is given by

$$h = \sqrt{R_e^2 + R^2 + 2RR_e\cos\theta} - R_e, \tag{2.4}$$

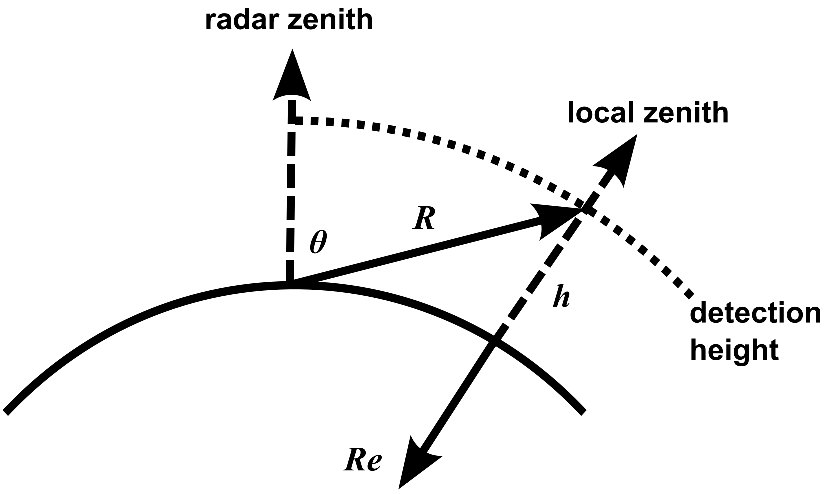

Figure 2.6: Geometry used to determine the height of an off-zenith meteor detection.

where R_e is the radius of Earth.

2.3 Performance

The ability of a radar to detect a meteor trail depends on the sensitivity and operating parameters of the radar, atmospheric conditions, the velocity of the meteor, and the electron density of the trail. The free electron content of a trail is usually described by the electron line density, q, which is the total number of electrons per unit length of the trail.

2.3.1 Underdense meteor function

The power scattered from an underdense meteor that is received by a radar is given by

$$P_R = 2.5 \times 10^{-32} q^2 \left(\frac{\lambda}{R}\right)^3 P_T G_T(\theta,\phi)\, G_R(\theta,\phi)\, (\alpha_r \alpha_v \alpha_d)^2 , \tag{2.5}$$

where λ is the wavelength of the radar, P_T is the transmitted power, G_T is the gain of the transmitting antenna, and G_R is the gain of the receiving antennas (see, e.g., Ceplecha et al. [1998]). Augmenting the equipment parameters are three attenuation factors, α_r, α_v, and α_d, relating to the properties of the meteor trail (A derivation of this relation is provided in chapter 5.). The role of each attenuation term in modifying the detectability of a meteor trail is now explained.

Following the passage of a meteor across the field of view of a radar, the ionization is not concentrated entirely on the trail axis, but rather is distributed around it. This leads to destructive interference from scattering in the off-axis regions, reducing the overall strength of the observed echo. Assuming the ionization has a Gaussian radial profile, then

$$\alpha_r = \exp\left(-\frac{4\pi^2 r_0^2}{\lambda^2}\right), \tag{2.6}$$

where r_0 is the initial radius of the trail (see, e.g., McKinley [1961]). The initial radius of the trail is dependent on the properties of the atmosphere in which the ionized material is deposited and is described in more detail in section 5.2.1.

Once the meteor trail is formed, scattering electrons in the trail begin to diffuse immediately. For a meteor with finite velocity, the regions of the trail further back from the meteoroid will have diffused more than the recently formed parts of the trail near the meteoroid [Peregudov, 1958, Baggaley and Webb, 1980]. The result is that, compared to an instantaneously formed trail, a fully formed underdense echo from a meteor with finite velocity has its observed scatter reduced by a factor of

$$\alpha_v = \frac{1 - e^{-\Delta}}{\Delta}, \tag{2.7}$$

where, for local ambipolar diffusion coefficient D (see section 5.2.2),

$$\Delta = \frac{16\pi^2 D}{v}\left(\frac{R}{2\lambda^3}\right)^{1/2}. \tag{2.8}$$

For pulsed radars, the sampling of the echo at discrete, separated points in time results in a bias against short duration echoes. A meteor trail may have sufficient electron line density to be detectable, but the echo maximum may rise and decay between pulses, leading to the meteor trail not being detected. The factor α_d accounts for this bias, which is given by

$$\alpha_d = \frac{\tau}{t_I}\left(1 - e^{-t_I/\tau}\right), \tag{2.9}$$

where t_I is the pulse repetition interval of the radar and τ is the time constant of the exponential decay of an underdense meteor echo (see, e.g., Ceplecha et al. [1998]). In the event that the radar has a criterion of n pulses above the detection threshold to register a detection, then equation 2.9 becomes

$$\alpha_d = \frac{\tau\left(1 - e^{-t_I/\tau}\right)}{t_I e^{(n-1)t_I/\tau}}. \tag{2.10}$$

2.3.2 Overdense cutoff

For a system detecting underdense meteors, the maximum detectable line density is that which crosses through the transitional region to become overdense. From McKinley [1961] the overdense condition can be derived as follows. When a meteor trail has sufficient electron volume density N that the dielectric constant κ is less than or equal to zero, a radio wave can no longer penetrate the volume. The dielectric constant is given by

$$\kappa = 1 - \frac{N\lambda^2}{\pi} r_e, \tag{2.11}$$

where λ is the radar wavelength and r_e is the classical electron radius. The critical density above which radio waves can no longer penetrate the volume can be found by solving for the electron density when $\kappa = 0$. Assuming that the distribution of ionization in a meteor trail is Gaussian with respect to the distance from the trail axis, the line density associated with the critical density N_c achieved at a distance r_c from the center of the trail can be obtained from:

$$N_c = \frac{\pi}{\lambda^2 r_e} = \frac{q_c}{\pi\left(4Dt + r_0^2\right)} \exp\left(-\frac{r_c}{4Dt + r_0^2}\right), \tag{2.12}$$

where D is the ambipolar diffusion coefficient, t is the time since formation of the trail, and r_0 is the initial radius of the trail. Solving Equation 2.12 for q_c, the critical line density at which a meteor trail becomes overdense is given by $q_c = \mathrm{e}/4r_e = 2.4 \times 10^{14}$ electrons m^{-1}, where e is the charge of an electron.

At or above this line density, incident radio waves are likely to scatter from multiple points in the trail before returning to the receiver, eliminating the coherence of the observed backscatter and producing reflective behavior akin to that of a conducting cylinder. Thus, q_c serves as a maximum line density for underdense meteor echoes.

2.3.3 Minimum detectable electron line density

Rearranging Equation 2.5, the minimum detectable line density is given by

$$q_{min} = 6.3 \times 10^{15} \left(\frac{R}{\lambda}\right)^{3/2} \left(\frac{P_{Rmin}}{P_T G_T(\theta, \phi)\, G_R(\theta, \phi)}\right)^{1/2} \left(\alpha_r \alpha_v \alpha_d\right)^{-1}, \tag{2.13}$$

where P_{Rmin} is the minimum power to exceed the signal-to-noise threshold of the receiving system. This provides the minimum electron line density necessary for a meteor to be detected.

2.3.4 Observed detection rates

The number of meteors detected by a radar at a specific location over some period of time depends on a number of factors. The influx of meteoroids into the atmosphere varies as the sporadic background is augmented by the passage of discrete, shower-causing streams. Seasonal variations in the count rates are introduced by the changing geometry of the observing radar's field of view with respect to different incident sources throughout the duration of Earth's orbit. Additional seasonal variation is introduced by seasonal changes in the density and temperature of the atmosphere, the overall effect of which increases as the observing radar's location approaches the poles.

The observed rate of meteor detections is also strongly governed by the radar parameters. Equation 2.13 indicates that sensitivity of a radar is proportional to the receiver gain and inversely proportional to the transmitted power. Thus, differences in the transmitted power of different systems with otherwise similar configurations can have a significant effect on the observed rate of detections.

Figure 2.7 shows the detection rate for the year 2009 observed by the Davis Station 33 MHz meteor radar, which is equipped with a 7.5 kW solid state transmitter. Under ideal conditions, this particular system is capable of detecting in excess of 15,000 underdense meteors per day. The detection rate of this system is dominated by a

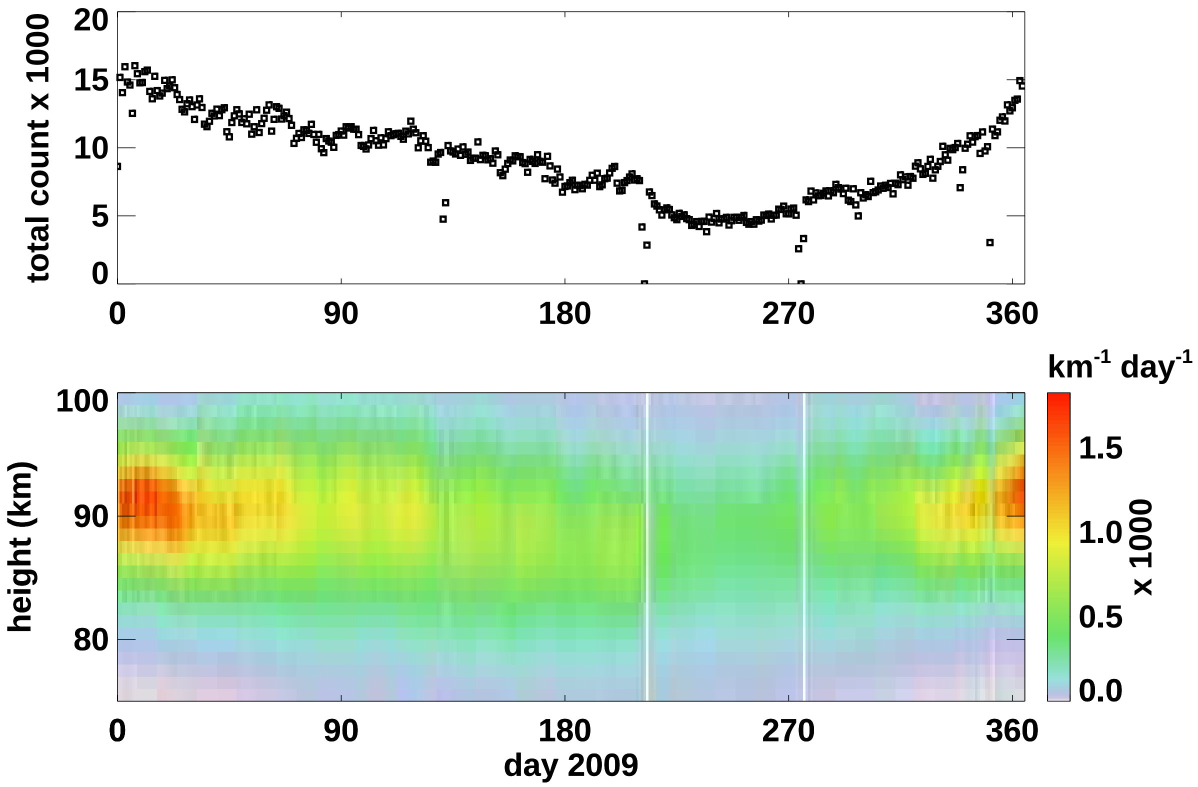

Figure 2.7: Top: Total daily counts detection density for Davis Station, Antarctica 33 MHz meteor radar. Bottom: Density of detections with respect to height.

seasonal variation caused by the movement of the radar's field of view throughout the year. In summer and autumn, the radar achieves its maximum detection rate as the South Pole is tilted towards the strong sporadic sources located in the orbital apex and antihelion direction. Spring sees the minimum count rate as the southern polar region is tilted away from Earth's direction of orbital motion and is shielded from the dominant sources of sporadic meteors.

Also of note is the height distribution of meteor detections in the atmospheric column, which changes with seasonal and dynamic changes to the density and temperature of the upper atmosphere. Meteors are detected at lower altitudes in the winter months. This is a result of the increased temperature in the winter mesosphere, which results in lower atmospheric densities. This permits meteoroids to travel deeper into the atmosphere before producing detectable ionization. The observation of these phenomena are dependent on the accurate knowledge of the height at which detected meteor trails occur. Factors influencing the positional accuracy of a meteor radar are now examined to determine to what degree height estimates may be relied upon.

2.4 Antenna Mutual Coupling

The angle-of-arrival estimate from an interferometric antenna array relies on the assumption that the voltage measured at each receiving antenna is a true representation of the incident electric field. This requires that each antenna of the array functions as an isolated system, i.e. without input from the fields present on the surfaces of the other antennas in the array. In reality, as an incident electromagnetic wave interacts with an antenna, it generates a current along the length of the antenna, which in turn gives rise to an electric field. This field can then induce a current in other antennas, producing a coupled system.

The measured voltage V_i at antenna i is then given by

$$V_i = \sum_j Z_{ij} I_j \tag{2.14}$$

where Z_{ij} is the matrix of impedances between antennas i and j and I is the current in antenna j (see, e.g., Balanis [2005]). While the spacing of antennas in the meteor radar receiving array significantly reduces the effect of mutual coupling, there is still a small effect.

2.4.1 Measurement of Mutual Coupling

It is possible to quantify the impact of mutual coupling on an antenna array by directly measuring the coupling between antennas and calculating the angle-of-arrival that will be estimated for an incident wave of a given true angle-of-arrival. Thus, the impact of coupling can be assessed and steps taken to mitigate or correct the impact on observations.

The Buckland Park meteor radar receive array was assessed for the effects of mutual coupling by measuring the scattering parameters for the antennas, as shown in table 2.4.1. An Agilent E5061A vector impedance meter was used to measure the s-parameter for each antenna and each possible pair of antennas.

The s-parameters describe the propagation of signals in the array. The elements along the diagonal of the s-parameter matrix represent the amount of signal that is reflected back from a signal input into the antenna. Off-diagonal elements of the s-parameter matrix represent the gain of a signal transmitted between the two antennas [Anderson et al., 1997].

Due to the construction of the connections of the feed cables to the transmit antenna, it was not possible to perform a nondestructive inspection, so the transmit antenna was not included in the measurements. While the transmit antenna will contribute to mutual coupling in the array, its location on the periphery and the number of receive antennas should reduce the impact of the absence of the transmit antenna from the analysis. The final estimate of the effect of mutual coupling from each antenna is obtained from the multiplication of a vector containing the instantaneous incident radiation at each antenna and matrix of coefficients describing the magnitude of mutual coupling. The final summation includes six terms, only one of which belongs magnitude (dB)

ant.	0	1	2	3	4
0	-20.9	-35.8	-38.2	-39.3	-36.7
1	-35.8	-23.6	-45.8	-44.0	-43.0
2	-38.2	-45.8	-29.6	-46.7	-44.6
3	-39.3	-44.0	-46.7	-22.4	-47.9
4	-36.7	-43.0	-44.6	-47.9	-23.2

phase (degrees)

ant.	0	1	2	3	4
0	92.9	-32.6	149.7	-29.2	142.0
1	-32.6	88.1	157.2	9.3	-43.0
2	149.7	157.2	63.4	56.7	-44.6
3	-29.2	9.3	56.7	61.5	-24.4
4	142.0	-43.0	-44.6	-24.4	87.0

Table 2.2: S-parameters measured for the receive array antennas of the Buckland Park meteor radar. The array is configured as depicted in Figure 2.1 with antenna 0 in the center, crossed by antenna pairs 1/2 (E-W) and 3/4 (N-S), with antennas 1 and 4 having 2.5 λ separation from antenna 0 and the transmit antenna located in the southeast corner nearest antennas 2 and 3.

to the transmit antenna. Therefore, the five coefficients of the closely spaced receive array should dominate the mutual coupling process.

The resultant s-parameter matrices consist of both a magnitude and phase, reflecting the complex nature of the related impedances. The matrices are symmetric due to the reciprocal relationship between the antennas of each possible pair. This equivalence was verified during the measurements.

The matrices shown in Table 2.1 represent a single matrix $\mathbf{S}$ of complex s-parameter values. These values can be used to obtain the matrix of impedances $\mathbf{Z}$ between antennas using the relationship

$$\mathbf{Z} = Z_L \left[\left(\mathbf{E} - \mathbf{S} \right) \left(\mathbf{E} + \mathbf{S} \right) \right]^{-1}, \tag{2.15}$$

where $\mathbf{E}$ is the identity matrix. Z_L is the impedance of the loads to which the antennas are attached. It has a value of 50Ω.

For a given voltage, the induced current can be expressed as a function of the matrix of admittance parameters $\mathbf{Y} = (Z_L\mathbf{E} + \mathbf{Z})^{-1}$. $\mathbf{Y}$ plays the part of $1/R$ in the basic form of Ohm's law. Current is then given by $\mathbf{I} = \mathbf{YV}$ [Anderson et al., 1997].

Using the above definitions, the observed voltage on an array $\mathbf{V}_O$ can be calculated from the incident voltage $\mathbf{V}_A$ as

$$\mathbf{V}_O = Z_L\mathbf{EYV}_A. \tag{2.16}$$

The phase of the observed voltage can then be used to calculate an estimated angle-of-arrival as described by equation 2.1.

2.4.2 Impact of Mutual Coupling on Positional Accuracy

This was done using the measured s-parameters in Table 2.4.1 for the Buckland Park meteor radar in order to determine what effect, if any, mutual coupling of antennas has on the angle-of-arrival estimates produced by the array. Of particular interest is to what degree mutual coupling between antennas affects the meteor detection height estimates produced by the array, as positional accuracy is essential to the accurate determination of gravity wave fluxes using meteor wind measurements [Vincent et al., 2010].

Equation 2.16 was used to calculate the predicted observed voltage with coupling for simulated meteor detections located across the sky map. The angle-of-arrival calculated from the observed voltage was compared with the angle-of-arrival of the incident waves to produce a map of zenith errors, shown in Figure 2.8.

It was found that mutual coupling produced maximum zenith angle estimate errors near the horizon. There is some fine structure in the error estimate map, due to the projection of the coupling process with five degrees of freedom onto the domain of the angle-of-arrival estimate, which has two degrees of freedom. Overall, the error presents as a gradient along the array's north-south axis. The maxima of the errors lie on the horizon with a magnitude of about 0.4°. For a meteor at 90 km and an extreme viewing angle of 75° zenith, this produces an error in the height estimate of about 2.1 km. Around the peak detection zenith of about 60°, the zenith error rarely

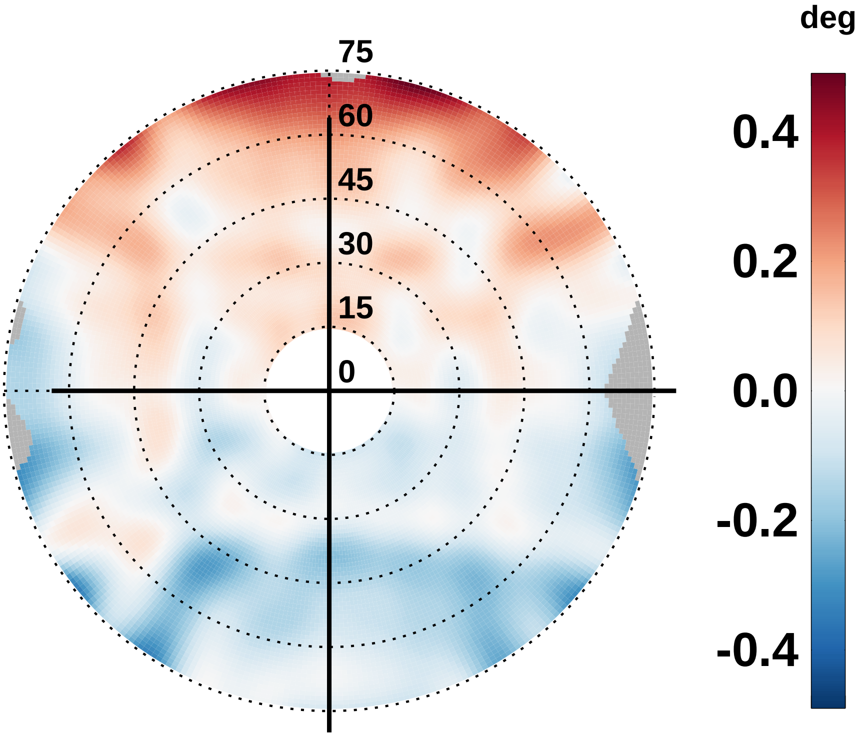

Figure 2.8: Skymap of zenith angle errors due to coupling between antennas of the Buckland Park meteor radar's receive array. Gray regions indicate unresolvable angles of arrival. Bold lines depict the interferometer baseline geometry.

exceeds 0.2°, corresponding to a height estimate error of about ±1.1 km.

Two points should be considered in assessing whether the observed antenna coupling has an appreciable impact on observations. First, the magnitude of the resultant errors are small in comparison to those introduced by uncertainty in the angle-of-arrival and range to the meteor. Secondly, the gradient seen in Figure 2.8, which is the most prominent feature produced by coupling, will be removed by phase calibration performed across the entire receiver signal path. Thus, while antenna coupling does have some effect, it is either mitigated by calibration processes or is not significant enough to adversely affect observations.

2.5 Calibration

Interferometric meteor radars suffer from the same key uncertainty common to any electronically steered radar: how does one know that the angle-of-arrival (or transmission in the case of a phased array radar) indicated by the radar is the actual angle-of-arrival of the incident scattered signal? While the system itself provides a reliable method for the conversion of phases to angles of arrival, the measurement of phase itself needs to be verified. Even small biases of a few degrees in the measurement of a signal's relative phase can have a dramatic effect on the recorded observations, skewing the entire distribution of detections across the sky and shifting the estimates of meteor detection heights by up to several kilometers.

2.5.1 Meteor echo phase calibration

Holdsworth et al. [2004b] present a method for estimating the phase biases of each antenna pair of a meteor radar by applying a statistical analysis of the phases of individual meteor echoes. Using Equation 2.1, the observed phase χ' with measurement bias α is given by

$$\chi' = \chi + \alpha. \tag{2.17}$$

This observed phase then produces a set of flawed angle-of-arrival candidate values Ψ'. For two antenna pairs j and k along the same baseline, one candidate value can be selected arbitrarily to construct the quantity

$$X_k = \frac{2\pi}{\lambda} d_k \sin \psi'_j, \tag{2.18}$$

which is the phase at antenna pair k for the angle-of-arrival candidate value ψ'_j. This leads to the quantity

$$\gamma_k = X_k - \chi'_k = \frac{d_k}{d_j} \alpha_j - \alpha_k, \tag{2.19}$$

which leads to a new phase:

$$\chi''_k = \chi'_k - \gamma_k. \tag{2.20}$$

This in turn produces a new set of candidates for the angle-of-arrival, Ψ_k. There is then one unambiguous angle-of-arrival ψ' that is present in both Ψ'_j and Ψ''_k. ψ' can then be inserted into Equation 2.18 to determine the value of γ_k. Following the collection of a number of estimates for γ, the optimal value can be selected by fitting a Gaussian distribution to the histogram of estimates. The values of γ can then be used to infer the measurement biases α_j and α_k. Simulations indicate that this method is capable of determining phase measurement biases to within ±2°.

2.5.2 Correction using geophysical data

The method described in 2.5.1 provides the most direct method of estimating systematic errors in phase measurements in all the receiver channels, but it requires that the phase information for each channel be recorded for every detection. While the increase in data storage capabilities in recent times may make this practically feasible, the calibration has traditionally been done at the time of the initial analysis, after which the original receiver channel time series have been discarded to free up storage space. Additionally, there is the issue of how to reconcile the newer calibrated data with older, uncalibrated data sets.

What is needed therefore, is some method of calibrating existing data, using only those parameters which are available in the data set of analyzed detection summaries.

Such a practice constitutes a post statistical steering method [Kudeki and Woodman, 1990], to which meteor radar data is particularly well suited.

As the ambipolar diffusion coefficient (discussed in chapter 6) is a function of the local atmospheric temperature and density, and can be obtained from the decay time of meteor radar echoes, D can be used to assist in the assessment of phase errors without the original individual channel phase data.

One such method assumes that $\log_{10} D$ varies linearly with height and fits a plane to the Cartesian coordinates of an ensemble of meteor detections by selecting the values a, b, c, and d so as to minimize the quantity

$$\delta = \sum \left(ax + by + cz + d - \log_{10} D_n\right)^2 . \tag{2.21}$$

This process consists of adjusting the angle and height of a series of equi-D planes [Holdsworth et al., 2004b]. The coefficient d sets the central height of a given equi-D plane, the coefficients a and b serve to tilt the equi-D plane, and c controls the gradient of $\log_{10} D$ with respect to height.

This method suffers from two limitations. Firstly, it assumes that $\log_{10} D$ is strictly linear in its height dependence, which is not necessarily always the case. In fact, there can be significant curvature, especially below 85 km [Younger et al., 2008]. Secondly, the use of planes in the fit, although mathematically expedient, ignores the non-negligible curvature of the atmosphere. Such an assumption results in large errors in the assumed height for meteors with large zenith angles. This effectively assigns an erroneously large weighting for detections near the horizon in the least squares fit.

2.5.3 Equi-D shell fitting

An alternative method was developed to use diffusion coefficients of approximately the same value to fit curved shells of height data, as opposed to planes. This has the additional benefit that the errors in the phase estimates of the baseline can be directly solved for.

It is first assumed that all meteors with the same estimate of the diffusion coefficient obtained from the echo decay time occur at the same height. Detections are separated into bins by their value of D and the following analysis is applied to each bin.

Substituting the expression for the phase differences along each baseline for the angles to the baselines, Equation 2.2 becomes

$$\begin{aligned}\cos^2\theta &= 1-\cos^2\left[\sin^{-1}\left(\frac{\chi_1\lambda}{2\pi d}\right)\right]-\cos^2\left[\sin^{-1}\left(\frac{\chi_2\lambda}{2\pi d}\right)\right] \\ &= \left(\frac{\chi_1\lambda}{2\pi d}\right)^2+\left(\frac{\chi_2\lambda}{2\pi d}\right)^2-1. \qquad (2.22)\end{aligned}$$

Substituting this expression into Equation 2.4 and including phase errors α_1 and α_2, a meteor's estimated height can be described

$$h=\sqrt{R_e^2+R^2+2RR_e\sqrt{\frac{\lambda}{2\pi d}\left(\chi_1+\alpha_1\right)^2+\frac{\lambda}{2\pi d}\left(\chi_2+\alpha_2\right)^2-1}}-R_e. \qquad (2.23)$$

The bias terms α_1 and α_2 can then be directly obtained by a least squares curve fitting algorithm so as to minimize the quantity $\sum\left(\bar{h}-h_i\right)^2$. Once the bias in the phase difference estimate is known, the corrected phase differences can be used to determine the true angle-of-arrival.

2.5.4 Effectiveness of equi-D shell fitting

The effectiveness of equi-D shell fitting as a means of estimating phase measurement biases was first tested using simulated meteor detections. A distribution of simulated meteor detections was constructed by assuming a linear relationship between height and $\log_{10} D$. Simulated meteors were then assigned true heights in a 6 km wide Gaussian distribution around 90 km, which is a reasonable approximation of what is seen in actual observations.

Random errors were inserted into the simulated distribution in the form of range errors, which were assigned a standard deviation of 1.8 km, and random errors in the phase measurement for each baseline, which were assigned a standard deviation of 10°. Both these values are in keeping with the precision of the radar systems used in this study. Systematic errors were then introduced by placing fixed phase offsets in the phase measurements of each baseline.

The simulated data were then used to test the method's capabilities on three criteria. If equi-D shell fitting is a viable means of determining phase errors, then it should return an accurate value of the inserted phase bias after analysis of the simulated data. Also of interest is how many detections are necessary to accurately apply the calibration method. Applying the method to smaller time bins restricts the possible temporal variation in D, but fewer detections may not be sufficient to accurately estimate what, if any biases are present in the measurements of phase. Finally, it is important to know what the overall precision of the method is, given a large number of detections under ideal conditions.

The results of the simulation, shown in Figure 2.9, indicate that equi-D shell fitting is accurate to within about 0.5° (root mean square deviation) with a minimum sample size of 1500 meteor detections. The detection number threshold of the predictions is similar to the precision achieved using the Holdsworth method, as shown in figure 9 of Holdsworth et al. [2004b]. With this prediction, the method should be more than adequate for estimating phase biases on timescales down to several hours. It should however be noted that this simulation assumed a fixed distribution of diffusion coefficients, while in practice geophysical variations will reduce overall precision.

An opportunity for a real world comparison of the equi-D shell fitting method with another calibration method is present in the July 2007 observations of the Darwin meteor radar. It was noted during normal operations in early August 2007 that the sky map of detections of the Darwin meteor radar were significantly skewed in one direction on the skymap, indicating a possible problem with the angle-of-arrival estimates. Meteor echo phase calibration as described by Holdsworth et al. [2004b] was implemented on 9 July, 2007 (day 191 in figure 2.10), resulting in the return of detections to the appropriate distribution.

This scenario allows a direct comparison of the behavior of equi-D shell fitting with meteor echo phase calibration. An application of the equi-D shell fitting method should return a significant bias estimate from before calibration was performed and little or no bias after calibration was implemented. The results, shown in Figure 2.10,

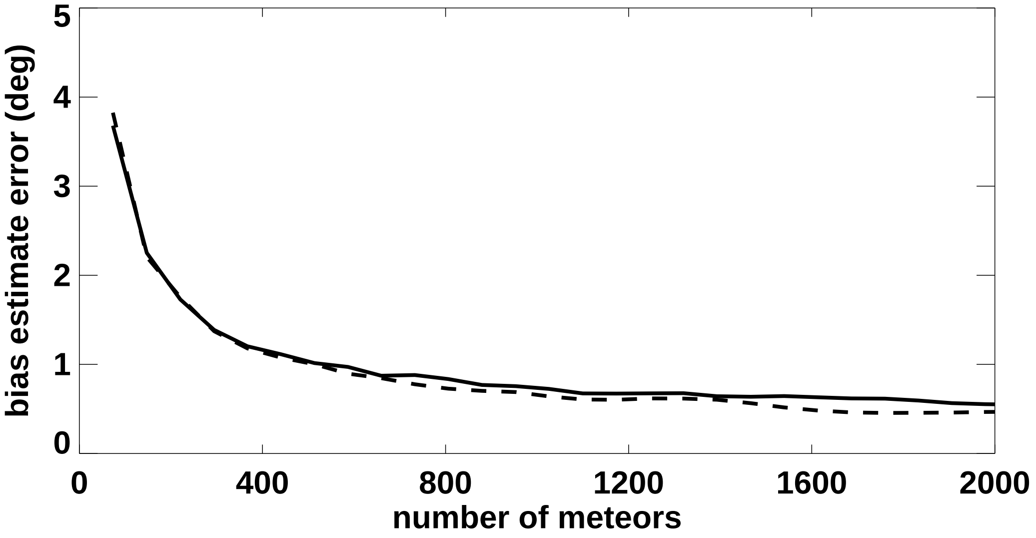

Figure 2.9: Accuracy of biases estimated from ensembles of simulated detections. Average of 100 simulations is shown for 10° (solid) and 0° (dashed) phase measurement bias.

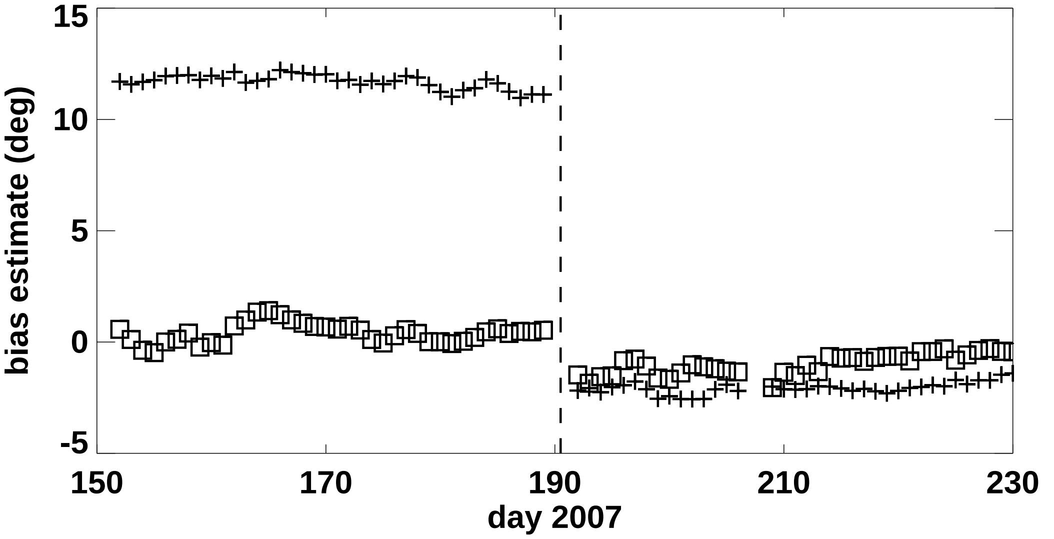

Figure 2.10: Equi-D shell fit estimates of phase measurement bias (three day smoothed) along the Darwin meteor radar's N-S (crosses) and E-W (boxes) 4.5 λ baselines. The dashed line indicates the date a Holdsworth type statistical calibration was performed.

indicated that prior to meteor echo phase calibration, there was a phase measurement bias of approximately 12° for the Darwin meteor radar along the N-S 4.5λ baseline. Following calibration, the equi-D method returned bias estimates on the order of $\leq 1°$.

Given the results of simulations shown in Figure 2.9, the comparison indicates that equi-D shell fitting produces comparable results to meteor echo phase calibration. Good agreement is shown in the post-calibration bias estimates, and correction of pre-calibration observations using equi-D shell fitting produces detection distributions consistent with post-calibration observations.

For calibration purposes, the meteor echo phase calibration described by Holdsworth et al. [2004b] remains the most rigorous method of estimating biases in the phase measurements used to estimate angle-of-arrival, due to its lack of reliance on variable geophysical parameters. The dependence of this method on the phase data recorded for each receiver channel, however, means that it cannot be implemented for observational data that does not contain phase information. The equi-D shell fitting method is then a viable method to perform a reasonably precise calibration of existing data sets, without the need for the original phase data. This allows older data sets to be integrated with current studies using a single consistent calibration method.

2.6 Summary

Interferometric meteor radars provide an all-weather, day/night capability to observe meteor trails in the upper atmosphere. The integration of the observations of meteor trails into a picture of the dynamic processes in the upper atmosphere requires that the accuracy and limitations of radar systems are known. Of particular importance to atmospheric observations is the accuracy of the height estimate for each meteor detection.

Overall accuracy has been examined, following the sources of errors in the measurement of phase differences between antennas, through the estimation of angle arrival, and the final estimation of the height of the meteor detection. Two sources of systematic error in angle-of-arrival estimates have been considered: bias in the measurement of phase differences and mutual coupling between antennas.

The effect of mutual coupling between antennas is removed during normal calibration processes or is so small as to be insignificant compared to random errors in the phase measurement. It has therefore been shown to not contribute appreciably to errors in the estimate of meteor detection height.

An improved method of calibration has been developed and demonstrated using meteor decay times. It is assumed that the diffusion coefficient responsible for the decay of a meteor radar echo varies uniquely with height. Meteors with the same decay time are then assumed to occur at the same height. An appropriate phase measurement bias is then determined to correct the data to this condition. Simulations of the performance of this method and a comparison with existing calibration methods indicate that this method produces estimates of the phase measurement bias accurate to within 1°. This method provides a means to calibrate older data sets for which the original phase data is not available.

With an understanding of the methods used to observe meteor trails using interferometric meteor radar, an examination of meteors and their interaction with the atmosphere can begin in earnest. The capabilities of the radar will then be combined with the behavior of meteors to provide a foundation to interpret meteor radar observations. The following chapter will examine the factors that determine the characteristics of meteor trails, which will be used to investigate the properties of meteor echoes.

Chapter 3

Atmospheric Entry and Meteor Ablation

A meteoroid entering the atmosphere collides with atmospheric molecules, which results in heating of the meteoroid and sputtering of molecules from its surface. If the meteoroid is heated sufficiently, the surface can vaporize. The combination of evaporated and sputtered material left in the wake of an ablating meteoroid can then be ionized by further collisions with atmospheric molecules. The free electrons in the meteor trail provide point scatterers for observation by radar.

An understanding of the processes occurring during meteoroid ablation is a critical step towards understanding the formation of radar echoes from meteor trails. Using a few relations and an *a priori* knowledge of the properties of the most common meteoric materials, it is possible to model the evolution of a meteor trail, as the body is heated, evaporation occurs, and a column of ionization is formed. In this chapter, the work of Love and Brownlee [1991] has been followed, with improvements made in the areas of computational accuracy and the addition of sputtering. Fragmentation has not been considered in the ablation process (see, e.g., Campbell-Brown and Koschny [2004]), but will be discussed in regards to the impact on the formation of radar echoes in section 5.4.5.

Taking an additional step, we can invert the relation. Rather than considering the atmosphere as a passive host to the trails of passing meteors, we can consider it an active participant in the ablative behavior of entering meteors. As the density and density gradient of the atmosphere vary, so too should the observed distribution of meteors with the same initial velocity in the atmosphere. As such, the distribution of detected meteors can provide additional information about the conditions of the upper atmosphere.

3.1 Meteoroid Entry into the Atmosphere

The mean free path of molecules in a gas is given by

$$l = \frac{kT}{\sqrt{2}\pi d^2 p}, \tag{3.1}$$

where k is the Boltzmann constant, T is the temperature, d is the mean diameter of the molecules, and p is the pressure. Around a typical lower meteor ablation altitude of 80 km, the temperature is about 200K and the pressure is about 2 Pa. Under these conditions, the mean free path is approximately 1 cm and small bodies interact with the atmosphere through elastic collisions.

For the comparison of the mean free path of a gas with the radius r of a spherical particle passing through it, the Knudsen number given by $k_n = l/r$ provides a useful criterion. When $k_n \gg 1$ the gas/meteoroid interaction can be considered to be within the free molecular flow regime. At smaller values of k_n, hydrodynamic phenomena including the formation of a bow shock of compressed atmospheric gas ahead of the meteoroid can not be ignored [Coulson, 2002]. The meteoroids considered in this study are restricted to those with $r \leq 500\mu$m, indicating that their interaction with atmospheric molecules is strictly one of classical collisions.

When a meteoroid collides with atmospheric molecules, a portion of its kinetic energy is transfered to the atmosphere, reducing the velocity of the meteoroid. The velocity of a spherical meteoroid of density ρ_m with instantaneous velocity v passing through an atmosphere of density ρ_a is then changed at a rate given by

$$\frac{dv}{dt} = -\frac{3\Gamma\rho_a v^2}{4\rho_m r} + g, \tag{3.2}$$

where g is the acceleration due to gravity. Γ is the drag coefficient, which describes the efficiency of momentum transfer between the meteoroid and the atmosphere [Love and Brownlee, 1991]. Given that meteoroid velocities are on the order of tens of kilometers per second, the gravitational component is negligible throughout the ablation phase, although it will affect the trajectory of the body over the course of the entire infall process.

3.2 Thermal Effects

A meteoroid with cross-sectional area $s = \pi r^2$ traveling at velocity v sweeps out a volume $sv\Delta t$ in time Δt. Thus, collisions with atmospheric molecules deposit energy into a spherical body at a rate given by

$$P_{in} = \frac{\Lambda}{2}\rho_a \pi r^2 v^3, \tag{3.3}$$

where Λ is the heat transfer coefficient, which is a measure of how efficiently the kinetic energy of incident particles is converted to thermal energy in the meteoric material upon collision. The energy deposited by collisions with atmospheric molecules is shared among three processes: raising the temperature of the material, radiation, and vaporization of meteoric material.

For a spherical body, the power used to change the temperature of the material is given by

$$P_h = -\frac{4}{3}\pi r^3 \rho_m c_p \frac{dT}{dt}, \tag{3.4}$$

where c_p is the heat capacity of the material. Love and Brownlee [1991] show that for a relatively slow meteor traveling at 12 km/s, the energy required to heat the body to 1500 K is significantly less than 1% of the initial kinetic energy. Therefore, they neglect heating in the solution to the meteoroid's energy budget. This allows for the heating and entry process to be modelled with more computationally expediant methods, but neglects important early entry behaviour at low temperatures, as will be shown in section 3.5.

For meteoroids with a diameter of less than ≈ 1 mm, it can be assumed that the particle is isothermal for the entire process and that no significant thermal gradients are present in the material. The validity of this assumption can be assessed by means of the Biot number, $Bi = hr/3K$, where r is the particle's radius and K is the thermal conductivity. The heat transfer coefficient $h = \sigma T^3$ expresses the transfer of heat between the particle and its surroundings. Kakaç and Yener [1985] show that objects with a Biot number less than 0.1 are effectively isothermal, allowing the effects of conduction to be neglected in the calculation.

For a typical olivine meteoroid melting point of approximately 1500 K with an estimated thermal conductivity of 2 W K^{-1} m^{-1} [Öpik, 1958], the diameter at which conduction becomes important is then approximately 6.3 mm. At a superheated extreme temperature of 2000 K, this diameter is reduced to 2.7 mm. Love and Brownlee [1991] find the diameter to be an order of magnitude lower, which is due to their choice of an extremely conservative K value of 0.2 W m^{-1} K^{-1}. Therefore, by restricting consideration to particles of 1 mm diameter and under, the effects of thermal conduction may safely be ignored and the meteoroid can be considered to be isothermal throughout the heating and ablation process.

Meteoroids radiate energy at a rate given by

$$P_{rad} = -4\pi r^2 \epsilon \sigma \left(T^4 - T_a^4 \right), \tag{3.5}$$

where σ is the Stefan-Boltzmann constant, ϵ is the particle's emissivity, and T_a is the temperature of the atmosphere. ϵ varies with the body's composition and surface roughness, but for the purposes of calculation it is assumed to be unity. This approximation is adequate due to the relatively minor effect overall of emissivity in comparison with the rapid onset of vaporization around the material's boiling point and the relatively high energy loss with evaporative processes, which is illustrated in

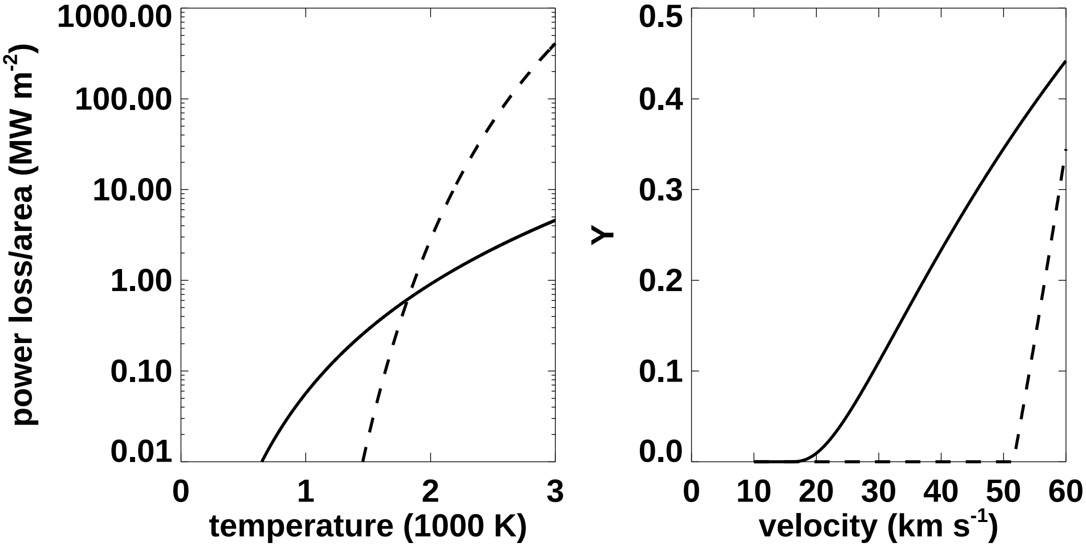

Figure 3.1: Left: Power lost due to radiation (solid) and evaporation (dashed) for an olivine type stone composition meteoroid. Right: Sputtering coefficient Y, the ratio of sputtered particles to incident particles, as calculated by Tielen's method using equation 3.18 (solid) and Öpik's method given by 3.10 (dashed).

figure 3.1.

Power lost to vaporization at temperature T is given by

$$P_{vap} = h_v \frac{dm_{th}}{dt}, \tag{3.6}$$

where h_v is the latent heat of vaporization and dm_{th}/dt is the rate of mass loss. Evaporation to a vacuum is assumed, given the free molecular flow environment of the low atmospheric density regime as defined with k_n in section 3.1. The rate of mass loss due to thermal evaporation, dm_{th}/dt, is expressed as a function of the saturated vapor pressure in a vacuum environment, p_v,

$$\frac{dm_{th}}{dt} = -4\pi r^2 C_L p_v \sqrt{\frac{m_{mol}}{T}}, \tag{3.7}$$

where $C_L = (2\pi R)$, R being the universal gas constant, is Langmuir's constant and m_{mol} is the mass per mol of meteoric material. The vapor pressure, p_v, may be calculated by means of the Antoine equation given by

$$\log_{10} p_v = A - \frac{B}{T - C}, \tag{3.8}$$

where A, B, and C are empirically derived constants specific to the material [Langmuir, 1913].

3.3 Sputtering

Mass loss in a body entering the atmosphere is not restricted solely to thermal evaporation. It is also possible for atmospheric molecules to impact with sufficient energy to eject molecules from the surface of the meteor without the meteoroid being in an evaporative temperature regime. Sputtering, as this mechanism is called, is possible whenever the kinetic energy of the impinging atmospheric molecules exceeds the surface binding energy, U_0, of the meteoric material. This can result in non-negligible mass loss at much greater altitudes than those associated with thermal ablation only (see, e.g., Rogers et al. [2005]).

The rate of mass loss due to sputtering is given by the general expression

$$\frac{dm_{sp}}{dt} = -2\pi r^2 v M_2 \sum_i \rho_i Y_i \left(E_i, \theta = 0\right), \tag{3.9}$$

where ρ_i is the density of the ith atmospheric constituent, θ is the angle between the path of the incident particle and the surface normal, and M_2 is the mean molecular mass of the sputtered material. Y_i is the sputtering yield which expresses the number of meteoric molecules sputtered per impinging molecule [Tielens et al., 1994].

The sputtered yield is necessarily dependent on the incident angle of impinging molecules. Particles incident near the normal are more likely to embed themselves in the lattice of meteoric molecules without actually ejecting material from the body, whereas incident molecules grazing the edges of the body can dislodge significant numbers of molecules from the lattice. To account for this geometric dependence, a factor of 2 is introduced from the experimentally derived relation for the sputtering yield averaged over all angles of incident, so that $\langle Y(E)\rangle_\theta \approx 2Y(E, \theta = 0)$ [Draine and Salpeter, 1979]. Thus, only the normal incidence Y_i needs to be calculated to obtain the total sputtered yield estimate.

Several methods have been suggested for calculating Y, ranging from the simple approximation [Öpik, 1958] to a semi-empirical treatment covering most physical processes in the impactor-lattice interaction [Tielens et al., 1994]. We now briefly consider and compare these models to determine which is best suited to simulations of meteor sputtering.

3.3.1 Öpik's approximation

Öpik [1958] suggested an early model where the sputtering yield is given by

$$Y\left(E\right) = 5.3 \times 10^{-3} \kappa_n \left(E - 32U_0\right). \tag{3.10}$$

Here, κ_n is the accommodation coefficient for the particular combination of incident atom and meteor lattice atom, which describes the portion of incident particle kinetic energy that is transmitted to the lattice. Öpik [1958] provides values of κ_n of 0.924 and 0.650 for meteors of average stone composition and of pure iron, respectively. U_0 is the lattice energy, taken to be about 5.6 eV. This approximation is only valid when $E > U_0$ and produces a sudden onset of sputtering at around 51 km s^{-1} for a pure iron meteor and 42 km s^{-1} for an olivine stone meteor. The sputtering yield then follows a simple linear relation with the incident particle energy.

3.3.2 Semi-empirical formula

Tielens et al. [1994] provides a detailed derivation of the general form of sputtering yield for arbitrary incident and target species at normal incidence, given by

$$Y\left(E\right) = 4.2 \times 10^{14} \frac{\alpha S_n\left(E\right)}{U_0}, \tag{3.11}$$

where α is a function of the ratio of molecular masses between target and incident particles given by

$$\alpha = 0.3\left(M_2/M_1\right)^{2/3}, \tag{3.12}$$

where M_1 is the molecular mass of the incident (atmospheric) particles and M_2 is the molecular mass of the target (meteoric) material. Equation 3.12 is valid over the range

$0.5 < M_2/M_1 < 10$. For the case of $M_2/M_1 < 0.5$, α is approximately constant with a value of 0.2 [Rogers et al., 2005].

The form shown for α neglects surface effects, treating the depth of the target medium as infinite. Not accounting for electronic stopping at the surface prior to the onset of the cascade process within the material produces an excessive number of sputtered particles. This may be corrected by inserting a factor of the ratio of the mean projected range to the mean penetration length:

$$\frac{R_p}{R} = \left(K\frac{M_2}{M_1} + 1\right)^{-1}, \tag{3.13}$$

where K is a free parameter taken to be approximately 0.4 [Rogers et al., 2005].

Equation 3.11 presents the sputtering yield as a function of α, the surface binding energy U_0, and the nuclear stopping cross-section S_n. This last term can be calculated using the universal function, s_n, of the collision's reduced energy γ [Sigmund, 1969]:

$$S_n\left(E\right) = 4.2\pi a Z_1 Z_2 e^2 \frac{M_1}{M_1 + M_2} s_n\left(\gamma\right). \tag{3.14}$$

The screening length of the interaction potential is defined as

$$a = \frac{0.885 a_0}{\sqrt{Z_1^{2/3} + Z_2^{2/3}}}, \tag{3.15}$$

where a_0 is the Bohr radius and Z_1 and Z_2 are the incident and target particles' atomic numbers, respectively.

Matsunami et al. [1980] show that s_n can be approximated by the formula

$$s_n = \frac{3.441\sqrt{\gamma}\ln\left(\gamma + 2.718\right)}{1 + 6.35\sqrt{\gamma} + \gamma\left(-1.708 + 6.882\sqrt{\gamma}\right)}, \tag{3.16}$$

where the reduced energy of the interaction is given by

$$\gamma = \frac{M_2}{M_1 + M_2}\frac{a}{Z_1 Z_2 e^2}E. \tag{3.17}$$

Bohdansky [1984] makes two additional corrections to equation 3.14. Firstly, to account for the low energy regime where cascading molecules may not exceed the threshold energy, a factor of $1 - (E/E_{th})^{2/3}$ is inserted into S_n. Secondly, to account for non-isotropic momentum transfer, a factor of $(1 - E/E_{th})^2$ is added. With these corrections and inserting equations 3.12, 3.13, 3.16, 3.17, and 3.15 into equation 3.11, the sputtering yield at normal incidence is then

$$Y(E, \theta = 0) = \frac{3.56}{U_0} \frac{M_1}{M_1 + M_2} \frac{Z_1 Z_2}{\sqrt{Z_1^{2/3} + Z_2^{2/3}}} \alpha \frac{R}{R_p} s_n(\gamma) \left[1 - \left(\frac{E_{th}}{E}\right)^{2/3}\right] \left(1 - \frac{E_{th}}{E}\right)^2. \tag{3.18}$$

The threshold energy E_{th}, is the kinetic energy required for an incident molecule to remove a molecule from the target lattice. This term depends on the ratio of masses between incident and target molecules and can be calculated as

$$E_{th} = 8U_0 \left(\frac{M_1}{M_2}\right)^{1/3}, \tag{3.19}$$

for the case of $M_1/M_2 \geq 0.3$ [Andersen and Bay, 1981] and

$$E_{th} = \frac{U_0}{G(1 - G)}, \tag{3.20}$$

for $M_1/M_2 < 0.3$ Bohdansky et al. [1980], where the maximum fraction of energy that can be transferred in an elastic collision, G, is given by

$$G = \frac{4M_1 M_2}{(M_1 + M_2)^2}. \tag{3.21}$$

3.4 Ionization

The material ejected from the surface of the meteoroid by evaporation or sputtering is still traveling through the atmosphere at a speed comparable to the original velocity of the meteoroid. Subsequent collisions between these atoms and the incident atmospheric molecules can result in the ionization of one or both of the colliding particles. For the purpose of characterizing meteor trails, a useful measure of the ionization intensity is the free electrons per meter of axial length of the meteor trail. This is given by

$$q = -\frac{\beta}{M_2 v} \frac{dm}{dt}, \tag{3.22}$$

where β is the ionization efficiency, which describes the relative number of ionized atoms to vaporized atoms [McKinley, 1961].

Bronshten [1983] uses the Massey-Sida formula, combined with laboratory measurements of chonddritic material to produce the formula $\beta = 5.47 \times 10^{-7} v^{3.42}$. However, this approximation is suspect, because it requires that $\beta << 1$ and it does not take into account scenarios when the collisional energy of the particles does not exceed the energy required for ionization. Jones [1997] corrected for this, producing an approximate value for olivine type stone of

$$\beta = 9.4 \times 10^{-6} \left(v - 10\right)^2 v^{0.8}. \tag{3.23}$$

3.5 Numerical simulation

The preceding relations were used to numerically simulate the ablation of meteoroids in the atmosphere. Combining equations 3.3, 3.5, 3.6, and 3.4 the energy budget for a meteor is described by

$$\frac{1}{2}\Lambda \rho_a \pi r^2 v^3 = 4\pi r^2 \epsilon \sigma \left(T^4 - T_a^4\right) + h_v \frac{dm}{dt} + c_p m \frac{dT}{dt}. \tag{3.24}$$

The total mass loss, dm/dt is simply the sum of the evaporative and sputtering mass loss rates:

$$\frac{dm}{dt} = \frac{dm_{th}}{dt} + \frac{dm_{sp}}{dt}. \tag{3.25}$$

3.5.1 Linear integration method

Initially, the flight of a meteoroid through a model atmosphere and subsequent ablation was calculated using a hybrid Euler/4$^{\text{th}}$-order Runga-Kutta method. Heating, represented in the last term in equation 3.24, was neglected as suggested by Love and Brownlee [1991]. Deceleration, given by equation 3.2 was calculated using linear estimates over a small time increment, dt. Gravitational acceleration was ignored, given the negligible contribution over the several second passage of a bodies traveling at speeds in excess of the Earth escape velocity of 11.2 km s^{-1}. Once the new speed was obtained, the sputtering yield was calculated using equation 3.18.

As temperature cannot be obtained analytically from equation 3.24, it must be solved for numerically at each time step. This was done using Halley's method [see, e.g., Scavo and Thoo [1995]], with a tolerance of 0.001 K applied to the calculation.

Mass loss and the attendant reduction in particle radius were calculated using a 4^{th}-order Runga-Kutta method. Equations 3.7, 3.9, and 3.25 were calculated simultaneously over dt and the resultant particle mass used to obtain a new value for radius.

The results of this method of numerical simulation were compared with observations. It was found that the simulation predicted meteoric ionization to at several kilometers higher than is actually observed. It was determined that this was the result of ignoring the effect of heat capacity. While heating represents a small portion of the overall kinetic energy of the body, it is plays a significant role in the energy budget in the early stages of atmospheric entry when P_{in} is small. The contribution of a portion of input power to raising a body's temperature delays the overall heating process, which leads to a delay in the production of ionization.

3.5.2 Complete solution using Runga-Kutta 4^{th}-order method

In order to account for heating effects, it was necessary to solve for v, h, T, and m simultaneously. This was accomplished by integrating equations 3.2, 3.25, 3.7, 3.9, and the rate of temperature change given by

$$\frac{dT}{dt} = \frac{1}{c_p m}\left(P_{in} - P_{rad} - P_{vap}\right), \tag{3.26}$$

using a 4^{th}-order Runga-Kutta method.

This method fully accounts for the energy used in heating the particle and predicts the onset of ionization at several kilometers below that predicted by the simplified linear integration method, the effects of which are seen in figure 3.2.

The initial time increment was obtained from the formula $dt = dl/v_{init}$, where v_{init} is the meteoroid's initial velocity and dl is the minimum desired length traveled to perform the calculation over. A dl of 10 m was found to be more than adequate for the desired precision. In order to preserve the precision of the integrations during the

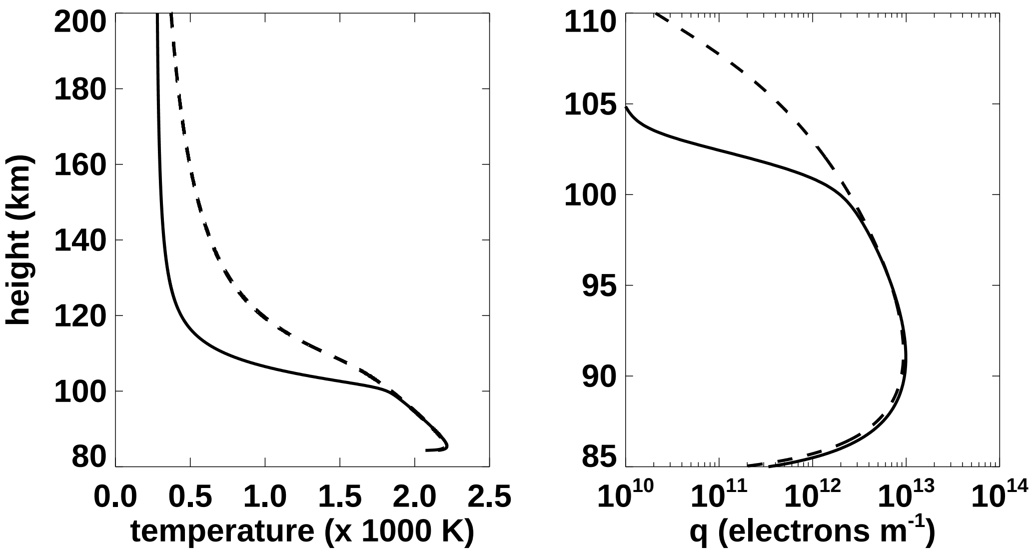

Figure 3.2: Temperature (left) and trail electron line density (right) for a 45° angle of entry, 500 μm diameter, 30 km s^{-1} initial velocity stony particle calculated using linear integrations, ignoring heat capacity (dashed) and a complete solution calculated using a 4th-order Runga-Kutta method (solid).

ablation phase where the meteoroid's mass is rapidly changing, an adaptive time step was used given by

$$dt' = cm \left(\frac{dm}{dt} \right)^{-1}, \tag{3.27}$$

where c determines the approximate maximum fraction of mass loss over an integration. dt' was used as the time step whenever $dt' > dt$. For the calculations described, $c = 0.0001$, which ensures mass loss at each time step is less than 0.1%.

Each simulated meteor was started at 180 km and the calculations were repeated until either the particle reached 50 km or one of three conditions was satisfied. A particle was considered to have survived the atmospheric entry process if its temperature was reduced to less than 0.2 times the maximum temperature achieved or if it was decelerated to less than 1 km/s. A particle with a mass reduced to less than 1.2×10^{-12} kg ($r \approx 10\mu$m) was classed as having been completely evaporated.

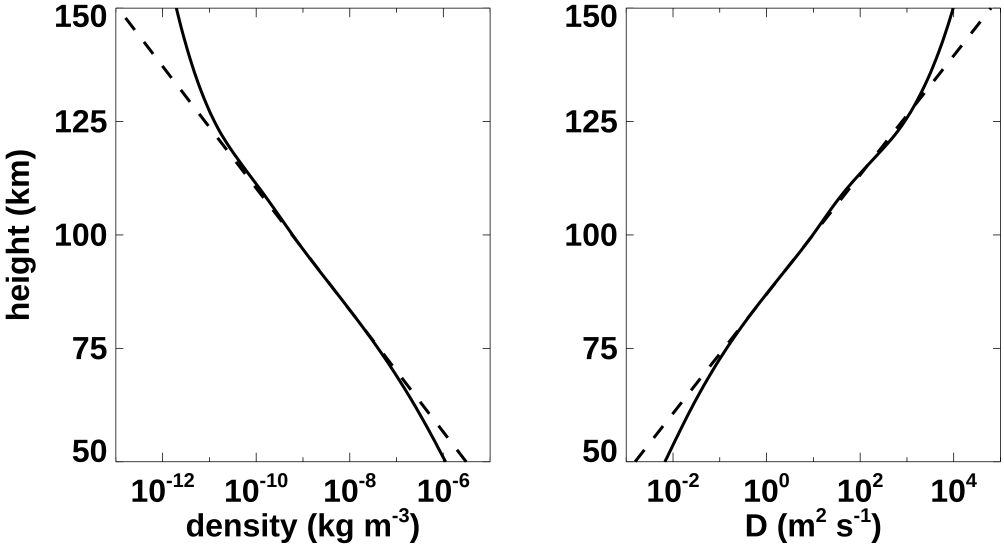

Figure 3.3: Comparison of atmospheric properties obtained from the NRLMSISE-00 model (solid) and a simplified exponential approximation (dashed) for Buckland Park, South Australia (34.6° S).

3.5.3 Model atmosphere

For an examination of ablative behavior and to determine the effect of the variation of different atmospheric properties, a simplified model atmosphere was used initially. The model atmospheric density ρ_a varies exponentially with height, according to the relation $\rho_a = \rho_{a0} \mathrm{e}^{-(h-h_0)/H^*}$, where h is the altitude, h_0 is the baseline altitude, ρ_{a0} is the density at the baseline altitude, and H^* is the density scale height.

Following the falling sphere measurements of Lübken et al. [2004] and the semi-empirical NRLMSISE-00 model, a value of $\rho_{a0} = 3 \times 10^{-5}$ kg m^{-3} at a baseline altitude of 80 km was chosen, although given the model's simplicity this choice is somewhat arbitrary and serves only to give a general association between altitude and meteoroid behavior. Variations in ρ_{a0} serve only to modify the overall height of meteor events, while it is H^* that influences the actual ablative behavior and overall shape of the observed meteor detection height distribution.

For a more detailed analysis, including the comparison of the predicted distribution of meteor radar detections with actual observations, the NRLMSISE-00 model was used. This model, maintained by the United States Naval Research Laboratory extends from ground level to the upper thermosphere and is an evolution of the previous MSIS-90 and MSIS-00 models, the most recent version being released in 2004. Data for the model is supplied by mass spectrometers, incoherent scatter radar, and more recently, observations of satellite drag [Picone et al., 2002]. Values of total atmospheric density were calculated at 1 km intervals for the three radar locations used for observations. In the ablative model, density values were estimated by a linear interpolation of the natural logarithm of the NRLMSISE-00 supplied density.

The primary difference between the two models, examples of which are shown in figure 3.3, is the assumption of a single scale height in the simplified exponential model. The NRLMSISE-00 model predicts an approximately constant scale height ranging between about 5-6.5 km below 100 km with a transition to a scale height of about 27 km above 130 km. This produces a much more gradual decline in density at higher altitudes, with a sudden increase in the density gradient descending below about 100 km. This added complexity produces subtle differences in the simulated ablative behavior of meteoroids. In the case were the density scale height at high altitudes is large, meteoroids will encounter higher densities for longer than with the simple exponential model. This manifests as an increase in the amount of sputtering, early low temperature heating, and in a higher altitude of peak temperature and mass loss.

In both models, for the calculation of the individual sputtering yields in equation 3.9, the atmospheric composition was set to a fixed mixture of 78% N_2, 21% O_2, and 1% Ar.

3.5.4 Meteoroid physical properties

Two types of meteoric composition were considered, that of an olivine stone and the special case of a pure iron particle. While the model of uniform meteoric materials used in these simulations lacks the sophisticated chemical processes modeled by Vondrak et al. [2008], the use of two distinct materials allows some basic observations on the effects of differential ablation to be made. For stony meteors, the thermal properties used were obtained from Öpik [1958]. Harwit [1973] supplied values for iron meteoroids.

3.5.5 Input meteoroid distributions

Initial velocities considered ranged from 15 km s^{-1}, just above Earth's escape velocity of 11.2 km s^{-1}, to 65 km s^{-1}, near the 72 km s^{-1} solar escape velocity and close to the maximum velocity that the Fresnel method as implemented is capable of resolving [Holdsworth et al., 2007]. For the purposes of obtaining simulated detection distributions, six velocities were used with a spacing of 10 km s^{-1}. The relative distribution of velocities for weighting of the final predictive product was taken from the cumulative distribution of observed velocities for one year at each of the sites considered.

The size of incident meteors was calculated from the model of Grün et al. [1985], which gives the annual flux of meteors of mass m at a distance of 1 AU from the Sun by

$$F(m) = \left(2.2 \times 10^{3} m^{0.306} + 15\right)^{-4.38} + 1.3 \times 10^{-9} \left(m + 10^{11} m^{2} + 10^{27} m^{4}\right)^{-0.36}. \quad (3.28)$$

The density assumed for the conversion of meteoroid size to mass was $3{\times}10^{3}$ kg m^{-3}, after the value for stony meteors supplied by Öpik [1958]. Initial calculations showed that under no circumstances were meteors with initial diameters of less than 200 μm detectable and that the population of detected underdense meteors has a peak initial diameter around 600 μm. Given this result, initial diameters between 200 and 1000 μm were supplied to the model, separated by 100 μm.

A uniform distribution of entry angles was assumed with five angles supplied to the model ranging from 15-75° at 15° intervals. Each angle of entry was then wieghted using the corresponding zenith angle gain obtained from modeling of the array using the antenna simulation program 4NEC2 [Voors].

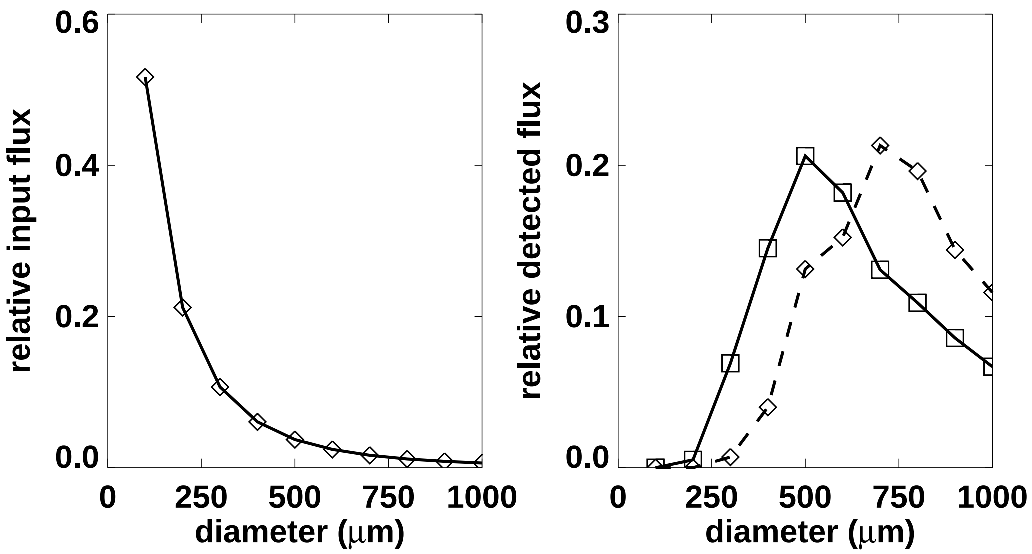

Figure 3.4: Left: Normalized annual flux of meteors incident on Earth obtained from equation 3.28. Right: Normalized distribution of the initial sizes of detected meteors from simulations for 33 MHz (solid) and 55 MHz (dashed) radars, following the application of individual meteor characteristic weighting and detection criteria. Distributions are averaged for one year's simulations at Davis Station, Antarctica.

Finally, the detectability of each individual meteor was determined by comparing the predicted electron line density of each trail with the minimum detectable line density given by equation 2.13. The initial radius term was calculated using the method of Jones [1995], which will be discussed in section 5.2.1.

3.5.6 General ablative behavior

For a given atmospheric profile, the ablation of a meteoroid is determined by its composition, size, initial velocity, and angle of entry to the local horizontal. Higher velocities result in higher ablation heights, as meteoroids are heated more rapidly by more frequent collisions with atmospheric molecules. At fixed velocities and entry angles the initial size of the particle determines the depth of penetration into the atmosphere and whether or not the particle will survive atmospheric entry without being completely vaporized.

The angle of entry has a more subtle effect, increasing the altitude of ablation as the angle of the meteoroid's path to the horizontal decreases. A smaller angle to the horizontal increases the effective scale height seen by the particle, considering scale height as a gradient in density not with height, but with distance along the path of the meteoroid. The additional time spent at higher atmospheric density early in the entry process for a shallow entry angle produces heating at higher altitudes, which raises the height at which the meteor begins to evaporate. Thus shallow entry angle meteors ablate at higher altitudes.

As the meteoroid passes through the low density thermosphere, heating of the particles is initially gentle. During this phase of flight, the mass loss mechanism is restricted to sputtering, which, as can be seen in equation 3.9, is proportional to atmospheric density. Following this slow heating, the temperature rapidly increases while the body passes through the higher densities below about 110 km. The rapidity of the heating in the mesosphere region produces a sudden onset of evaporative mass loss, resulting in a zone of the atmosphere between about 80-110 km where evaporated meteoric material is primarily deposited.

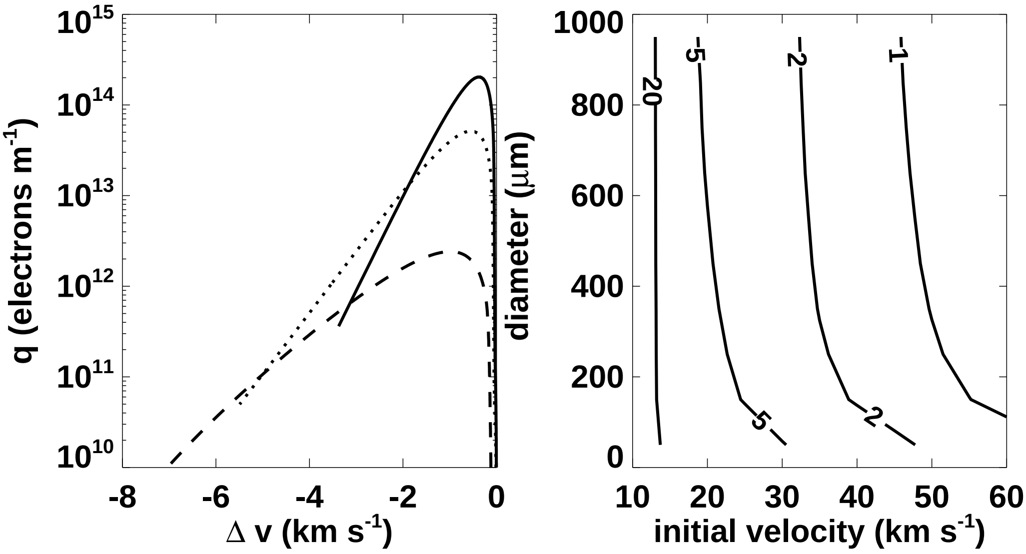

Figure 3.5: Left: Electron line density as a function of deceleration from initial velocity for 600 μm, 45° entry meteoroids with initial velocities of 60 (solid), 40 (dotted), and 20 (dashed) km s^{-1}. Terminated curves indicate the body evaporated completely. Right: Percentage deceleration from initial velocity at the point of maximum electron line density for 45° angle of entry meteors.

Of note is the distribution of initial sizes of meteors detected. Whereas the actual flux of meteors incident on the atmosphere is heavily biased towards small meteoroid masses, the initial size distribution of simulated meteors that satisfied detection criteria shown in figure 3.4 is significantly different. The resultant distribution of initial sizes for detected meteors peaks around 600 μm and declines to either side. The reason for the underrepresentation of small sizes as compared with equation 3.28 is due to a combination of two factors. Firstly, low mass particles experience greater deceleration earlier in the ablation process, due to the smaller ratio of mass to cross sectional area. The additional deceleration can slow smaller particles below ionizing velocities before they reach the denser mesosphere region. Secondly, due to the smaller surface area available for evaporation, small particles may not eject sufficient material for ionization to exceed the minimum detectable threshold q_{min}, even when significant mass loss at high velocity occurs well below the high altitude cutoff.

3.5.7 Deceleration

The difference between the observed velocity of a meteor and the velocity of the body when it initially entered the atmosphere is difficult to describe in general terms. Figure 3.5 shows the interplay between the initial conditions of different meteors and the possible observed velocities. Due to the number of different meteoric and atmospheric factors determining ablative behavior and the effect of the minimum detectable electron line density in the trail, it is not possible to say with certainty at what point in a meteor's ionization curve the specular detection point is located. The problem is further complicated in that the size of the meteoroid, which is one of the determining factors in its instantaneous deceleration, rapidly changes over the course of the evaporation process that produces detectable ionization.

One approximation is to choose a representative size meteor and define the deceleration as the difference between the initial velocity and the velocity at peak ionization. A function can then be constructed to estimate the original velocity of a particle prior to its entry into the atmosphere, based on the observed velocity at what is assumed to be peak ionization.

This was done for a 600 μm particle with an entry angle of 45° to the horizontal. The atmospheric profiles were taken from the annually averaged NRLMSISE-00 model for Buckland Park, South Australia. This site was chosen for its mid-latitude location, which upon analysis produced results that were in good agreement (within <1% for each coefficient) with the results from equatorial and polar locations. A parabola was fitted to the initial velocity as a function of the observed velocity at maximum electron density for the simulated meteoroids to produce the approximation,

$$v_i \approx 1.52 + 0.966 v_{obs} + 2.58 \times 10^{-4} v_{obs}^2, \tag{3.29}$$

where v_{obs} is the observed velocity of the meteor, defined by its velocity at peak ionization in km s^{-1}. While this simplifies the deceleration problem to that of a single size particle at a single point in its ionization curve, it does provide an improvement on uncorrected meteor velocity observations when seeking the original velocity prior to atmospheric entry. This is of particular importance for astronomical applications when attempting to ascertain orbital parameters associated with different meteor populations.

3.5.8 Significance of sputtering

Rogers et al. [2005] predicts that sputtering for particles in the typical underdense meteor mass range of 10^{-9}-10^{-6} kg with velocities in excess of 30 km s^{-1} will account for 10-20% of the total mass loss of the particle over the ablation process.

While this may be the case for meteoroids with extremely low density, or weakly bound CHON (volatile ices, see e.g. Rietmeijer [2004]) type particles, the simulation performed did not support these findings for stony meteoroids. Instead, the simulation predicted that only approximately 1-2% of mass would be lost due to sputtering for any meteor large enough to be detected, as can be seen in figure 3.6. This result is consistent with the findings of Vondrak et al. [2008], who considered a more thorough treatment of the ablation process, including differential ablation of different elements

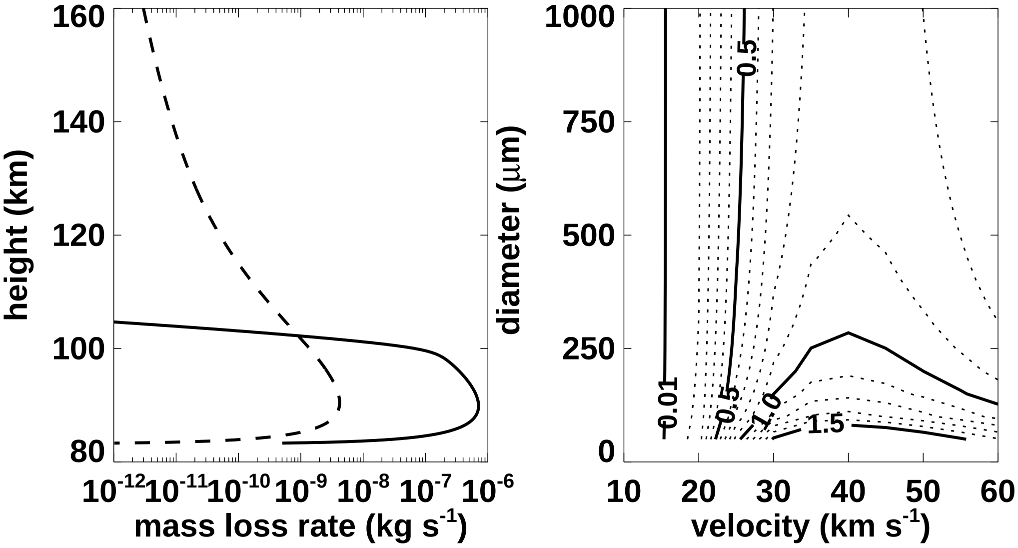

Figure 3.6: Left: Rate of mass loss for evaporative (solid) and sputtering (dashed) processes. The simulated meteor was calculated with a 600 μm initial diameter, an initial velocity of 40 km s^{-1}, and a 45° entry angle. Right: Percentage of total mass loss due to sputtering for meteoroids with a 45° entry angle. Dotted contours are 0.1% apart.

and the diffusion of different chemical species within the molten body.

The significance of the simulation results is that for the purposes of studying underdense meteor radar detections, sputtering plays only a minor, if not negligible, role in the formation of the ionization responsible for radio wave scattering. However, what should be noted is that for larger particles, sputtering may produce sufficient mass loss early in the ablation process to produce detectable ionization at higher altitudes than would otherwise be expected. This possibility is due simply to the larger amount of material sputtered from a larger surface. Ionization produced by the ionization of material lost to thermal evaporation would of course also see an attendant increase.

3.6 Summary

The evolution of a meteoroid as it interacts with the atmosphere is the culmination of the processes of sputtering, heating, radiation, and evaporation. Each of these processes has been examined, and the impact of each quantified by simulating meteors with a variety of initial conditions. It has been shown that linear integration assuming negligible heat capacity of the meteoric material is insufficient to accurately describe initial ablative behavior, although it is roughly equivalent in the final stages of meteor ablation.

Sputtering, whereby the impact of an atmospheric molecule on the surface of a meteoroid ejects molecules from the lattice of meteoric material, has been examined with a focus on the importance to the production of detectable ionization. It is shown that sputtering plays a relatively minor role in the formation of the ionization detected by meteor radars.

The simulation of meteor ablation using a range of meteor sizes and initial conditions allowed a model of the detected size distribution of meteors to be assembled. A model of the size distribution of meteoroids incident on the Earth was used to weight the numerical predictions of detectability. The results of the simulations provide the new insight that meteor radar detections comprise an approximately symmetrical distribution of bodies with initial diameters in the range of 500-700 μm, depending on the sensitivity of the observing radar.

Deceleration of meteoroids causes the detected velocities of meteors to be less than the initial velocities at the starting point of atmospheric entry. The predicted initial size distribution of detected meteors was used in conjunction with simulations of meteoroid deceleration to produce a model that corrects for average deceleration and returns an estimate for the initial velocities of meteors entering the atmosphere.

The numerical simulations of meteoroid ablation and trail formation allow a further analysis of the vertical distribution of meteor detections in the atmosphere. The simulations lay the groundwork for an examination of the relationship between the properties of the atmosphere and the distribution of detected meteors.

Chapter 4

Meteor Detection Heights

The distribution of heights over which a radar detects meteors can be used as an indicator of atmospheric variation. As it has been noted in Chapter 2, radar detection of the passage of a particular meteor through the atmosphere is dependent on the radar parameters, on the physical characteristics of the meteoroid, and on the atmospheric conditions. For a stable population of meteors, such as the sporadic sources that constitute the vast majority of meteor radar detections, the overall distribution of meteor detection heights is then contingent only on the characteristics of the observing radar and the atmosphere. Given that a radar with a fixed configuration will not contribute to changes seen in the distribution of detected heights over time, the atmosphere remains the only variable quantity. In principle, it should therefore be possible to use variations in the height distribution of radar detected meteor trails as an indicator of atmospheric variability.

The heights of meteor detections over a finite period of time produce a nearly Gaussian distribution with respect to height, as can be seen in figure 4.1. This simple model of the height distribution of meteor radar detections provides two useful observable quantities: the peak height, at which meteor detection activity maximizes, and the detection zone width, which describes the range of heights over which meteors are detected.

Early meteor radar work described by Kaiser [1953] and McKinley [1961] frame

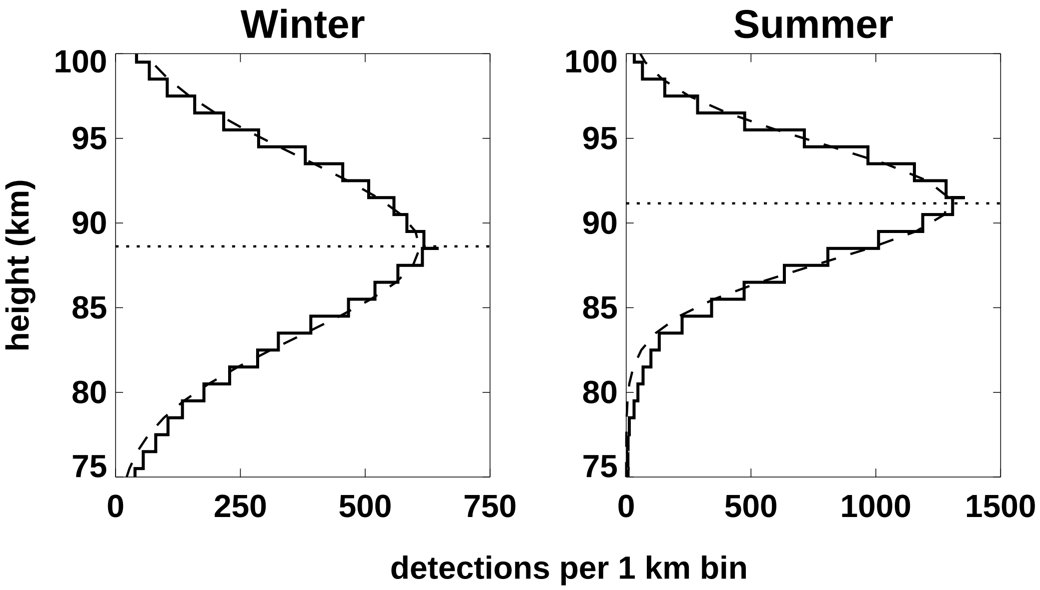

Figure 4.1: Height distribution of meteor detections from the 33 MHz meteor radar at Davis Station, Antarctica for the 2009 winter solstice (June 21, left) and summer solstice (December 22, right). The dashed line is a fitted Gaussian curve. The dotted line marks the peak detection height, as determined by the center of the fitted Gaussian curve.

the variability of the detected distribution of meteor heights as a question of radar performance. Of primary concern to initial studies was the so-called height ceiling of a radar, above which meteor detectability significantly attenuates. Further work by Steel and Elford [1991] confirmed the accuracy of the radar response function and detailed the frequency dependence of the meteor radar height distribution.

Ellyett and Kennewell [1980] examined the effect of solar variability on overall meteor detection rates, with a focus on the input meteor mass distribution. Of particular importance to this study is the recognition that the vertical component of the path length of ionization left by an ablating meteor is dependent in some way on the atmospheric density scale height [Lindbald, 1976]. Unfortunately, the focus on total detection rates does not allow an in-depth examination of the distribution of meteor detection heights, which may itself contain indications of variation in path lengths.

Clemesha and Batista [2006] look in more detail at the variation of the distribution of meteor detection heights, using the centroid or mean detection height as the key parameter. They found that there is a relation between the constant density levels in atmospheric models and the mean detection height. Furthermore, their work demonstrates that possibly solar cycle based variations in the strength of waves with periods of 2-15 days and longer can be observed by means of a spectral analysis of the variations of the mean meteor detection height.

These results show that the distribution of meteor radar detection heights should provide some indication of atmospheric variability. In order to examine this relationship further, and obtain relations that will provide useful metrics, simulated meteor radar detection height distributions were compared with the characteristics of input atmospheric models. The results of the simulations were then compared with observations to verify the predictions.

4.1 Numerical simulation

The set of simulated detections described in section 3.5 was used to assemble a predicted distribution of detections as a function of height for hypothetical meteor radars operating at 33 and 55 MHz at 68° S. The ionization curve of each meteoroid was calculated and assigned a 1 or 0 value to denote whether the electron line density exceeded q_{min}. The initial radius used in equation 2.6 was calculated using the method described by Jones [1995], which will be discussed further in section 5.2.1. Uncertainty in the measurement was added by convolving the detection zone with a Gaussian curve of width σ_h, which was obtained for each zenith angle using an error of $\pm 1°$ in the angle of arrival and ± 0.9 km for the range.

The resultant detection zone for each simulated meteor was then weighted using the relative distribution of initial conditions and added to the overall distribution. A histogram was constructed using the sum of the weighted detectability zones, separated into 1 km height bins, as is done with actual observations. A Gaussian fit was then applied to the histogram. The center of the fitted curve was used to define the peak detection height and the width of the curve was used to define the detection zone width.

Due to the dramatic seasonal variation in atmospheric density and density gradient and ample existing data, Davis Station, Antarctica at 68° S was chosen as an appropriate site for the evaluation of the impact of atmospheric variability impact on the detected meteor distributions. The simulated distribution was calculated as described above, using the NRLMSISE-00 model as a reference atmosphere, for the two hypothetical radars. The simulated distributions were calculated at five-day intervals, with the parameters of the model atmosphere averaged over each five-day period.

The results, shown in figure 4.2, followed the general trend seen in observations of a decrease in the peak detection height during winter, accompanied by an increase in the detection zone width.

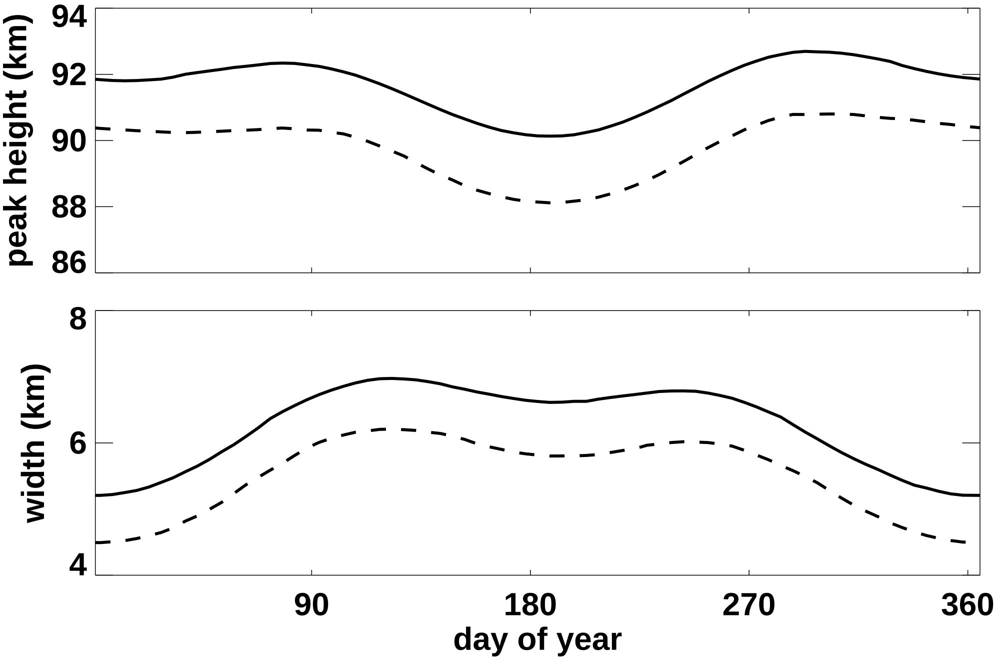

Figure 4.2: Comparison of predicted detection parameters for hypothetical 55 (dashed) and 33 (solid) MHz meteor radars, calculated using NRLMSISE-00 model data for Davis Station, Antarctica.

4.2 Effect of density scale height

The results of the simulations indicate that the width of the height distribution of detected meteors is a nearly linear function of the density scale height, which can be seen in figure 4.3. With this relationship, it is possible to use a simple data parameter obtained during meteor radar operation to infer the atmospheric density gradient.

Implementation of such a method to recover density scale heights from meteor height distributions would first involve calibrating a radar's detection zone widths against a set of known values for the scale height, in order to take into account the sensitivity of the specific radar. A linear fit could then be applied as in figure 4.3 to produce a simple linear conversion between observed detection zone width and density scale height.

The error for this method was estimated from the simulation values by calculating the mean absolute deviation between the scale height estimate inferred from a linear fit and the supplied model value. It was found that the linear fit was accurate to within about 100 m of the supplied model scale height value.

4.2.1 Linearity of H^* vs $h_1 - h_2$

Further analysis of the simulation results showed that this relationship is not restricted to the cumulative height distributions for ensembles of meteors. Single meteors also exhibit a correlation between the vertical component of the detectable ionized path length and atmospheric density scale height. For an individual meteoroid with fixed initial conditions, the range of heights at which it is actively evaporating can be shown to be an almost linear function of scale height.

This result can be derived from a strictly theoretical consideration of the processes involved in the evaporation of a meteoroid. Figure 3.2 shows that, at evaporative temperatures, the power consumed by heating is negligible in comparison to that consumed by vaporization. Similarly, as seen in figure 3.1, the power consumed by radiation is also small in comparison to that consumed by vaporization. Applying

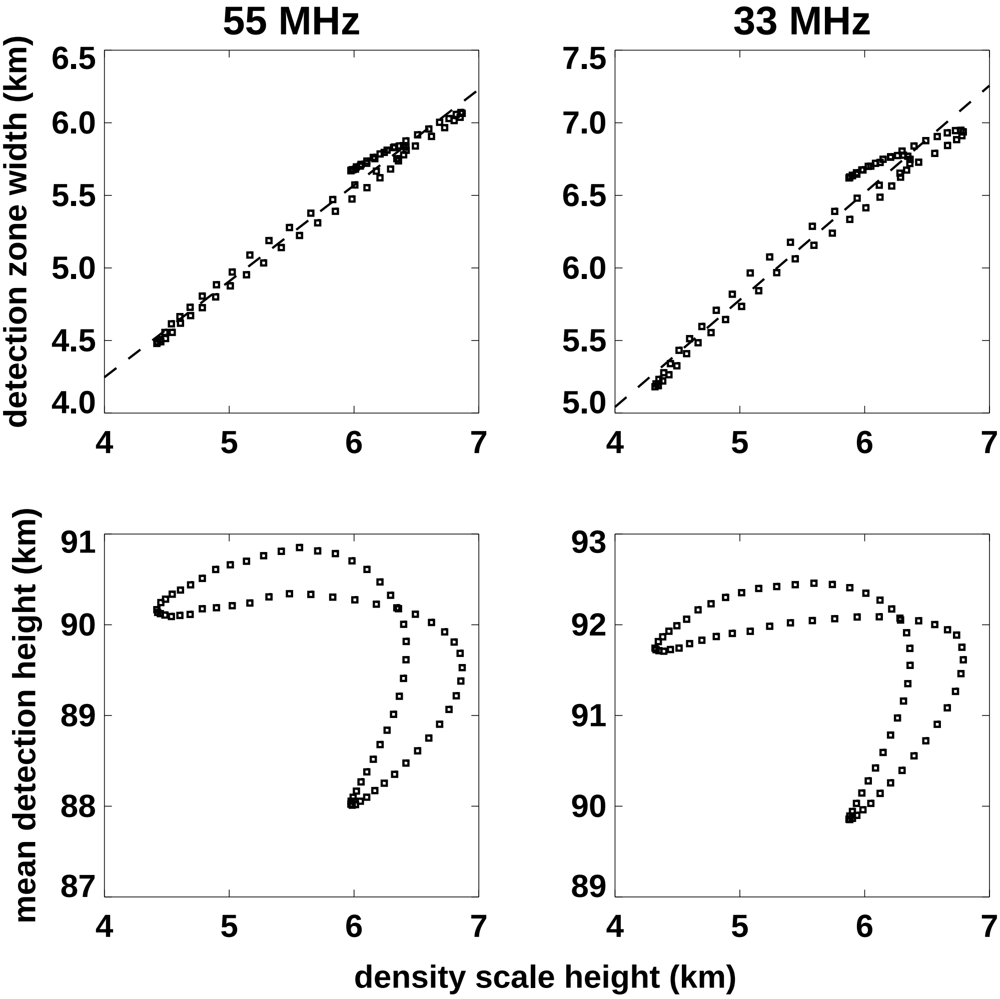

Figure 4.3: Results of simulation showing the relation between density scale height and meteor detection zone width (top row) and peak detection height (bottom row) for 33 and 55 MHz radars (left and right column, respectively) using model data for Davis Station, Antarctica, located at 68° S. The dashed line is the line of best fit.

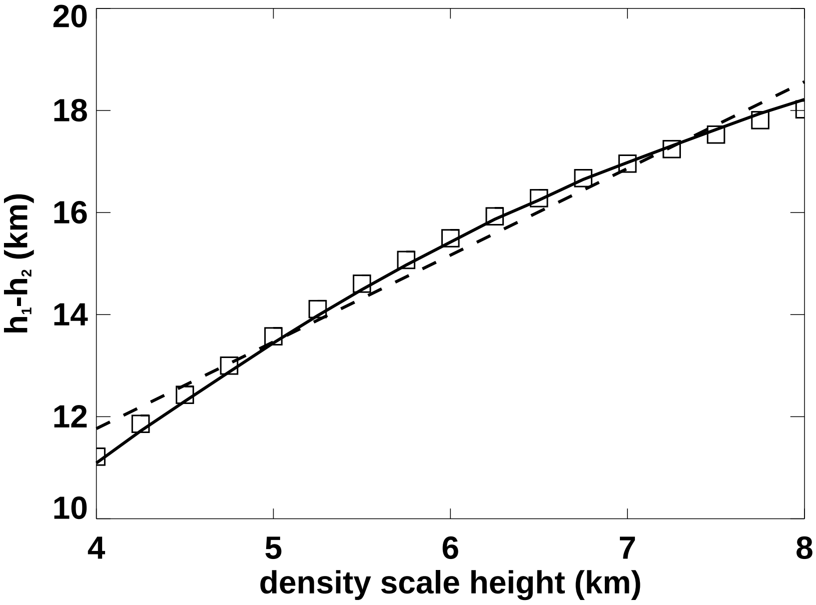

Figure 4.4: Dependence of the vertical width of detectable ionization on density scale height. The solid line is $H^* \ln(A/H^*+1)$. Boxes are $h_1 - h_2$ obtained from a simulated meteor with 600 μm initial diameter, 45 degree angle of entry, and 30 km s^{-1} entry velocity. The dashed line is the line of best fit.

these conditions reduces equation 3.24 to

$$\frac{\Lambda}{2}\rho_a v^3 \pi r^2 = 4\pi r^2 h_v C_L p_v \sqrt{\frac{m_{mol}}{T}}, \tag{4.1}$$

which holds for the evaporative phase of meteoroid evolution.

The relationship can be further simplified by dividing both sides of equation 4.1 by the surface area of the particle at any given time, producing a description of the balance of power per unit surface area:

$$\frac{\Lambda}{8}\rho_a v^3 = h_v C_L p_v \sqrt{\frac{m_{mol}}{T}}, \tag{4.2}$$

When the energy budget of a particle is dominated by evaporation, the integral of equation 4.2 with respect to time is conserved for a particle of a given size. The energy required to evaporate material from a spherical surface to a depth of dr is $4\pi r^2 h_v \rho_m dr$. The integral of this with respect to particle radius is then the product of volume, latent heat of vaporization, and density which is simply the energy required to vaporize the entire particle. If the energy per unit surface area is integrated over the instantaneous radius of the evaporating particle, the result is another conserved quantity, the total energy consumed per unit surface area, given by

$$E_s = \int_0^{r_0} h_v \rho_m dr = h_v \rho_m r_0, \tag{4.3}$$

where r_0 is the particle's initial radius. This term is constant for any particle with initial radius r_0. It is the energy required to vaporize a slab of material with unit surface area to a depth of r_0.

Consider a meteoroid that rapidly commences evaporation at some height h_1, atmospheric density ρ_1, and time t_1 and is completely evaporated at height h_2, atmospheric density ρ_2, and time t_2. Combining equations 4.2 and 4.3 the energy consumed per unit surface area by evaporation can be expressed as

$$E_s = \int_{t_1}^{t_2} h_v C_L p_v(t) \sqrt{\frac{m_{mol}}{T(t)}} dt = \int_{t_1}^{t_2} \frac{\Lambda}{8}\rho_a(t) v^3 dt. \tag{4.4}$$

Assuming that the atmospheric density varies exponentially with height, that deceleration is small (see figure 3.5), and defining the average velocity $\bar{v}$, the right hand

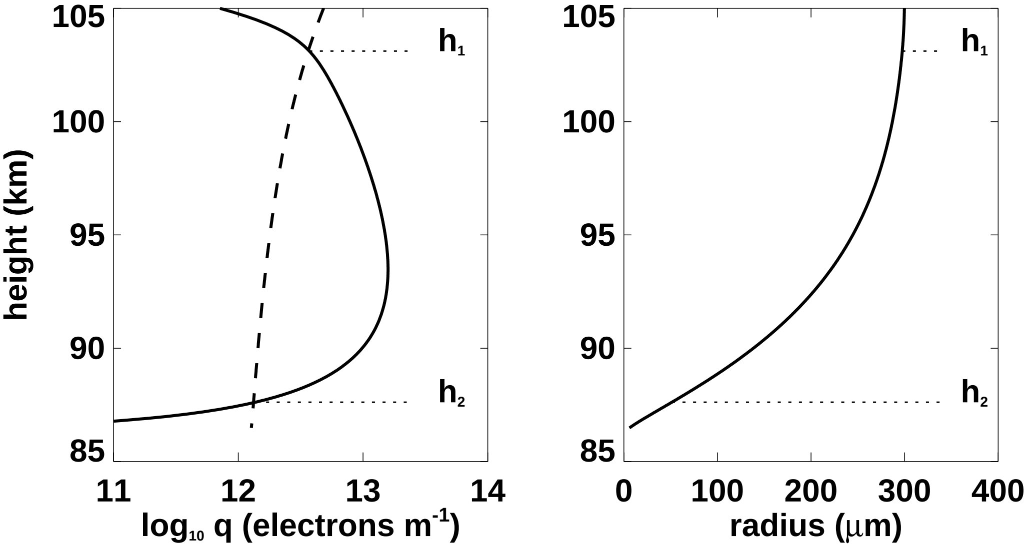

Figure 4.5: Left: Electron line density produced by a 600 μm, 45° angle of entry, 30 km s^{-1} particle. The start of detectable evaporation (h_1) and end of detectable evaporation (h_2) are annotated where the minimum detectable electron line density (dashed) crosses the trail's electron line density (solid). Right: Evolution of the radius of the same particle during the evaporative phase.

side of equation 4.4 can be expressed as

$$E_s = \frac{\Lambda \bar{v}^3}{8} \int_{t_1}^{t_2} \rho_a(t_1) \exp\left[-\frac{\bar{v}\sin\theta\,(t-t_1)}{H^*}\right] dt = \frac{H^* \Lambda \bar{v}^2 \rho_a(h_1)}{8\sin\theta}\left[\exp\left(-\frac{h_2-h_1}{H^*}\right)-1\right]. \tag{4.5}$$

Solving for $h_1 - h_2$, the range of heights over which the particle is actively evaporating, and thus depositing material that may be ionized, yields

$$h_1 - h_2 = H^* \ln\left(\frac{A}{H^*}+1\right), \tag{4.6}$$

where $A = 8E_s \sin\theta / \Lambda \bar{v}^2 \rho_a(h_1)$.

It can be seen in figure 4.4 that equation 4.6 is nearly linear in H^*. The result of this relationship is that the range of heights over which any meteoroid is evaporating can be considered to be approximately proportional to H^*. Therefore, the cumulative height range over which an ensemble of meteoroids is detectable by a radar is also proportional to H^*.

It should be noted that for particles with initial diameters below about 400 μm the value of $h_1 - h_2$ becomes smaller than the theoretical prediction for larger values of the density scale height. This is due to small particles ablating above the detection ceiling of the radar where the increase in the initial radius produces a value of q_{min} in excess of the overdense cutoff, leading to a decrease in detectable path length. In this case, the detectable portion of ionization is truncated by the intersection of q_{min} with the overdense cutoff at high altitudes.

For particles with an initial diameter in excess of about 800 μm, heat capacity is an increasingly important term, which leads to a slightly larger value of $h_1 - h_2$, due to the additional 'thermal inertia' [Love and Brownlee, 1991] that must be overcome. Fortunately, both of these effects occur in the extremities of the detectable size distributions shown in figure 3.4. Additionally, the reasonably symmetric distribution of detected particle sizes means that outliers in either size direction, which have opposite deviations from equation 4.6, will mostly cancel one another in the complete ensemble that determines the meteor detection height distribution.

The simulations performed considered only the ablation of single bodies. Fragmentation is a well documented phenomenon in radio meteor observations (see e.g., Elford and Campbell [2001]) and it remains to be seen what the effect of the separation of a body into multiple parts will have on the effective trail length. Verniani [1973] suggests that fragmenting meteors will produce shorter trails, but if a fragmented meteor trail is considered to be the superposition of the constituent smaller trails, then the reduced trail lengths should still scale linearly with the density scale height.

The derived relationship shown in figure 4.3 provides a means for the estimation of the atmosphere's density scale height in the meteor ablation region. However, in order to apply this method it is necessary to take into account radar sensitivity. Due to the minimum detectable electron line density described by equation 2.13 and illustrated in figure 4.5, a radar will not necessarily detect the ablation of a meteoroid over the entire range $h_1 - h_2$, but rather may detect a truncated section of the ionization curve. Additionally, radars with different sensitivities will detect ensembles of meteors with different distributions of initial conditions, as seen in figure 3.4. Thus, it is necessary to calibrate the observed values of Δh against a known source of H^*, whether that be from independent observations of density or an accepted model. Once this is complete, meteor detection height distributions become a valuable tool in characterizing the upper atmosphere.

4.3 Effect of constant density level

While the density scale height characterizes the rate at which atmospheric density decreases with respect to height, the height at which a given density occurs is also a useful metric of atmospheric behavior. The movement of a constant density level signifies an integrated shift throughout the entire atmospheric column below it, which may or may not be related to the source of variation in the density scale height in the meteor ablation region.

A constant density level corresponding to the height at which the atmosphere has a density of 3×10^{-6} kg m^{-3} was selected here as the level of interest. This value was chosen because it is the approximate average model value around the peak detection height in simulations. The height of the constant density level was determined by performing a linear interpolation of the logarithm of density with respect to height within the detection zone.

A comparison of the height of the constant density level with peak detection height and detection zone width, shown in figure 4.6, shows no clear correlation between detection zone width and the constant density level. The peak height, however, approximately follows the variation in the height of the constant density level.

As the density profile of the entire atmospheric column in the ablation zone is shifted vertically, the ablation region will also be displaced vertically. Hence, the vertical positions of detectable meteors will vary with changes to the height of constant atmospheric density levels. The spread in values seen in figure 4.6 is due to the additional independent variables affecting the peak detection height. Detectability of meteors as described in Chapter 2 is also dependent on the range from the radar to the meteor trail and the initial radius of the trail, which is in turn dependent on the local temperature and pressure. These terms modify the otherwise simple dependence of the peak detection height on the height of a specific density contour, resulting in increased scatter in the comparison of the two values.

While not precise enough to track the exact height of a specific density level, this result does suggest that a significant variation in the peak height of meteor detections is an indication of vertical movement of constant density contours in the atmosphere. A similar linear regression approach to that described in section 4.2 can be used to recover an approximate value of the constant density level, allowing for an initial calibration using a range of values.

The uncertainty in this method was estimated using the mean absolute deviation between the linear fit estimate of the height of the constant density level and the input model value of the height of the constant density level. It was found that, based on the simulated peak height values, this method provides an estimate of the actual height

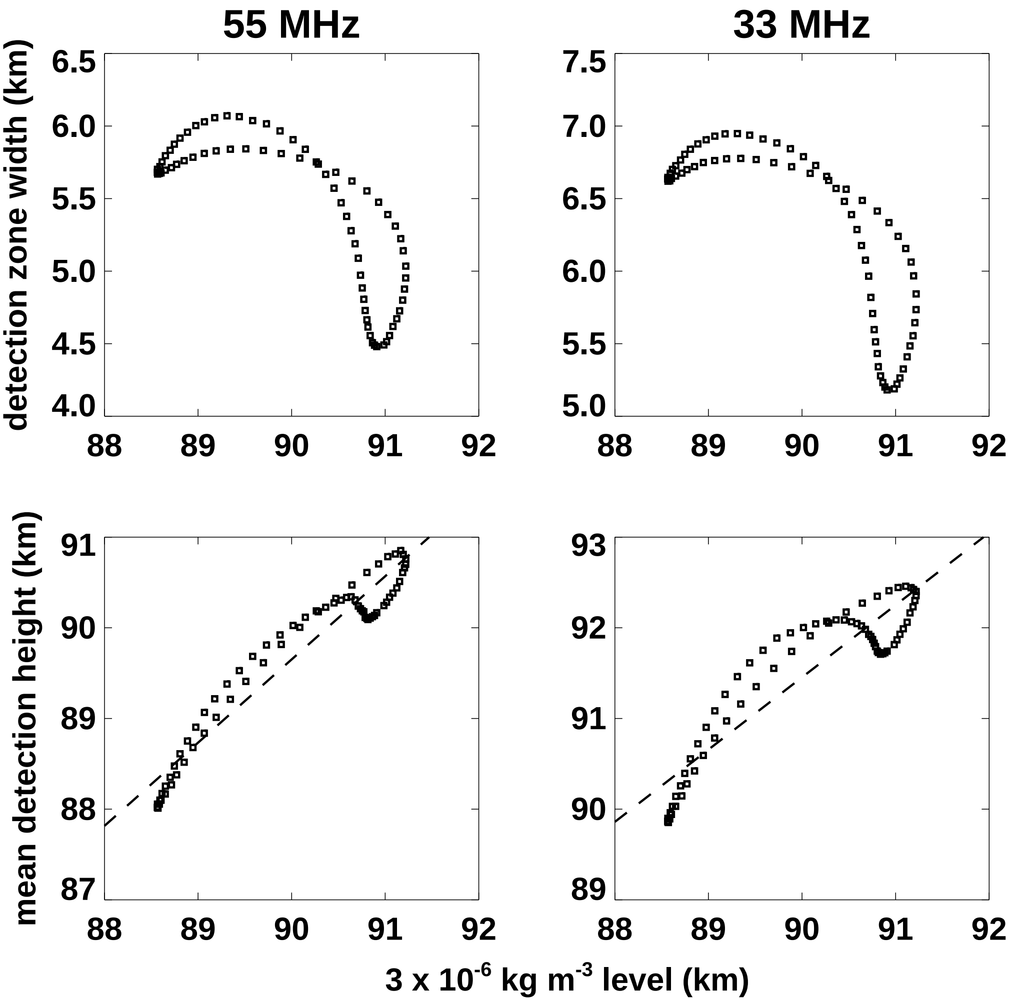

Figure 4.6: Results of simulation showing the relation between the height at which the atmospheric density is 3×10^{-6} kg m^{-3} and meteor detection zone width (top row) and mean detection height (bottom row) for 33 and 55 MHz radars (left and right column, respectively) using model data for Davis Station, Antarctica, located at 68° S. Dashed line is the line of best fit.

of the 3×10^{-6} kg m^{-3} density level accurate to within about ±220 m for the 55 MHz radar and about ±325 m for the 33 MHz radar.

4.4 Observations

The predictions of the numerical simulations were compared with the data for one year collected by the 33 MHz meteor radar located at Davis Station, Antarctica during 2009. The daily number of detections ranged from about 5,000 in winter to over 15,000 in summer. The detection zone parameters were obtained by fitting a Gaussian curve to a 1 km bin height histogram of detections for each day, as was done for the simulated distributions described in section 4.1.

It was found that the detection zone width demonstrated a nearly linear relation to the model density scale height in the detection zone, as seen in figure 4.7, which is consistent with the results of the simulations. Significantly more scatter was seen in the observations than in the simulations, but it is likely that a large contributor to the uncertainty is short time scale geophysical variations not present in the model values.

A comparison of the observed daily peak heights with the model 3×10^{-6} kg m^{-3} density level height is shown in figure 4.8. As was the case with the relationship between the density scale height and the detection zone width, the observations showed a correlation between the constant density level's height and the peak height of meteor detections. The observations are consistent with the findings of Clemesha and Batista [2006], who observed a correlation between mean detection height and constant density level height. Again, there is more scatter in the observations, which is due in part to small time scale atmospheric variations in the form of atmospheric tides and 2-15 day planetary wave spectral features. An additional source of scatter is that the model constant density level minimum height seems to lag the observed minimum peak height by about 20 days. Given the otherwise close correlation, this may be due to a weather effect for the particular year.

These results support the proposition that atmospheric variability has a tangible

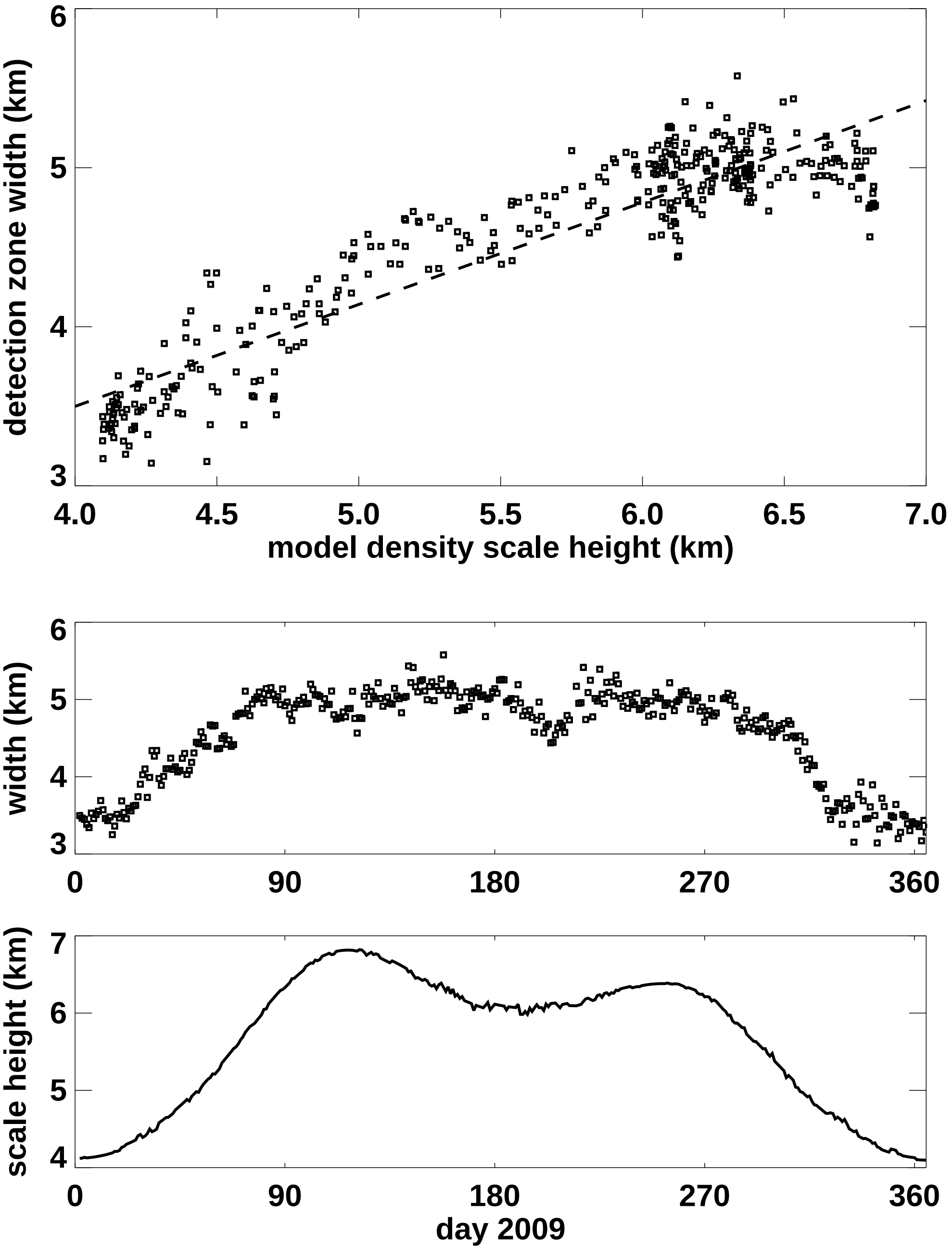

Figure 4.7: Top: Comparison of the daily meteor detection height distribution widths for 2009 from the Davis Station, Antarctica 33 MHz meteor radar with NRLMSISE-00 model scale height around the peak detection height. Best fit line (dashed) shown for comparison. Center: Daily detection zone width. Bottom: Daily average model density scale height in the detection zone.

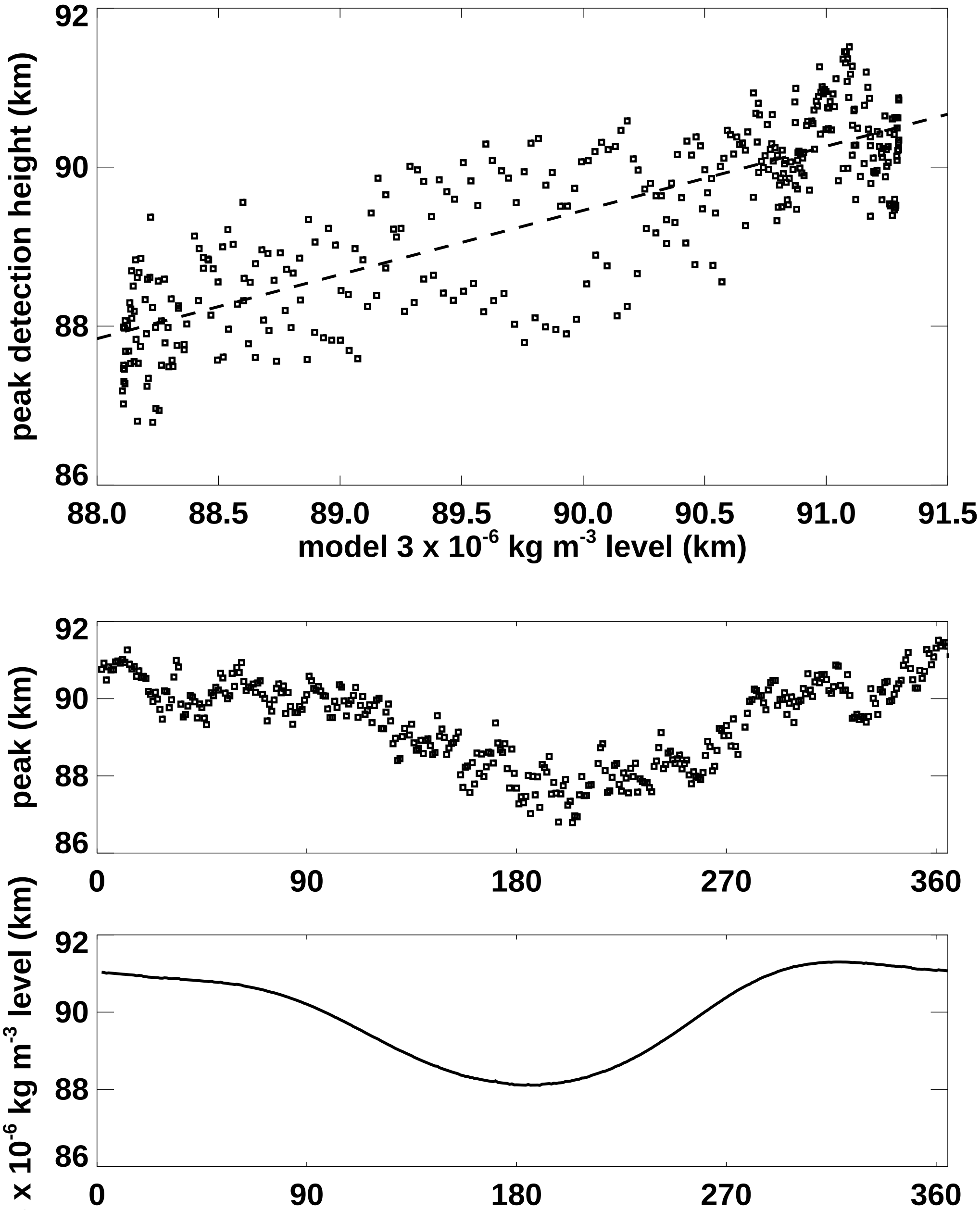

Figure 4.8: Top: Comparison of the daily mean meteor detection heights for 2009 from the Davis Station, Antarctica 33 MHz meteor radar with NRLMSISE-00 model 3×10^{-6} kg m^{-3} density level height. Best fit line (dashed) shown for comparison. Center: Daily peak detection heights. Bottom: Daily average model height of the 3×10^{-6} kg m^{-3} density level.

effect on the height distribution of meteor radar detections. The variability in the height distribution's parameters can then be used as a source of information on the density conditions in the upper atmosphere.

4.5 Summary

Variations in the density and density gradient of the upper atmosphere produce detectable changes to the height distribution of meteor radar detections. Numerical simulations of the ablation process have been performed and detection criteria applied for meteors with a range of initial conditions, based on existing models and observations of the characteristics of the incident meteor flux. Simulations predict that the peak height of meteor detections is an approximately linear function of the height of constant density contours in the meteor ablation region, and that the width of the height distribution of meteor detections is an approximately linear function of the atmospheric density scale height in the meteor ablation region.

Through a purely theoretical consideration, it has been shown that the vertical component of the path length of detectable ionization for a single meteor is a nearly linear function of the atmospheric density scale height. This result depends on the conservation of the total energy consumed per unit surface area during the ablation of a meteoroid. This follows from the desciption of the evaporative energy budget in Chapter 3 which shows that this condition is satisfied for meteoroids in the range of detectable sizes shown in figure 3.4 during the evaporative phase of meteoroid evolution.

Meteor detections collected at Davis Station, Antarctica, were compared with a reference model atmosphere. The results of this comparison are consistent with the predictions of the numerical simulation. The observations clearly demonstrate a correlation between the peak detection height and the height of constant atmospheric density contours in the ablation region, and between the width of the height distribution of meteor detections and the atmospheric density scale height in the ablation region.

By explaining the mechanisms primarily responsible for the peak detection height and width of the height distribution of detections, two new metrics for the observation of the atmospheric density profile in the upper atmosphere have been established. Such a method does, however, require that the peak heights and detection zone widths be initially calibrated against an accepted set of values of a constant density level height and the atmospheric density scale height. Once this is done, variations in atmospheric density and density scale height can be inferred from a simple assessment of the distribution of meteor detections. Due to the simplicity of the two measurements involved, this allows older data sets for which detailed individual detection data are not available to yield useful information about the density conditions of the upper atmosphere.

Following from the examination of the broad behavior of sets of meteor detections, a more detailed description of the properties of individual detections will be examined. Each detection of an underdense meteor trail by radar includes a record of the evolution of the intensity of received backscatter with respect to time. The properties of each echo will provide additional information about the meteor trail and the atmosphere in which it is formed.

Chapter 5

Properties of Underdense Meteor Echoes

A major reason for the interest in underdense meteor echoes, specifically, is that they decay over time at a rate determined by the ambipolar diffusion coefficient, which is governed by the temperature and pressure of the local atmosphere. Interpretation of diffusion coefficient estimates requires an understanding of the processes that contribute to the observed behavior of the intensity of observed meteor trail backscatter over time.

The underdense echo is a diffraction pattern formed by the particular geometry of the meteor trail and the observing radar. The intensity of the echo is modified by the evolution of the trail over time, the intrinsic properties of the particular trail, and the speed at which the meteor travels across the field-of-view of the radar. Understanding the formation of the echo enables the inference of the properties of meteor trails and the atmosphere from observations of the characteristics of individual echoes.

In this chapter, the mathematical description of the formation and decay of the Fresnel diffraction pattern of an underdense meteor trail will be reviewed. The effect of different meteor trail properties on the observed echo decay time will be demonstrated in order to assess how different meteor trail characteristics affect echo decay time. This provides a quantitative rationale for the removal of these effects from consideration when attempting to discern the cause of anomalous underdense echo decay phenomena in Chapter 6.

5.1 Fresnel Diffraction Pattern

As a meteoroid travels across the field-of-view of a radar, depositing ionized material in its wake, the observed backscatter produces a knife-edge type diffraction pattern at the observing site. The meteoroid itself represents the edge, with the coherent backscatter emanating from the trail representing the illuminated one-sided aperture. The interference between backscatter originating in different parts of the trail produces a distinctive diffraction pattern that can be observed as the meteoroid travels across the specular point along the trail axis. This point is defined as the position where the line-of-sight to the radar is perpendicular to the path of the meteor.

A description of the resultant backscatter from an underdense trail begins with the consideration of a hypothetical trail wherein all ionization is concentrated along the trail axis. Lovell and Clegg [1948] describe the development of the observed backscattered intensity over time. The power incident on a trail at range R from a transmitter with power P_T and antenna gain G_T is $P_T G_T / 4\pi R^2$. The scattering cross section of a single electron in the trail is $4\pi \mathrm{e}^4/m_e^2 c^4 = 4\pi r_e^2$, where c is the speed of light and m_e is the mass of an electron. Thus, the backscattered power from a single electron observed at the receiver is given by

$$\Delta P_R = \frac{P_T G_T G_R \lambda^2 r_e^2}{16\pi R^4}. \tag{5.1}$$

The backscattered radiation from different segments along the trail axis interferes, which means that the backscattered amplitude must be integrated along the length of the trail in order for the total observed power to be determined. Following McKinley [1961], the instantaneous amplitude observed at the receiver at time t from a segment of trail with length ds and electron line density q is given by

$$\Delta A_R = (2 Z_R \Delta P_R)^{1/2} q \sin\left(2\pi f t - \frac{4\pi R}{\lambda}\right) ds, \tag{5.2}$$

where Z_R is the input impedance of the receiver and f is the frequency of the radar. Integrating over the length of the trail with the meteoroid at a distance s along the trail axis from the specular point, the instantaneous amplitude observed by the receiver for the entire trail is

$$A_R = (2Z_R \Delta P_R)^{1/2} q \int_{-\infty}^{s} \sin\left(2\pi f t - \frac{4\pi R}{\lambda}\right) ds. \tag{5.3}$$

The integral in equation 5.3 can then be simplified using the approximation $R \approx R_0 + s^2/2R_0$ where R_0 is the distance from the radar to the specular point. Using the transformations $\Phi = 2\pi f t - 4\pi R_0/\lambda$ and $x = 2s/(r_0\lambda)^{1/2}$, equation 5.3 becomes

$$A_R = \frac{(2Z_R \Delta P_R)^{1/2} q}{2} \int_{-\infty}^{x} \sin\left(\Phi - \frac{\pi x^2}{2}\right) dx = \frac{(2Z_R \Delta P_R)^{1/2} q}{2} (C \sin\Phi - S \cos\Phi). \tag{5.4}$$

The Fresnel integrals C and S are defined as

$$C = \int_{-\infty}^{x} \cos\frac{\pi x^2}{2} dx \qquad S = \int_{-\infty}^{x} \sin\frac{\pi x^2}{2} dx. \tag{5.5}$$

The transformed meteor trail path length x expresses the distance the meteoroid has traveled along the trail axis, as measured in units of the Fresnel zone of the wavelength and range, relative to the specular point.

The frequency of the oscillations of the Fresnel integrals is much smaller than f, so the Φ dependence may be removed by averaging equation 5.4 over a period of time that is large in comparison with one period of the radio frequency, but small in comparison with the period of a Fresnel oscillation. The instantaneous power observed by the receiver is then

$$P_R = \frac{A_R^2}{2Z_R} = \frac{\Delta P_R R_0 \lambda q^2}{2} \left(\frac{C^2 + S^2}{2}\right). \tag{5.6}$$

Combining equations 5.1 and 5.6,

$$P_R = 2.5 \times 10^{-32} P_T G_T G_R q^2 \left(\frac{\lambda}{R_0}\right)^3 \left(\frac{C^2 + S^2}{2}\right), \tag{5.7}$$

which is the unattenuated received power given by equation 2.5, modulated by the sum of the squares of the Fresnel integrals.

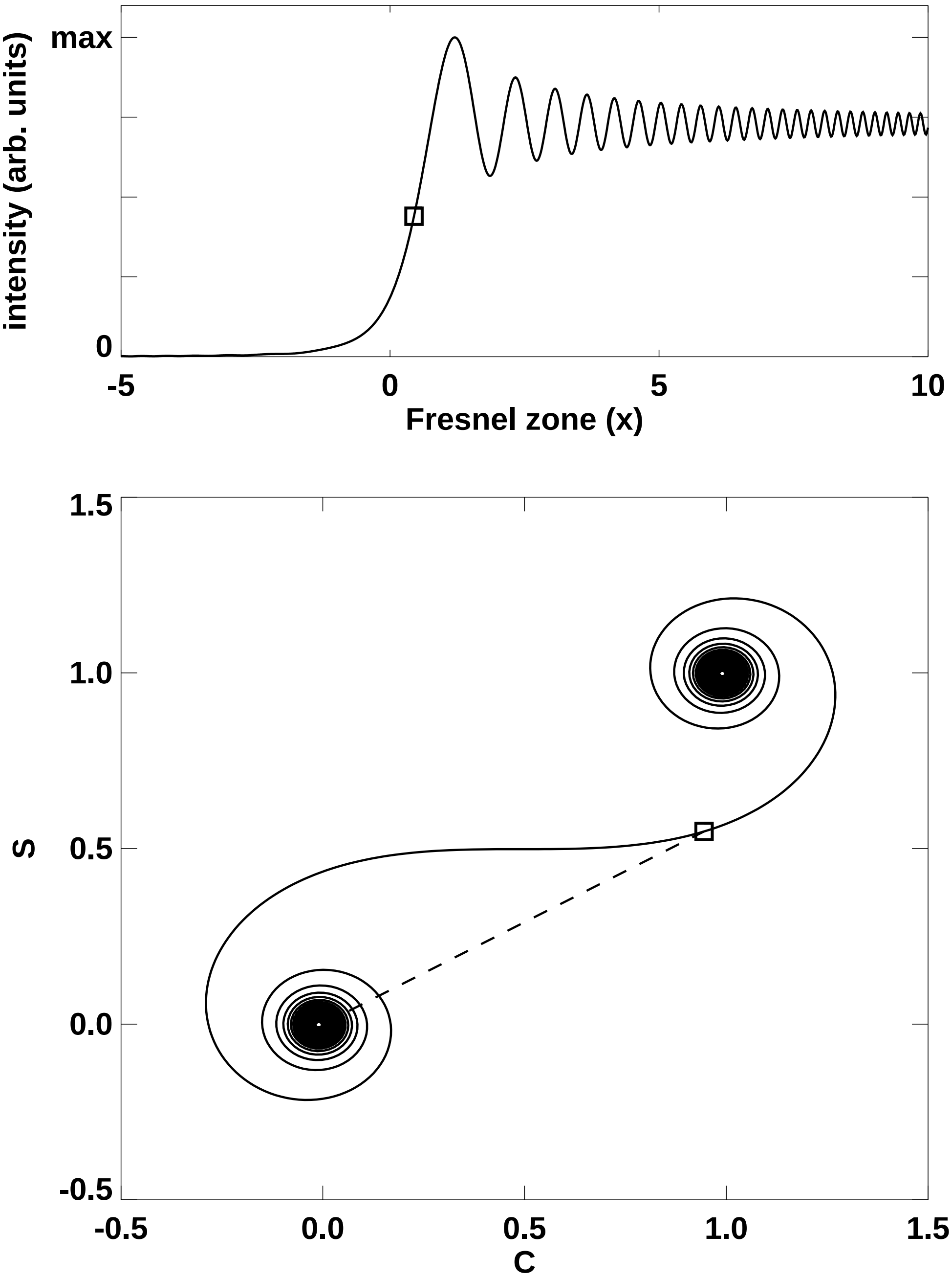

Figure 5.1: Top: Observed intensity of the meteor echo diffraction pattern as a function of the path length traveled, measured in units of Fresnel zone length. Units of intensity are arbitrary, depending on the electron density of the meteor trail and the sensitivity of the observing radar. Bottom: Associated Cornu spiral. The dashed line is the vector whose length defines the echo intensity at a point of interest, denoted by a box in both panels.

It is the modulation produced by the factor of $C^2 + S^2$ that produces the distinctive diffraction pattern seen in the top panel of figure 5.1. The intensity of observed backscatter increases rapidly beginning around $x = -1$ to a maximum at about $x = 1.217$. The maximum gradient occurs at $x = 0.572$ [Baggaley et al., 1997]. Following the initial peak, the intensity settles into a series of oscillations with increasing frequency and decreasing amplitude.

A useful method of interpreting the behavior of the diffraction pattern is the Cornu spiral (see, e.g., McKinley [1961]), seen at the bottom of figure 5.3. The Cornu spiral plots C against S. The intensity of the diffraction pattern can then be obtained from the square of the length of the vector extending from the origin to a point along the curve. The path length, x, is measured along the length of the curve, from the bottom left to upper right. The specular point is at the midpoint between the two spiral features.

Initially, the intensity of the diffraction pattern is small, as the intensity vector winds out of the lower left spiral. A transition occurs when the value of x approaches the specular point at $x = 0$. The intensity is suddenly increased as the movable end of the intensity vector crosses to the opposite spiral. This represents the sudden amplitude spike as the trail is formed around the specular point. The intensity then settles into a series of oscillations with decreasing amplitude and increasing frequency as the end point of the vector winds towards the center of the upper right spiral.

5.2 Trail Evolution

So far, the trail has been treated as a line of ionization concentrated on the trail axis. This idealization ignores the radial structure of the trail, and the evolution of the trail over time. How the trail is formed around the axis and how diffusion changes the backscatter observed from the volume of the trail over time will now be discussed.

5.2.1 Initial radius

As a meteoroid evaporates, material is ejected from the surface of the body, which in turn collides with atmospheric molecules. The initial collision between meteoric atoms and atmospheric molecules takes place at the relative velocity of the meteoroid. After a number of collisions, the atoms and ions shed by the meteoroid are slowed to the thermal velocity of the surrounding atmosphere. At this point, the meteoric material has spread around the axis, in a distribution determined by the paths of collisions with atmospheric molecules. Assumed to be Gaussian to a first approximation [Kaiser, 1953], the radial width of this distribution is referred to as the initial radius of the trail, r_0. The time taken for the distribution of meteoric material to reach r_0 is the formation time, t_0. Following the formation of the trail, ordinary diffusion governs the motion of the evaporated atoms and ions, which is described in section 5.2.2.

The initial radius was considered as a problem of colliding elastic spheres by Massey and Sida [1955] and Manning [1958]. They differed on the appropriate scattering cross section of the meteoric ions, but were in agreement on the general form of r_0. It was proposed that the initial radius of a meteor trail is proportional to the mean free path of atmospheric molecules, or $r_0 \propto \rho_a^{-1}$.

The effective diffusion cross section, σ_d of an ion in a neutral gas is crucial to the determination of the initial radius of a meteor trail and the diffusive behavior of the ions over time. Manning [1958] shows that the initial radius is proportional to the mean free path, l, of the ion with effective diffusion cross section σ_d traveling through the neutral gas with number density n_a, as given by

$$l = \frac{1}{n_a \sigma_d}. \tag{5.8}$$

Portnyagin [1966] followed Massey and Sida [1955] to produce the simplified expression

$$\sigma_d = \frac{C}{v}, \tag{5.9}$$

where $C \approx 1.7 \times 10^{-11}$ m^3 s^{-1} for a typical meteoroid composition.

Portnyagin and Tokhtasyev [1974] provide a more detailed examination of the origin of σ_d and derived an expression for σ_d by considering the probabilistic scattering behavior between ions and neutral gas molecules. For ions with initial velocity v and molar mass M_i in a background of neutral atmospheric molecules with molar mass M_a, they proposed that

$$\sigma_d = \frac{2.20 \times 10^{-5}}{v} \left(\frac{\bar{\alpha}}{N_A \mu} \right)^{1/2}, \tag{5.10}$$

where N_A is Avogadro's number and $\mu = M_i M_a / (M_i + M_a)$ is the reduced mass of the colliding ion and neutral molecule. The average polarizability of the atmospheric molecules, $\bar{\alpha}$, is taken to be 10.8 for O_2 and 11.9 for N_2 in units of the Bohr radius cubed [*].

Bronshten [1983] elaborates on the velocity and atmospheric density dependence of the initial radius. He modifies equation 5.9 to become

$$\sigma_d = \frac{C'}{v^{-0.8}}, \tag{5.11}$$

where $C' = 1.4 \times 10^{-15}$[†] for what is described as typical meteor composition, although the precise nature of this composition is not specified. This leads him to suggest an expression of the form $r_0 \propto \rho^a v^b$ where $a \approx -1$ and $b \approx 0.8$. It should be noted that Bronshten attributes the velocity dependence of $v^{-0.8}$ to Portnyagin and Tokhtasyev [1974], but this modification is not mentioned in that source. The origin of the -0.8 velocity exponent is therefore unclear, although it is in agreement with observations (see, e.g., Ceplecha et al. [1998]).

Jones [1995] revisited the modeling of the initial scattering of meteoric ions, investigating the time taken for ions to reach local thermal velocities and their distribution around the axis at that time. He modeled the formation of the trail by numerically simulating the paths of 10,000 meteoric molecules as they were decelerated and scattered by collisions with atmospheric molecules. The initial radius was then defined as the r.m.s. distance of ions from the trail axis after 10 collisions.

He found that ions were slowed to thermal velocities within about ten collisions with atmospheric molecules, which takes about 3.8×10^{-4} s for ions with an initial

---

[*] Equation 5.10 has been modified from the original text to accept SI units, with the exception of polarizability.

[†] The provided constant has been translated from the c.g.s. units of the original text to SI units.

velocity of 40 km s^{-1} at a height of 95 km. This formation time is small compared to the time scales of both the passage of the meteoroid across the central Fresnel zones and the diffusion of ions away from the trail axis. This means that the time taken for ions to be distributed around the trail axis and assume normal diffusion does not significantly affect observations of the time-dependence of backscatter intensity from the trail. Hence, the approximation that the trail is instantly formed following the passage of the meteoroid remains valid when considering echo decay.

It was found, however, that the initial distribution of ions around the trail axis deviates significantly from the assumption of a Gaussian distribution. The simulations of Jones [1995] predict that the initial distribution of ions has a core with a width of about $0.4r_0$, constituting approximately one tenth of the overall electron line density, embedded in a more diffuse distribution at the edges. This lead Jones to define an "effective" r_0, which is the width of a Gaussian distribution with the same radio wave scattering intensity as the simulated distribution. Such a distribution has a width of $r_0 = 2.845 \times 10^{18} v^{0.8}/n_a$. This was the value used for the numerical simulation of meteor ablation and detection described in Chapter 3.

Radar observations of the initial radius of meteor trails (see e.g., Baggaley [1970]) have produced a more complex picture of the initial radius problem. Campbell-Brown and Jones [2003] suggest that fragmentation may be responsible for an increase in the lateral extent of some meteor trails. A comparison with observations (see e.g., Ceplecha et al. [1998]) does however show that the equation given above is an acceptable first approximation.

5.2.2 Diffusion

Once the trail is formed, the ions in the trail diffuse outward at a rate determined by the local atmospheric conditions. The radial expansion of the trail produces interference between different areas of the scattering volume, leading to a net decline in the observed backscatter intensity as the trail expands. This allows the decay of observed backscatter intensity to be used to estimate the diffusive properties of the atmosphere.

Diffusion of the ions and electrons of the meteor trail is assumed to be quasi-neutral, given that the scale of the trail's physical dimensions are much greater than Debye length of the ions and electrons [Hill, 1978]. Any separation between fast moving electrons and the slowly diffusing, heavier ions results in an electric field that accelerates the ions and retards the motion of the electrons. Given that the ions are much heavier than the electrons, the Coulomb force effectively restrains the motions of the electrons so that their diffusion is bound to that of the ions in the trail.

The rate of diffusion of ionized materials away from the axis of a meteor trail is characterized by the ambipolar diffusion coefficient. The Einstein relation (see, e.g., Cervera and Reid [2000]) defines the diffusion coefficient for ions in a neutral gas as

$$D_i = \frac{kT_iK}{e}, \tag{5.12}$$

where K is the zero field mobility factor, given for atmospheric temperature T and pressure p by

$$K = \frac{1.013 \times 10^5}{p} \frac{T}{273.16} K_0. \tag{5.13}$$

Massey et al. [1971] provides a formula to calculate K_0 for specific ion-atmospheric molecule combinations given by

$$K_0 = 1.14 \times 10^{-4} \left(\bar{\alpha}\mu\right)^{-1/2}. \tag{5.14}$$

This relationship between ion mass and K_0 is illustrated in figure 5.2, which shows decreasing ionic mobility with increasing ion mass. Therefore, heavier ions will diffuse more slowly than light ions.

The ambipolar diffusion coefficient D is related to the ionic diffusion coefficient D_i by

$$D = D_i \left(1 + \frac{T_e}{T_i}\right), \tag{5.15}$$

where T_e and T_i are the electron and ion temperatures, respectively [Kaiser, 1953]. Assuming that the electron and ions are in thermal equilibrium, the ambipolar diffusion coefficient is then given by $D = 2D_i$. Combining this result with equations 5.12, 5.13,

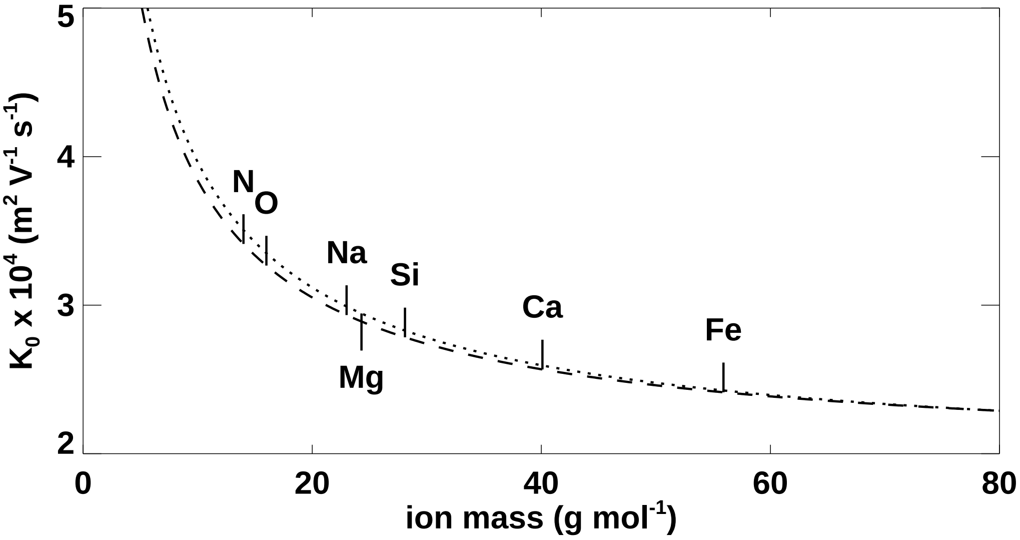

Figure 5.2: Reduced mobility of meteor trail ions in N_2 (dashed line) and O_2 (dotted) line. Common ions present in meteor trail spectra [Ceplecha et al., 1998] are indicated.

and 5.14 the diffusion coefficient as a function of atmospheric properties is given by

$$D = 6.39 \times 10^{-2} \frac{T^2}{p} K_0 = 2.23 \times 10^{-4} \frac{T}{\rho_a} K_0. \tag{5.16}$$

The diffusion coefficient described above governs the rate at which the concentration of ionized material changes over time. For a meteor trail, the distribution of ionized material is assumed to be cylindrically symmetric at any point along the trail. The diffusion equation for a distribution with cylindrical symmetry is given by

$$\frac{\partial n(r,t)}{\partial t} = -D\nabla^2 n(r,t) = \frac{D}{r}\frac{\partial}{\partial r}\left(r\frac{\partial n(r,t)}{\partial r}\right). \tag{5.17}$$

This leads to the Gaussian particular solution

$$n(r,t) = \frac{q}{\pi\left(4Dt + r_0^2\right)} \exp\left(-\frac{r^2}{4Dt + r_0^2}\right), \tag{5.18}$$

which defines the radial distribution of ionization at any time after formation. A picture of the development of the echo over time can be constructed by evaluating the total backscatter from the column of ionization as it expands under diffusion.

5.3 Echo Decay

Following McKinley [1961], the time evolution of the scattered amplitude from the trail can be obtained by considering the amplitude of backscatter from a slice of the trail of unit length in a plane perpendicular to the trail axis. If the slice is divided into annular rings of thickness dr, the amplitude contributed by each ring at time t is

$$dA = 2n(r,t)rdr \int_0^{\pi} \sin\left(2\pi ft - \frac{4\pi r}{\lambda}\cos\theta\right) d\theta = 2\pi n(r,t) J_0\left(\frac{4\pi r}{\lambda}\right) rdr \sin 2\pi ft. \tag{5.19}$$

Integrating across the radius of the slice and removing the phase angle, which is zero for all annular rings, the backscattered amplitude of the entire slice is

$$A_R(t) = 2\pi \int_0^{\infty} n(r,t) J_0\left(\frac{4\pi r}{\lambda}\right) rdr \tag{5.20}$$

This can then be used to describe the decay of the observed backscatter over time with the ratio

$$\frac{A_R(t)}{A_R(0)} = \frac{\int_0^{\infty} n(r,t) J_0\left(\frac{4\pi r}{\lambda}\right) rdr}{\int_0^{\infty} n(r,0) rdr}. \tag{5.21}$$

On integration the denominator is reduced to q. Inserting the electron volume density given by equation 5.18 and integrating [Magnus and Oberhettinger, 1949], the decay of the echo is given by

$$\frac{A_R(t)}{A_R(0)} = \exp\left(-\frac{16\pi^2 Dt}{\lambda^2}\right) \exp\left(\frac{-4\pi^2 r_0^2}{\lambda^2}\right) \tag{5.22}$$

The backscattered power is then

$$\frac{P_R(t)}{P_R(0)} = \left(\frac{A_R(t)}{A_R(0)}\right)^2 = \exp\left(-\frac{32\pi^2 Dt}{\lambda^2} - \frac{8\pi^2 r_0^2}{\lambda^2}\right). \tag{5.23}$$

As the initial radius term is constant at all times, it can be ignored in the consideration of the time decay. Solving for the time taken for the echo intensity to decay by a factor of e^{-1} yields the echo decay constant [Herlofson, 1947],

$$\tau = \frac{\lambda^2}{32\pi^2 D}. \tag{5.24}$$

Hence, the ambipolar diffusion coefficient can be inferred from the decay time of underdense meteor echoes. Combined with equation 5.16, the underdense echo decay time constant, τ, provides a means to infer a diagnostic temperature/pressure parameter for the atmosphere.

The process of echo decay is demonstrated in figure 5.3. The attenuation due to diffusion causes an exponential decay in the observed backscatter. In the Cornu spiral interpretation, the second spiral in the upper right is drawn back towards the origin as the echo decays.

5.4 Effects of Trail Parameters on Echo Decay

The estimation of ambipolar diffusion coefficients using meteor echo decay times has been developed using assumptions of a Gaussian initial distribution, a constant electron line density, instant formation across the field-of-view, a uniform diffusion coefficient along the trail, and the production of ionization by a single ablating particle. In order to assess the reliability of diffusion coefficient estimates, it is necessary to address the effects of deviations from these conditions. To this end, we will address what effect changes to these conditions will have on the observed decay times of meteor echoes.

5.4.1 Effect of non-Gaussian initial distribution

Jones [1995] predicts a non-Gaussian initial radial distribution of ionization and examines the effect on echo decay time by using a Fourier approach. The Fourier transform of the diffusion equation is given by

$$\frac{\partial n(r,t)}{\partial t} = D\nabla^2 n(r,t) \Leftrightarrow \frac{\partial a(k,t)}{\partial t} = Dk^2\nabla^2 a(k,t), \tag{5.25}$$

where $k = 4\pi/\lambda$. The Fourier-transformed form of the diffusion equation has the solution

$$a(k,t) = a(k,0)\exp(-Dk^2 t), \tag{5.26}$$

which leads to the exponential decay constant $\tau = D^{-1}k^{-2}$. Therefore, underdense meteor echoes decay exponentially with the same time constant, regardless of their initial distribution.

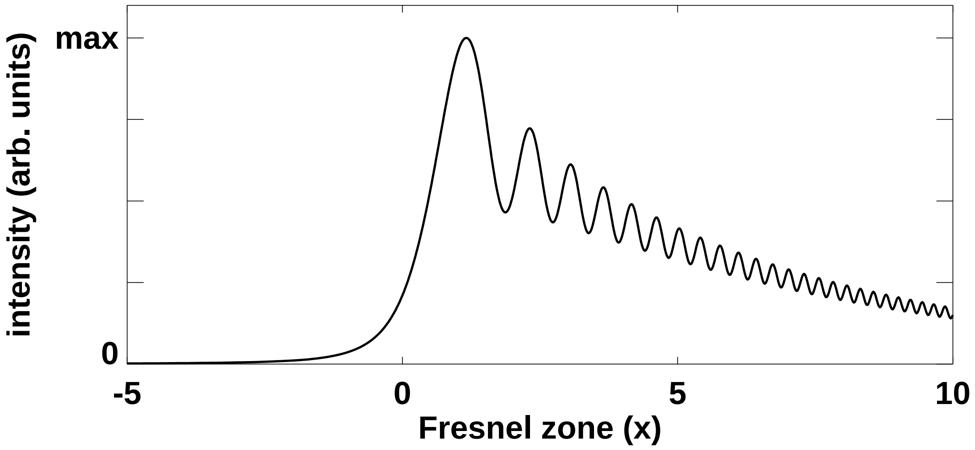

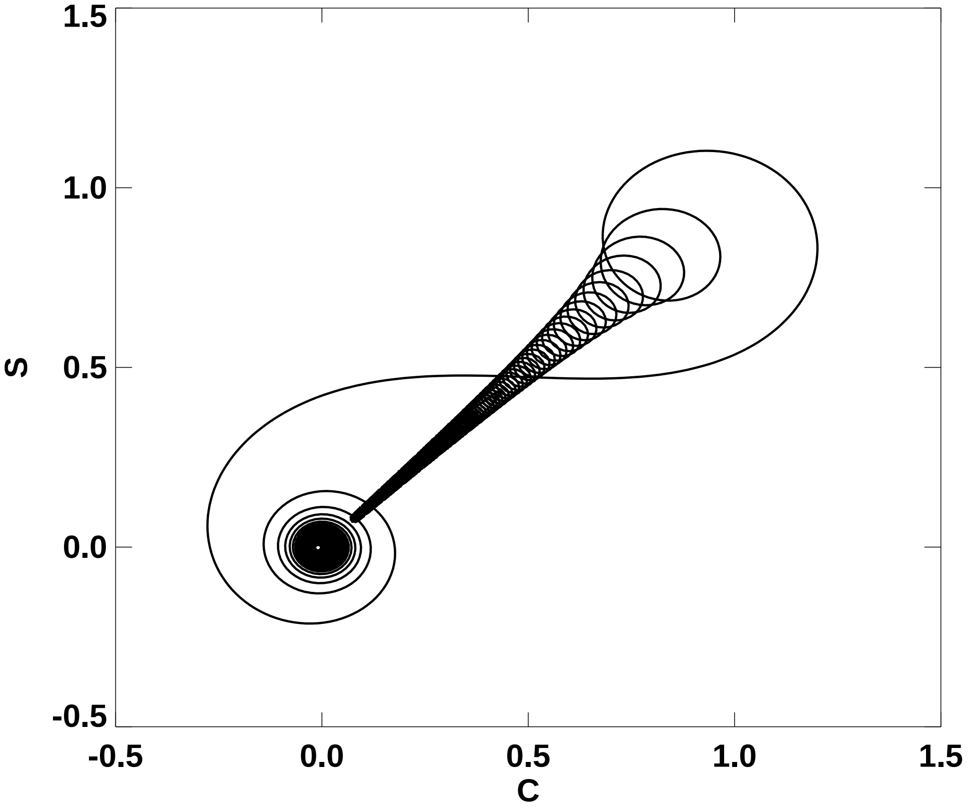

Figure 5.3: Top: Observed intensity of a decaying meteor echo diffraction pattern as a function of the path length traveled, measured in units of Fresnel zone length. Units of intensity are arbitrary, depending on the electron density of the meteor trail and the sensitivity of the observing radar. The exponential decay is produced by an ambipolar diffusion coefficient of 2.0 m^2 s^{-1}. Bottom: Associated Cornu spiral.

5.4.2 Non-constant electron line density

In the preceding work, it has been assumed that the electron line density of the meteor trail is constant along the length of the trail. As figure 4.5 shows, q undergoes a rapid increase and decrease as evaporation starts and stops. In order to gauge the reliability of meteor diffusion estimates, it is necessary to understand what, if any, effect a non-constant values of q will have on the echo decay time.

Should the electron line density vary near the specular point of the trail, the observed diffraction pattern will be affected. Under this condition, q must be included inside the Fresnel integrals. The effect of diffusion can be included by inserting a reflectivity coefficient for each point along the trail, based on equation 5.20. The modified Fresnel integrals taking into account non-constant q and attenuation due to diffusion are given by

$$C = \int_{-\infty}^{x} A_R(\Delta t) q(x) \cos\frac{\pi x^2}{2} dx \qquad S = \int_{-\infty}^{x} A_R(\Delta t) q(x) \sin\frac{\pi x^2}{2} dx, \tag{5.27}$$

where $\Delta t = t - s/v$ indicates the time since the passage of the meteoroid at position $x \leftrightarrow s$.

The effect of a non-constant value of q on the observed diffraction pattern was evaluated by calculating $C^2 + S^2$ from the numerical integration of equation 5.27. An electron line density was defined by a 5 km wide Gaussian distribution centered 5 km before the specular point for the case of decreasing q and 5 km past the specular point for the case of increasing q. The dimensions of the distribution of q were selected to be of approximately the same size as the electron line density profiles produced by numerical simulations in Chapter 3. A diffusion coefficient of 3 $\mathrm{m}^2\ \mathrm{s}^{-1}$ was used, based on the average model value of D around the peak detection height.

The results, shown in figure 5.4 show that the decay properties of the echo are unaffected by variations in electron line density. Smooth changes in electron line density along the length of the meteor path only affect the amplitude of the Fresnel oscillations. Variations in electron line density do not affect the average intensity or the rate of decay from the maximum value. Therefore, meteors that are detected with

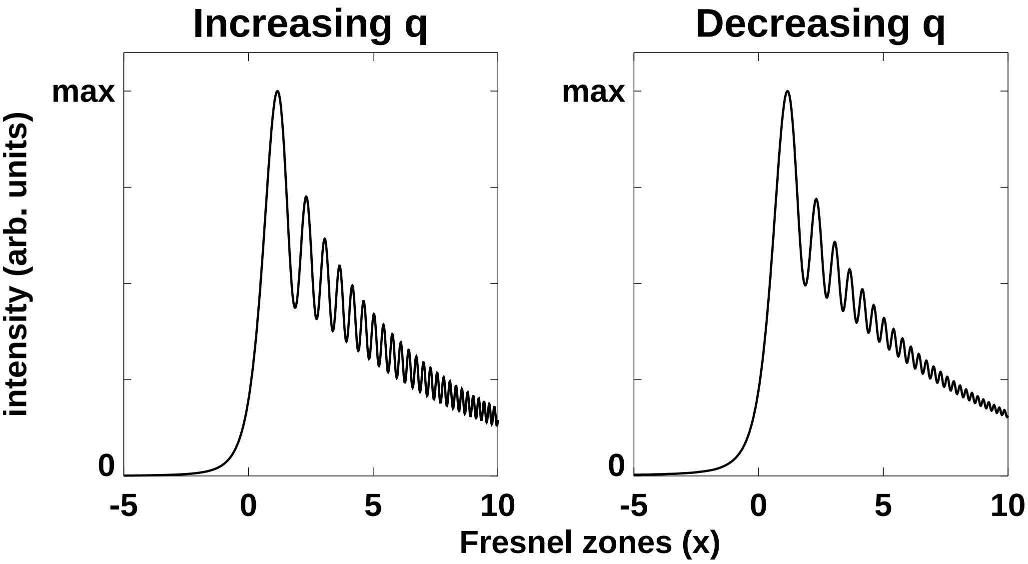

Figure 5.4: Effect of varying electron line density on the intensity of a meteor echo diffraction pattern. Left: Increasing electron line density during trail formation. Right: Decreasing electron line density during trail formation. Units of intensity are arbitrary, depending on the electron density of the meteor trail and the sensitivity of the observing radar.

the specular point located in a region of varying q will still provide reliable diffusion coefficient estimates.

5.4.3 Finite velocity

The formulation for echo evolution given by equation 5.27 provides the additional benefit of demonstrating the lack of any appreciable effect of finite velocity. As the trail is not instantly formed, diffusion begins at different times along the length of the trail. Areas of the trail further back from the meteoroid are formed first and begin diffusing prior to the formation of the trail further along the trail axis. This does not affect the overall decay of the trail, because the time taken for the meteor to form a trail across the central Fresnel zones is small in comparison to the time taken for the echo intensity to decay due to diffusion. Additionally, once formed, all regions of the trail still undergo the same exponential decay in backscatter intensity determined by equation 5.22, resulting in the same decay properties for the entire trail.

5.4.4 Non-constant diffusion coefficient

The ambipolar diffusion coefficient generally varies with height, an example of which is seen in figure 3.3. This implies that the diffusion coefficient is not constant along the length of a trail from a descending meteor, raising the possibility that decay times may not be representative of the diffusion coefficient at the specular point.

In order to evaluate the impact of a varying ambipolar diffusion coefficient along the length of the trail, a similar numerical simulation was performed as described for the case of non-constant q. In this case, the electron line density was held constant, while the reflectivity, represented by $A_R(t, x)$, was produced using a varying ambipolar diffusion coefficient. The diffusion coefficient distribution was defined by a value of 3 $\mathrm{m}^2\ \mathrm{s}^{-1}$ at a height of 90 km with a gradient of $\log_{10} D$ of +0.08 km^{-1}. The total signal was then integrated along the length of the trail as the meteoroid traveled past the specular point at altitudes of 85 and 95 km.

The results of the numerical simulation indicate that variation in the ambipolar diffusion coefficient along the length of the trail has a negligible effect on the decay time compared with the decay time that would be expected based on the diffusion coefficient at the specular point. This is due to the small region within about ±1 Fresnel zone that is responsible for almost all of the backscattered signal amplitude. This segment of the trail is sufficiently short that, even in a strong vertical diffusion coefficient gradient environment, only the diffusion coefficient in the immediate vicinity of the specular point contributes appreciably to the decay of the echo.

For example, a 33 MHz radar detecting a meteor at a range of 200 km has a Fresnel zone length of 675 m, which indicates that the bulk of the backscatter is produced within a 1.2 km segment of the trail. Furthermore, for non-vertical angles-of-entry, the vertical component of the trail is small compared with the height scale over which the diffusion coefficient significantly changes.

5.4.5 Fragmentation

Elford [2004] used values of trail reflectivity obtained by Fresnel transforms of echoes to demonstrate that meteoroids regularly fragment during ablation. The multiple fragments can then each contribute a sub-trail, which taken together, produce the cumulative backscatter for a single meteor event.

In the case of coaxial fragmentation, individual fragments are spaced along the trail axis behind a lead fragment. This can occur when different sized fragments are released, which will each be decelerated at different rates according to their sizes. Alternatively, it can occur when fragments are ejected at a non-negligible velocity or if the train is formed by a collision prior to atmospheric entry. In the case of coaxial fragments, the observed backscatter amplitude is a superposition of the diffraction patterns of the individual sub-trails. This is similar to the case of varying electron density discussed in section 5.4.2.

The effect of coaxial fragmentation was examined by numerically simulating the observed backscatter from trains of ablating meteoroids. This was accomplished by

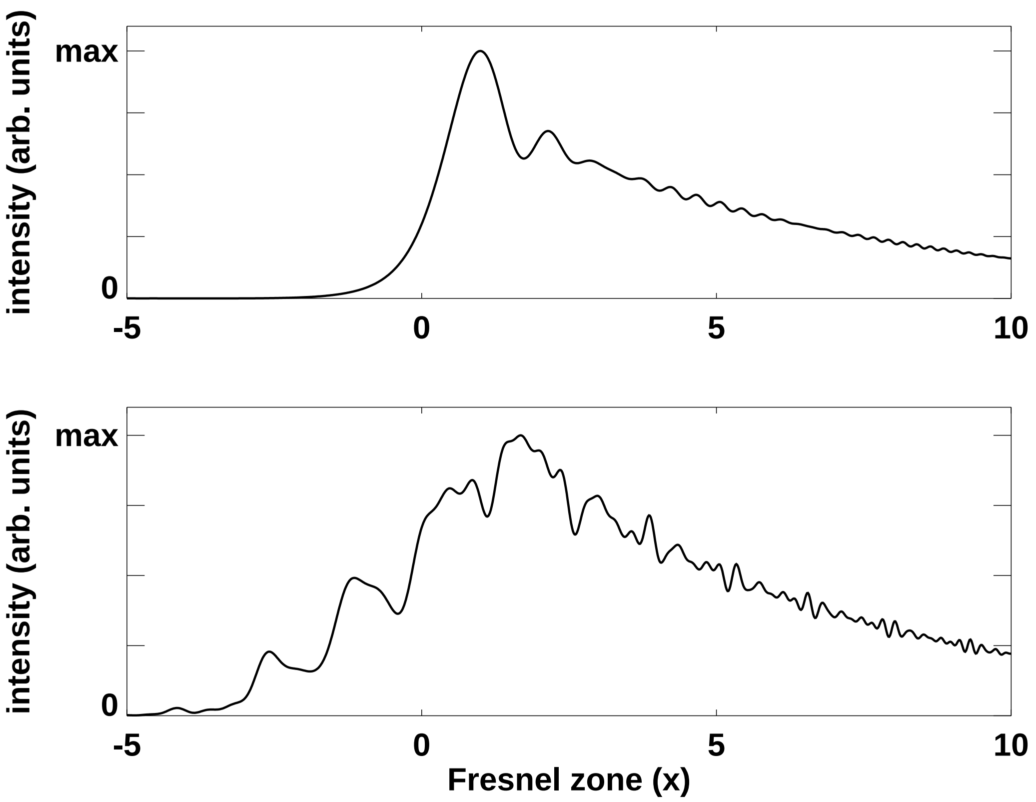

Figure 5.5: Top: Simulated observed echo for a train of 4 equal-size meteoroids at 100 m spacing. Bottom: Simulated observed echo for a train of 4 equal-size meteoroids at 1 km spacing. Calculated for a 9.1 m wavelength radar at a range of 200 km. x is located at the midpoint of the trains. Units of intensity are arbitrary, depending on the electron density of the meteor trail and the sensitivity of the observing radar.

adding the Fresnel integrals from equation 5.27 for a series of meteors prior to the calculation of $C^2 + S^2$. This was done for a 9.1 m wavelength radar detecting trains at a distance of 200 km. Two types of trains containing four meteoroids each were considered: a 100 m ‘close’ spacing and a 1 km ‘long’ spacing.

In the event of a train of meteoroids along the same axis, two effects may be seen in the resultant echo. For closely spaced fragments, with spacings of less than one Fresnel zone, the Fresnel oscillations will be suppressed as the individual diffraction patterns interfere. The overall decay from the initial maximum is not affected, as can be seen in the top panel of figure 5.5.

The case of widely space fragments may produce more dramatic effects, depending on the relative sizes of the fragments. The bottom panel of figure 5.5 demonstrates the severe case of equal size fragments with wide spacing. In this case, additional sub peaks have occurred prior to the overall maximum and the Fresnel oscillations have been severely distorted. Despite the changes to the overall appearance of the echo, the decay time of the average intensity from the maximum value remains the same.

Figure 5.5 shows two different possible echoes resulting from different spacings of coaxial meteoroid fragments. While significant changes may occur to the fine structure of diffraction patterns, the decay times of the average backscattered intensity from the maximum value remain unchanged. Thus, while fragmentation may be a common phenomenon during meteoroid ablation, it does not affect the observed echo decay time.

5.5 Velocity Estimation

Due to the specular nature of underdense echoes, the traditional method of inferring the velocity of a target by tracking position as a function of time is not possible. The formation of a recognizable diffraction pattern by the backscatter from a meteor trail provides the opportunity to estimate the velocity of the meteoroid. The echo amplitude can be used to directly estimate the velocity of the meteor or amplitude and phase information can be used to decompose the echo, yielding a trail reflectivity profile in addition to velocity information.

5.5.1 Echo slope

Velocity can be expressed as a function of x, the meteoroid position along the trail axis expressed in Fresnel zones. For a meteoroid traveling along the trail axis at a rate

dx/dt the velocity in m s^{-1} is given by

$$v = \frac{(R\lambda)^{1/2}}{2} \frac{dx}{dt}. \tag{5.28}$$

The echo amplitude $(C^2+S^2)^{0.5}$, as shown by the length of the vector depicted in figure 5.1, has a maximum value of 1.657 at $x = 1.217$. The gradient achieves a maximum value of 1 at $x = 0.572$. This geometrical relationship can be used with equation 5.28 to infer the velocity of the meteor (see, e.g., Baggaley et al. [1997]). For an echo that increases in amplitude by ΔA between the maximum gradient point and maximum amplitude point in a time Δt, the velocity is

$$v = \frac{1.657\,(R\lambda)^{0.5}}{2A_{max}} \frac{\Delta A}{\Delta t}. \tag{5.29}$$

This method provides a simple and efficient method of using echo amplitude alone to determine velocity, but relies on a well-behaved diffraction pattern. As was seen in figure 5.5, severe fragmentation may distort the leading edge of the diffraction pattern, prohibiting accurate measurement of the echo amplitude slope.

5.5.2 Fresnel transform

If phase information is available with echo amplitude, the diffraction pattern can be decomposed to provide an image of the trail. Elford [2001] describes a method using the Fresnel transform, by which the complex echo amplitude can be transformed to provide the reflectivity along the trail. He shows that received complex amplitude $A_R(t)$ at time t can be transformed to provide the trail reflectivity as a function of the distance from the meteoroid, y. This process is given by

$$A_R(t) \Leftrightarrow A_R(y) \propto \int_{-\infty}^{\infty} A_R(t) \exp\left[-i\,(x+y)^2 \frac{1}{2}\left(\frac{4\pi}{R_0\lambda}\right)^{0.5}\right] v \left(\frac{4\pi}{R_0\lambda}\right)^{0.5} dt. \tag{5.30}$$

It should be noted that velocity must be supplied to the Fresnel transform given in equation 5.30. In order to use the transform to obtain a value for the velocity of the meteor, a number of candidate velocities are used in the Fresnel transform. The reflectivity profiles produced by the different supplied velocities are compared to determine the best estimate.

As all ionization is produced behind the meteoroid, the leading edge of the reflectivity has a vertical or nearly vertical slope. Diffusion dominates the reflectivity behind the meteoroid, which should lead to a smooth decay of $A_R(y)$. Using these two criteria, the velocity is selected as the value that produces the sharpest leading edge with a reflectivity profile devoid of oscillations [Elford, 2004].

5.6 Summary

In this chapter, the development of the underdense meteor echo over time has been reviewed and modifications to the standard model have been investigated. The underdense meteor echo is a modified Fresnel diffraction pattern, formed as a column of ionization is left behind a meteoroid traveling across the field-of-view of an observing radar. The distinct diffraction pattern allows the velocity of the meteoroid to be determined from the time dependence of the echo amplitude both with and without phase information. The primary influence on backscattered intensity after the initial maximum is diffusion, which produces a distinctive exponential decay. Measurement of the exponential time decay constant allows the local ambipolar diffusion coefficient to be inferred.

Additional sources of variability to the underdense echo have been examined, in an effort to determine to what extent they influence echo decay times. This was done by performing numerical simulations of underdense echoes with additional properties. It was found that a non-constant electron line density along the length of the trail only affects the relative amplitude of the Fresnel oscillations, but not the decay time of the average backscatter intensity. Similarly, it was found that changes in the diffusion coefficient along the length of the trail do not significantly influence the observed decay time of the echo. This is due to the dominant contributions to backscatter intensity of the central Fresnel zones near the specular point. Fragmentation was found to be capable of causing significant distortions to the fine structure of the diffraction pattern but does not affect the decay time of the average echo intensity.

These negative findings provide a confirmation of the reliability of the echo decay-time method for estimation of the ambipolar diffusion coefficient. By eliminating trail properties as possible contributors to echo decay behavior, an examination of the elements affecting the diffusive process itself can begin. In the next chapter, the possible causes of anomalous diffusion phenomena will be evaluated, including methods to mitigate their impact on atmospheric parameter estimates.

Chapter 6

Anomalous Diffusion

Estimates of the ambipolar diffusion coefficient made using underdense meteor echo decay times depend on the linear diffusion of ionized material in the trail. Linear diffusion is defined as the diffusive transport of material as described by a simple linear differential equation, as given by equation 5.17 for the case of a cylindrical meteor trail. The previous chapter examined the formation and evolution of meteor trails and how diffusion produces an exponential decay in observed backscatter over time. If the diffusion process deviates from simple linear diffusion, it is possible that decay time based estimates of D may be called into question. It is therefore imperative to understand additional processes that may influence the evolution of backscatter from underdense meteor echoes. This chapter will consider deviations from the linear diffusion model of meteor trail due to the presence of multiple ion species and due to the presence of electron absorbing aerosols.

Disagreement in diffusion coefficient estimates, based on echo decay times from two radars with different frequencies observing the same meteor indicate that meteor trails are affected by processes other than simple linear diffusion. Holdsworth et al. [2006] examined simultaneous detections of the same meteors by the co-located 33 and 55 MHz radars operating at Davis Station, Antarctica during 2005. They found that the 33 MHz radar produced systematically higher estimates of the ambipolar diffusion coefficient as compared to the 55 MHz radar.

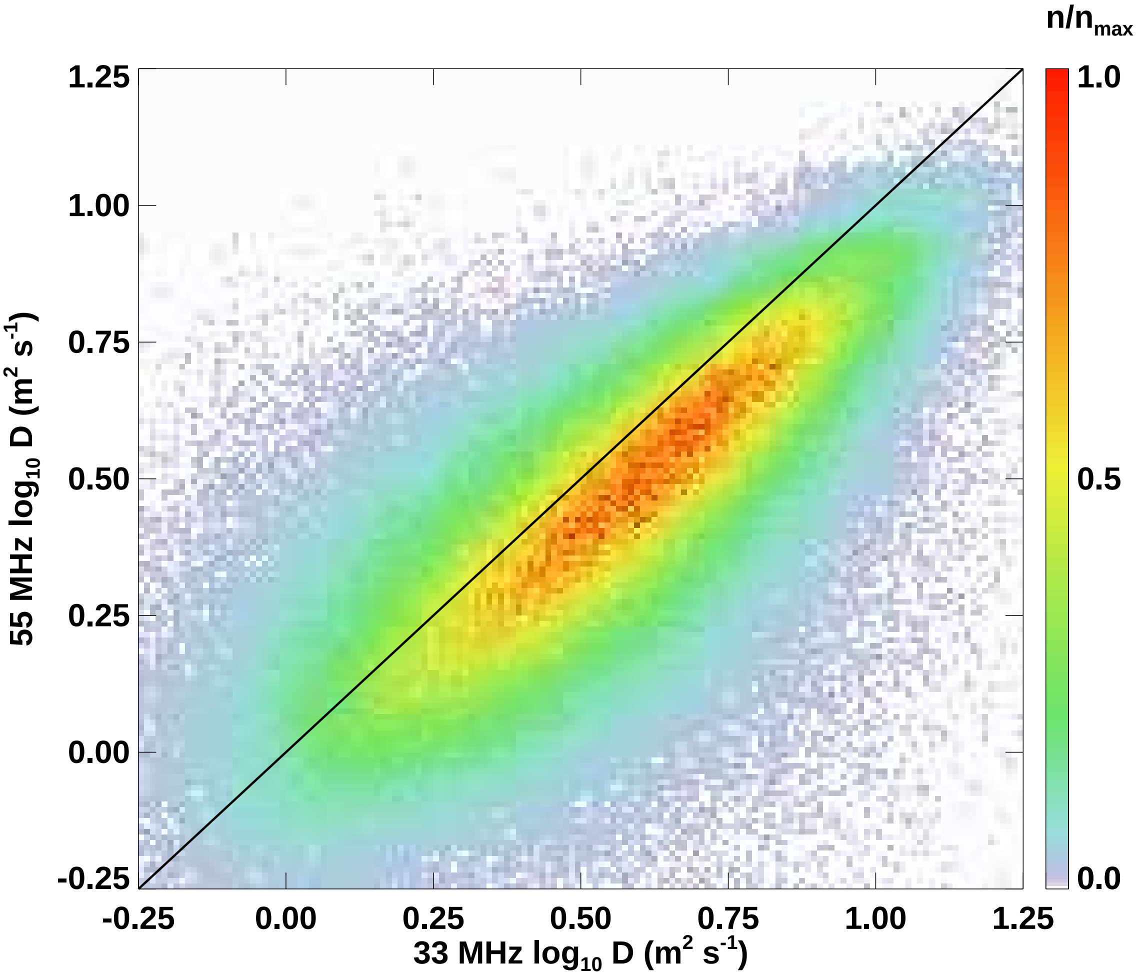

Figure 6.1: Comparison of diffusion coefficient estimates for 224,971 meteors detected simultaneously by co-located 33 MHz and 55 MHz meteor radars at Davis Station, Antarctica during 2009. The solid line indicates where the two estimates are in agreement.

Additional simultaneous detections of meteors observed by both the 33 MHz and 55 MHz radars at Davis Station have been used for this study. Meteor detections for the two radars were classified as coming from the same meteor if they occured on the two radars within a time spacing of 10 seconds and an angular spacing of three degrees of both azimuth and zenith. Over the course of 2009, 224,971 meteors were detected by both radars. Meteor detections above 90 km were not considered, in order to remove any possible contribution of magnetic field effects [Jones, 1991] or plasma instabilities [Dyrud et al., 2001].

The difference in diffusion coefficient estimates can be seen in figure 6.1, with the value of D estimated by the 33 MHz radar systematically larger than that of the 55 MHz radar. This indicates that some process is causing a reduction of longer wavelength decay times relative to those derived from shorter wavelength observations.

It should be noted that the disagreement between the two radars over the value of D is not for separate or overlapping distributions of meteor detections, but for the same meteors detected by both radars. The discrepancy between the two radars has been found to be independent of azimuth or zenith angle, ruling out array or magnetic field effects. There must, therefore, be some mechanism modifying the decay times of the meteor echoes that differently affects the two observing wavelengths.

As the true value of the ambipolar diffusion coefficient is not known, the difference in diffusion coefficient estimates between the two radars has been used to assess the effect of the anomalous diffusion phenomena. The metric used to quantify the deviation between the two different frequencies is the percentage difference in the diffusion coefficient estimate for the same meteor, calculated as $100\times(\log_{10} D_{33} - \log_{10} D_{55})/\log_{10} D_{33}$. Figure 6.2 illustrates the difference in the diffusion coefficient estimates of the two radars as a percentage of the 33 MHz estimate at a number of different altitudes. It can be seen that 33 MHz estimates of D are higher than than the 55 MHz values at all altitudes.

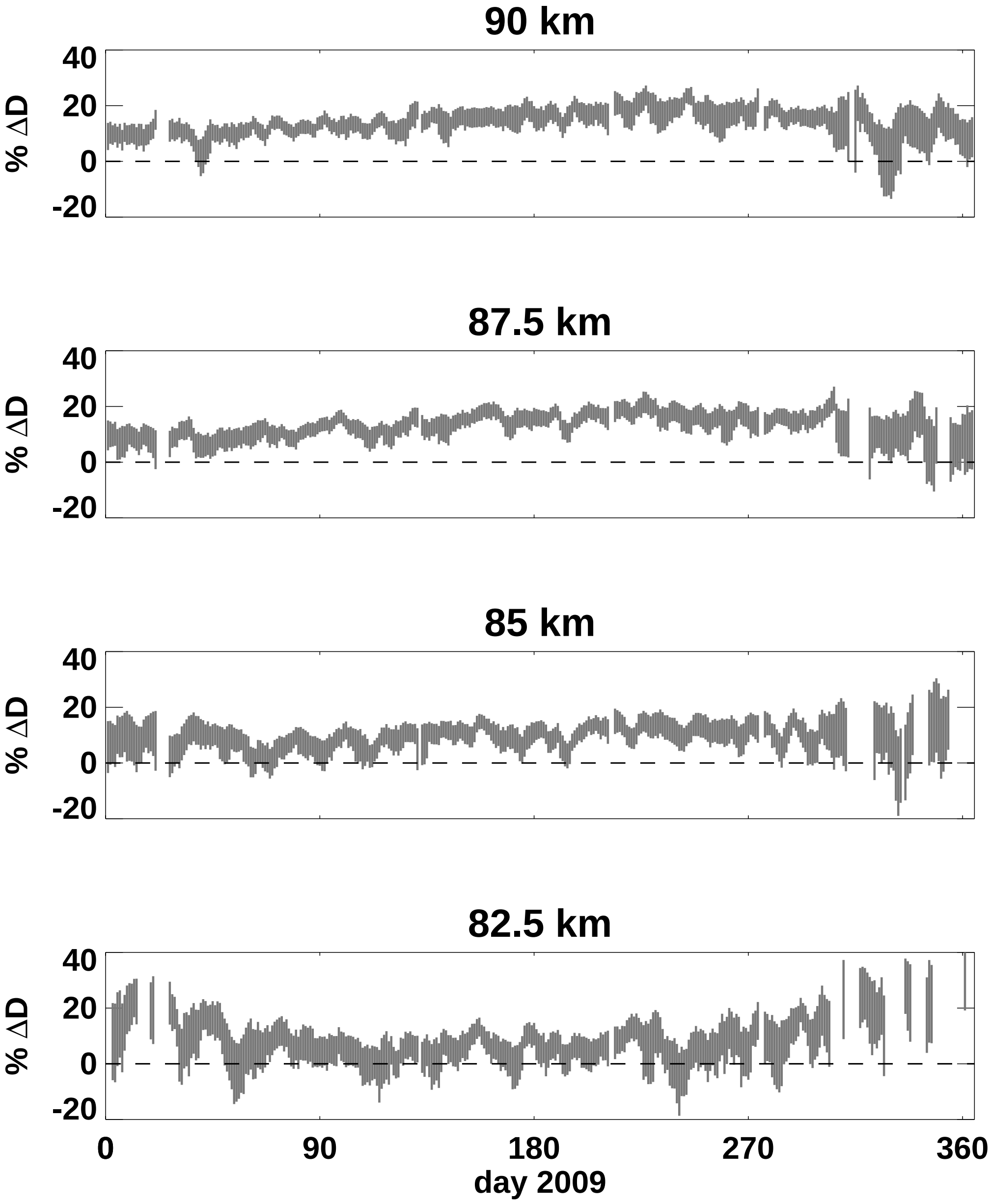

Figure 6.2: Comparison of diffusion coefficient estimates (5-day running mean) at different heights detected simultaneously by co-located 33 MHz and 55 MHz meteor radars at Davis Station, Antarctica during 2009. Each labeled height is the center of a 2 km wide bin. Vertical bars indicate the 95% confidence interval.

6.1 Multiple Ionic Species

The diffusion of multiple species of ions within the meteor trail is not generally considered, due to the lack of an analytic solution to the time dependence of free electron density. As discussed in subsection 5.2.2, an average value of ion mobility is assumed when considering the relation between the rate of diffusion and the local atmospheric parameters. Meteors, however, deposit a number of different constituent elements into the atmosphere as they ablate and atmospheric molecules themselves are ionized by collisions with meteoric material. This produces trails that are a mixture of different ions. The diffusion of mixed ion trails must then be considered in order to determine the effect on observed echo decay times.

The diffusion of ionized material described by equation 5.17 assumes that only one species of ion is diffusing in the meteor trail. In the event that more than one species of ion is present, the radial diffusion equation becomes

$$\frac{dn_i(r,t)}{dt} = -D_i \nabla \cdot \left[\nabla n_i(r,t) + c_i(r,t) \nabla n_e(r,t) \right], \tag{6.1}$$

where n_i is the ion density and c_i is the fractional concentration of the i^{th} component at r, t. It can be seen that 6.1 reduces to equation 5.17 in the event that only one species is present. Keeping the condition of quasi-neutrality, the density of free electrons in the trail is given by

$$n_e = \sum_i c_i n_i. \tag{6.2}$$

This system no longer admits an analytic solution.

6.1.1 Numerical simulation method

The diffusion of multiple species of ions and electrons in a meteor trail was simulated numerically to assess the effect of different initial compositions and distributions on estimates of the ambipolar diffusion coefficient. Equations 6.1 and 6.2 were solved using a 4^{th}-order Runga-Kutta method.

An adaptive time step was implemented such that at no point along the width of the trail did any ion density change by more than 1% over the course of a single time step, with an upper limit of 10^{-3} s. The scattered amplitude was calculated at each point in time using equation 5.20. The diffusion coefficient estimate was then obtained by determining the e^{-1} decay time and using it with equation 5.24.

The spatial basis was constructed so that each point was separated by a distance of 1/50 the largest individual initial radius of all the ions considered. This prevented over-resolution instability of the numerical differentiation of the spatial component of equation 6.1. The density was calculated at 300 points, leading to a maximum distance from the trail axis of about 8-10 m.

As was discussed in subsection 5.2.1, current studies of the initial radius of meteor trails do not differentiate between different ions in the trail and as such, the average values quoted in published works [see, e.g., Bronshten [1983], Jones [1995]] do not specify how constants were arrived at. For this reason, the initial radii, r_0, for different ion species were calculated using the older relation

$$r_0 = \left(\frac{4}{3} N l^2 \right)^{1/2}, \tag{6.3}$$

where the mean free path, l is obtained from equation 5.8 and N is the number of collisions to reach equilibrium. Following the results of Jones [1995], a value of $N = 10$ was used.

The simulation was performed using the initial atmospheric conditions of 3×10^{-6} kg m^{-3} and 180 K, corresponding to average conditions for mid-latitudes around the peak meteor detection height of 90 km. For the values of K_0 quoted in Cervera and Reid [2000] and Hocking et al. [1997] this corresponds to a diffusion coefficient of $D \approx 3.4$ m^2 s^{-1}. Meteor velocity was set at 35 km s^{-1} based on the average velocity seen in detections. Two mixtures of ions were considered, an olivine mixture and an equal mixture of iron and oxygen. The olivine mixture consisted of 62% O, 24% Si, 8% Mg, and 6% Fe [Jones, 1997]. The equal mixture of iron and oxygen ions was used to evaluate the effect of higher relative concentrations of heavier ions on the diffusive properties of the trail.

The initial conditions described were chosen to be representative of the conditions around the peak meteor detection height. Another factor in this decision is that the complexity of the multi-species diffusion problem makes finding stable combinations of physical grid spacing, time steps, and initial conditions difficult. As such, only the representative values for the peak meteor detection height were considered in the simulation. Other altitudes will require further work to determine what, if any, combination of input parameters will produce a viable solution.

The effects of two variables were of interest in simulating the diffusion of multiple species of ions: the effect of different chemical compositions and the effect of differing initial radii for each ion species. Each composition was simulated using individual radii for each ion species and again using an initial radius obtained from a weighted average of the different individual radii of the ions present. The decay times were then determined for wavelengths of $5 - 10$ m for the four scenarios considered. The effect of the different initial conditions was observed by comparing the diffusion coefficient estimated from decay times with the average diffusion coefficient of the ions in the trail.

6.1.2 Simulation results: common initial radius

For the case of a single initial radius for all ions in the trail, there was negligible wavelength dependence on the estimated diffusion coefficient, as shown in the lower left panel of figure 6.3. The estimated value of D was about 0.5% lower than the average diffusion coefficient for the olivine composition and about 1.1% lower for the Fe-O combination. The slight reduction in decay times is due to the emergence of non-uniform diffusion, as can be seen in the upper left panel of figure 6.3.

Diffusion for ions sharing a common initial radius is initially uniform across the width of the trail. With a single initial radius, the values of c_i are constant for all r at $t = 0$. As the trail develops, the presence of free electrons moderates the diffusion of the different ions, enhancing the diffusion of heavier ions and retarding the diffusion

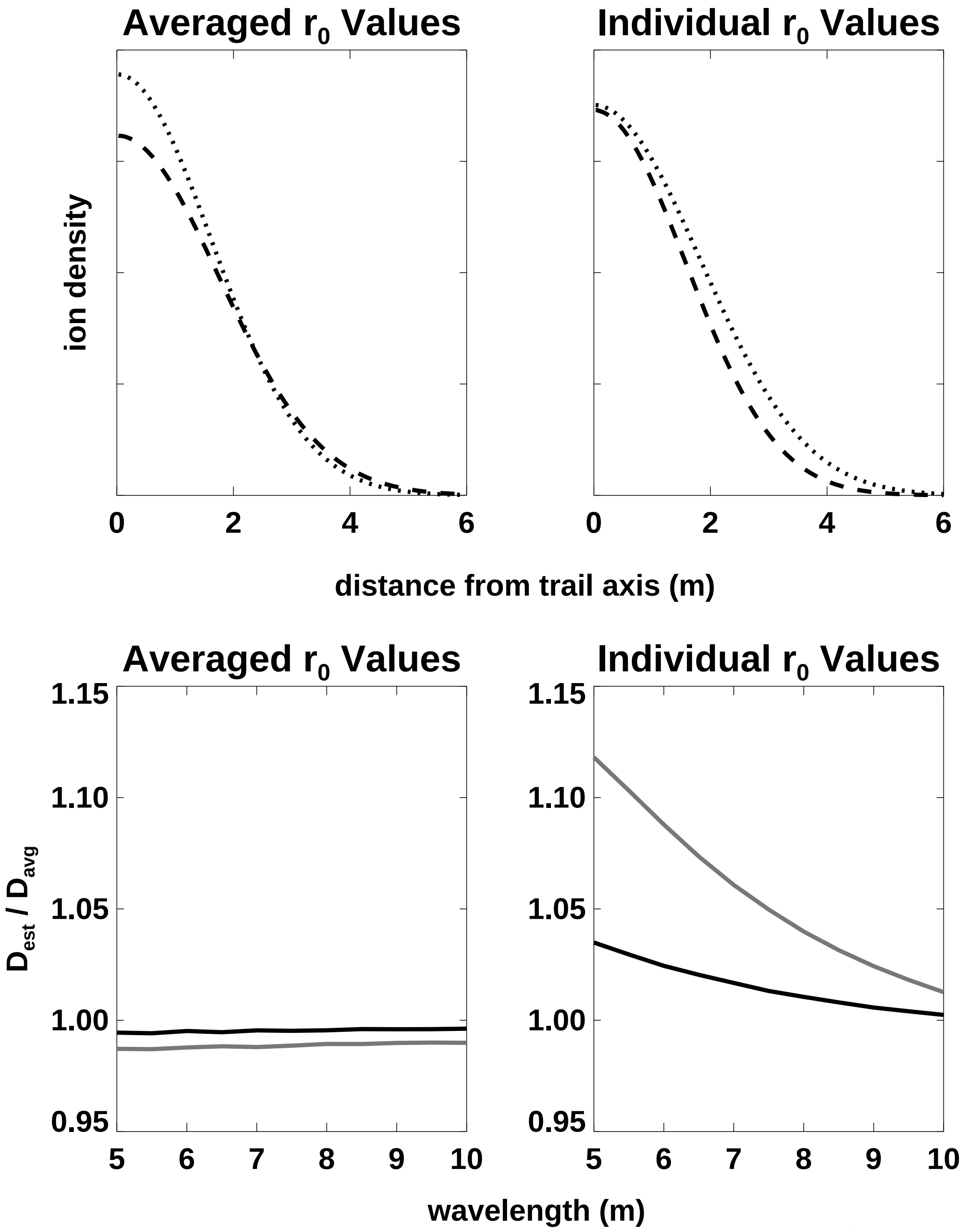

Figure 6.3: Top left: O (dashed) and Fe (dotted) ion concentrations at e^{-1} decay point for a 10 m wavelength radar using a single initial radius for all ions. Top right: O (dashed) and Fe (dotted) ion concentrations at e^{-1} decay point for a 10 m wavelength radar using individual initial radii for each ion. Bottom left: Deviation of estimate from average diffusion coefficient for averaged initial radius for olivine (dark) and equal Fe/O mix (light). Bottom right: Deviation of estimate from average diffusion coefficient for individual ion initial radii for olivine (dark) and equal Fe/O mix (light).

of the lighter ions. This smoothing effect of the electron component of the trail is not complete, however, and gradients in the concentration of different ions occur as quantities of lighter ions diffuse slightly faster than heavier ions, as is shown in the left column of figure 6.4. This in turn leads to a gradient in D along the radius of the trail, which produces non-linear diffusion as the trail develops.

The presence of electrons in the trail and the condition of quasi-neutrality restrain the development of concentration gradients, but they are not eliminated entirely. The result is a slight increase in the concentration of lighter ions in the periphery of the trail and persistent core of heavy ions in the center of the trail. The diffusion of the central core is further retarded by the evacuation of the lighter ions, leading to a lower effective diffusion coefficient near the trail axis. The observed result is a small extension in decay times, which leads to the slightly lower estimates of D than would otherwise be seen if only a single type of ion was diffusing with an average value of the diffusion coefficient.

6.1.3 Simulation results: individual initial radii

The inclusion of individual initial radii for each ion produced noticeable variations in the estimate of the diffusion coefficient with a strong wavelength dependence, as seen in the lower right panel of figure 6.3. The simulations predicted that trails comprised of ion distributions with individual initial radii will experience a reduction of the decay time for lower wavelengths. This implies that radars with different wavelengths observing the same meteor trail will produce different estimates of the ambipolar diffusion coefficient, with smaller wavelengths increasingly biased towards higher values.

The early diffusion of ions with individual initial radii is dominated by the outward movement of lighter ions that are initially distributed close to the trail axis. Light ions have a small diffusion cross-section, which leads to a small value of r_0 using equation 6.3. Thus, the relative concentration of ions is dominated by heavy ions at the edge of the trail and light ions in the center of the trail. The high effective diffusion coefficient near the center of the trail and low effective diffusion coefficient further out from the

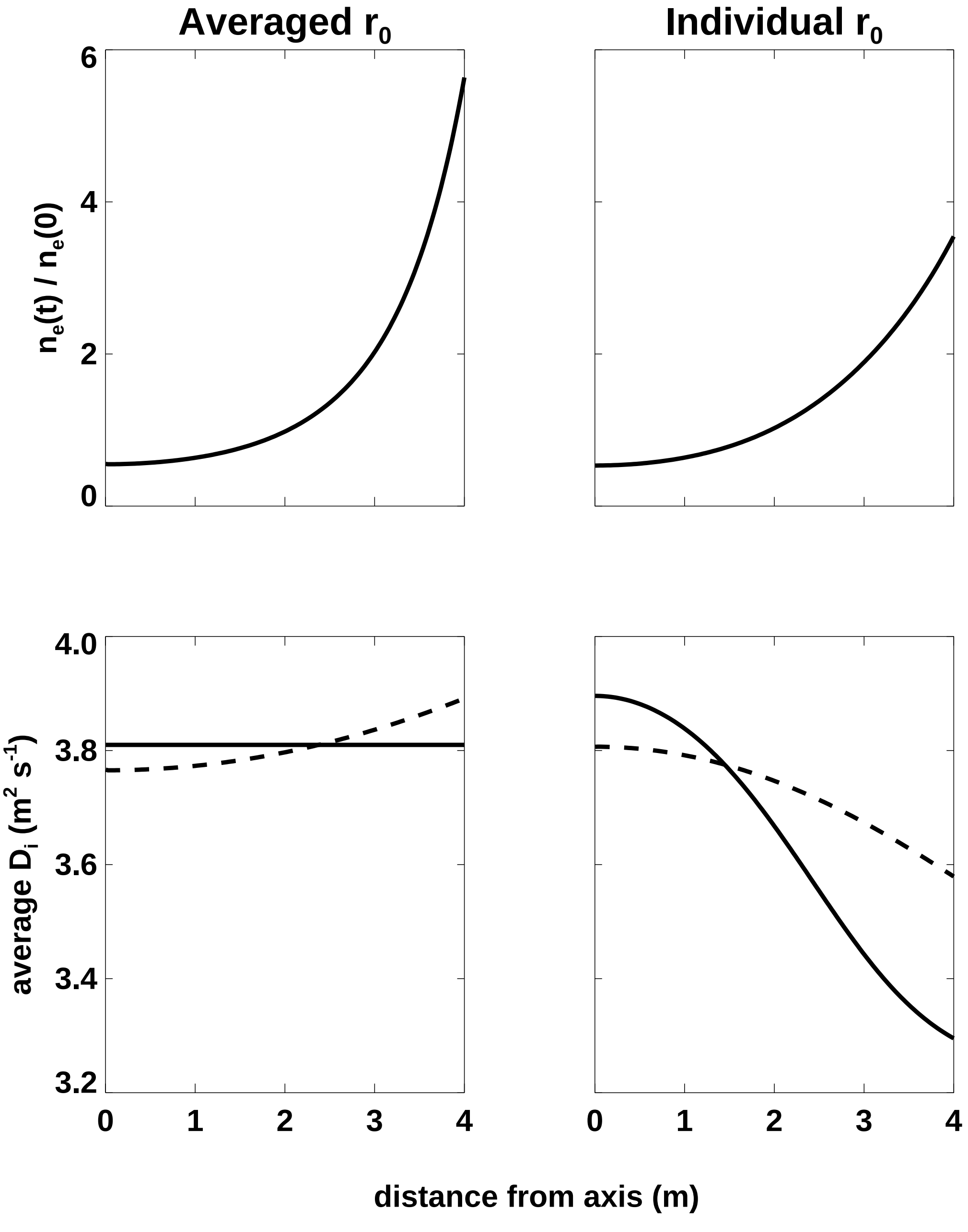

Figure 6.4: Fe-O numerical simulation example. Left column: Diffusion with an average value of r_0. Right column: Diffusion using individual values of r_0 for each ion type. Top row: Ratio of initial electron density with final density (e^{-1} decay time for a 10 m radar). Bottom row: Comparison of initial (solid) and final (dashed) average diffusion coefficient.

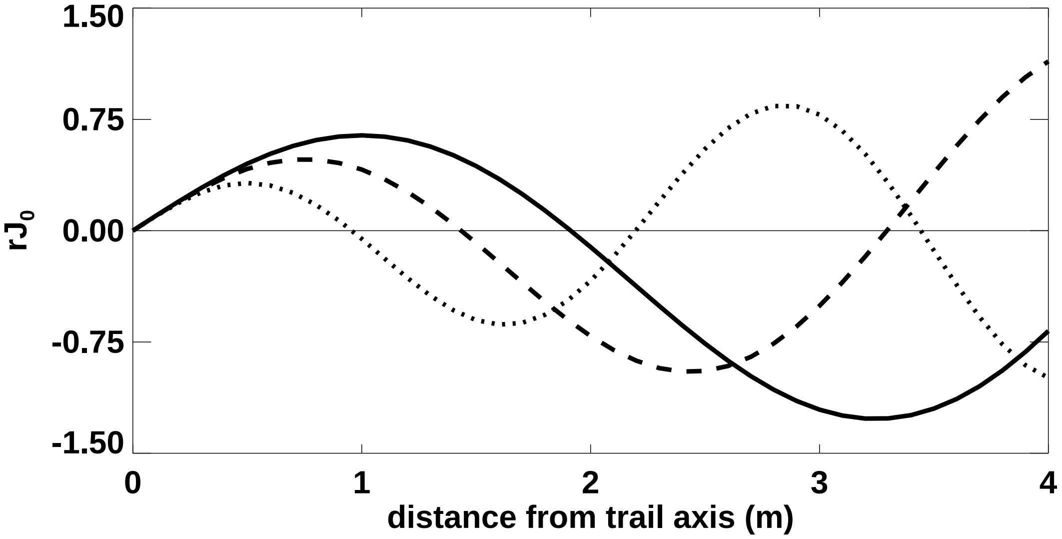

Figure 6.5: Bessel weighting function $rJ_0\left(4\pi r/\lambda\right)$ for 5 (dotted), 7.5 (dashed), and 10 m (solid) wavelengths.

axis leads to a rapid decrease in electron density near the trail axis with smaller changes to the electron density at the edges. This effect is illustrated in the right column of figure 6.4, as the faster diffusing oxygen ions increase the diffusion coefficient at the edges of the trail over time as they migrate out from their small initial radius.

The backscatter amplitude obtained from equation 5.20 can be thought of as a convolution of two terms: the electron density distribution, n_e, and a product of radius, r, and a Bessel function $J_0\left(4\pi r/\lambda\right)$. This latter term acts as a weighting coefficient, determining the strength of the backscatter from different points along the trail radius. As seen in figure 6.5, this is an oscillatory function that increases in amplitude with distance from the tail axis. The value is initially positive, with the point at which it first becomes negative increasing with value of the wavelength considered.

The echo decay process itself can be understood in terms of the interplay between shifting values of n_e and the radial-Bessel function product. The movement of electron density away from the axis decreases the positive contribution to echo amplitude. At the same time, increasing electron density in the negative regions of the Bessel function adds a negative contribution to the echo amplitude. Scattering from zones of the Bessel function with opposite sign will interfere destructively and scattering from zones with the same sign will add constructively.

For a trail undergoing a modified diffusion process, the observed deviation of the decay time depends not only on the magnitude of the change in diffusion, but where along the radius the changes are taking place in relation to the positive and negative regions of the radius-Bessel function product. In fact, the amplitude decrease due to enhanced diffusion in the positive range of J_0 may be offset by retarded diffusion in the negative J_0 regions.

In the presented case of individual initial radii, the first negative zone of the Bessel function of shorter wavelengths occurs around the initial radii of the ion distributions. Hence, the initial rapid decline in electron density close to the trail axis causes a significant decrease in backscattered amplitude. The slowly diffusing heavy ions simultaneously contribute a steady increase in density in the negative region of the Bessel function. These behaviors combined reduce the decay time as compared to the case of a single type of ion. The result is an increase in the diffusion coefficient for shorter wavelengths.

For longer wavelengths, the first positive region of the Bessel function encompasses most of the electron density distribution throughout the early stages of diffusion. As the central core of light ions diffuses outward, it mixes with the slower diffusing heavy ions that were initially scattered in a wider distribution about the axis. By the time that electron density begins to rise in the negative region of the Bessel function, the ion concentrations are well mixed, with similar distribution widths. This leads to a similar effect on the decay time as seen for the case of the averaged initial radius, with wavelengths on the order of twice the initial radii or greater, yielding diffusion coefficient estimates close to or slightly below the average value.

6.1.4 General considerations

The wavelength dependence of the deviation of the diffusion coefficient estimate from the average value increases as the quantity of heavy ions in the trail approaches the quantity of light ions. The olivine composition used in numerical simulations demonstrated a small wavelength dependence, because the structure of the ion densities is dominated primarily by the light ions O and Si. In contrast, binary Fe-O combination was more affected. This is due to the interaction of comparable quantities of ions with dramatically different mobilities, which exacerbates the non-linear diffusion effects.

The ambipolar diffusion coefficient increases and atmospheric density decreases in an approximately exponential fashion with regard to height, as illustrated in figure 3.3. This results in an increase in the initial radius of meteor trains with regards to height, while also increasing the rate of diffusion. The results described above can be generalized for differing atmospheric conditions primarily by considering the effect of atmospheric density on the initial radius of meteor trails with regards to the Bessel function for specific wavelengths.

At lower altitudes, the initial radius decreases, providing initial ion distributions contained entirely within the first zone of the Bessel function for all typical VHF meteor radar wavelengths. As a result, all wavelengths experience a slight increase in the observed estimate of the diffusion coefficient when compared with the case of linear diffusion using a single average value. The wavelength dependence of an increasing diffusion coefficient estimate with decreasing wavelength is still present, but decreases in severity at lower altitudes.

At higher altitudes, large initial radii complicate the evolution of observed backscatter over time, particularly at smaller wavelengths. Above 95 km, ion initial radii encompass the first several zones of the Bessel function for typical radar wavelengths. This produces lower overall signal strength as the contribution of negative and positive regions cancel, which is responsible for the high altitude cutoff discussed in Chapter 3. Over time, the development of the echo can deviate substantially from the usual exponential decay as electron density moves between positive and negative zones of the Bessel function. The most severe cases can produce significantly extended decay times, albeit with backscatter intensity several orders of magnitude below conventional underdense echoes. As such, the actual detection of high altitude extended decay time underdense echoes produced by this mechanism is unlikely.

6.2 Aerosol Absorption

The mesosphere region is populated by small particles which are likely formed by the condensation of evaporated meteoric matter [Hunten et al., 1980], the remains of partially evaporated meteoroids slowed to low velocities (see Chapter 3), and ice crystals that form in extremely cold conditions [Cho et al., 1994]. These particles, which may carry a charge, can serve as a sink for free electrons in meteor trails. Electrons are lost from the trail through attachment to aerosol particles, at a rate determined by the size and charge of the aerosols. The general approach of Havnes and Sigernes [2005] has been followed in the investigation of this phenomenon, with the implementation of more accurate numerical simulation methods.

The diffusion of a meteor trail in a background of electron-absorbing aerosol particles is given by

$$\frac{dn_e(r,t)}{dt} = -D\nabla^2 n_e(r,t) + \frac{\partial n_d}{\partial t}. \tag{6.4}$$

The loss of electrons to absorbing particles as a function of electron density, n_e, the absorbing particle density, n_d, and the electron capture rate, R_{ed}, is given by

$$\frac{\partial n_d}{\partial t} = -n_e(r,t)n_d(r,t)R_{ed}. \tag{6.5}$$

The electron capture rate for a spherical aerosol particle with charge Z_d and radius r_d is given by [Draine and Sutin, 1987]

$$R_{ed} = \pi r_d^2 \left(\frac{8kT_e}{\pi m_e}\right) \left[1 + \left(\frac{Z_d}{\eta}\right)\right] \left[1 + \left(\frac{2}{\eta + Z_d}\right)^{1/2}\right], \tag{6.6}$$

where $\eta = 4\pi\epsilon_0 r_d kT_e/\mathrm{e}^2$. In the event that the particle is neutral, this reduces to

$$R_{ed} = \pi r_d^2 \left(\frac{8kT_e}{\pi m_e}\right)^{1/2} \left[1 + \left(\frac{Z_d}{2\eta}\right)^{1/2}\right]. \tag{6.7}$$

The dependence of the electron capture rate, R_{ed}, on both the particle radius, r_d, and charge, Z_d, produces a large variety in the possible aerosol scenarios to consider. If the consideration is limited to a single electron absorbed per aerosol particle, the situation is simplified greatly. Under this condition, the detailed properties of the aerosol particle may be ignored and a value of R_{ed} can be supplied directly to equation 6.4. It is not necessary to delineate between different combinations of charge and radius, but rather the possible regimes can be categorized by their relative capture rate. Equations 6.6 and 6.7 imply that increases in charge and radius will increase R_{ed}. For the purposes of considering meteor trail evolution, a direct consideration of a range of values for R_{ed} is sufficient, without a detailed examination of all possible atmospheric aerosol configurations.

6.2.1 Numerical simulation method

Havnes and Sigernes [2005] considered the possible effects of aerosol absorption on the observed decay times of meteor echoes. Their simulations predicted that an 8 m wavelength radar would experience reduced decay times for meteors with initial electron line densities of about $10^{13} - 10^{14}$ electrons m^{-1}. The simulations, however, relied on the assumption that the electron density distribution is Gaussian at all times, which breaks down when considering the low density regions at the edge of the trail.

Younger et al. [2008] overcame this by using a hybrid Fourier-finite time method to calculate the diffusion of meteor trails in absorptive environments. It has since been found that 4^{th}-order Runga-Kutta method is sufficient for decay time calculations and has the advantage of being more computationally efficient. The goal of the simulations presented here was to extend previous work across a range of commonly used VHF meteor radar wavelengths. This investigation also seeks to relate the results of the numerical simulations to the Davis Station dual-frequency data being used as a case study. This will allow a direct comparison of the behavior of the simulated meteor echoes and actual observations.

The effect of the absorption of trail electrons by background aerosol particles was investigated by numerically simulating the diffusion of meteor trails in different absorptive regimes. The predicted decay time for different wavelengths was then compared with the decay time that would occur if only diffusion was occurring, as given by equation 5.24.

A 4^{th}-order Runga-Kutta method was used to simultaneously solve equations 6.4 and 6.5, for two different altitudes and a variety of aerosol configurations. The solution was calculated at 10^{-5} s time steps at 200 points from the trail axis with a grid spacing of $r_0/20$. Atmospheric parameters were set to $D = 2$ m^2 s^{-1}, $r_0 = 0.5$ m for 85 km and $D = 3.4$ m^2 s^{-1}, $r_0 = 1.0$ m for 90 km. Following the results of Rapp [2000], values of R_{ed} considered ranged from $10^{-10} - 10^{-8}$ m^3 s^{-1}. Aerosol densities considered ranged from 10^9-10^{10} m^{-3}, based on the findings of Megner et al. [2006]. In order to compare the results of the simulation to existing data, radar wavelengths of 5-10 m were considered. Echo amplitude was calculated using equation 5.20, with the decay time determined by the time taken to reach e^{-1} of the initial backscatter amplitude for each wavelength.

6.2.2 Numerical simulation predictions

A selection of predicted decay time reduction percentages are shown in figure 6.6. Negative values indicate that decay times are extended for the particular combination of radar wavelength and electron line density. It was found that the effect of aerosol absorption of trail electrons on observed decay times exhibits a strong dependence on both the wavelength of the observing radar and the initial electron line density of the meteor trail. Meteor trails with initial electron line densities in excess of about 10^{13} electrons m^{-1} do not exhibit significant changes to echo decay times. For trails with $q < 10^{12}$ electrons m^{-1}, the effect of the loss of free electrons to absorbing particles was strongly dependent on the wavelength of the observing radar. Significant changes

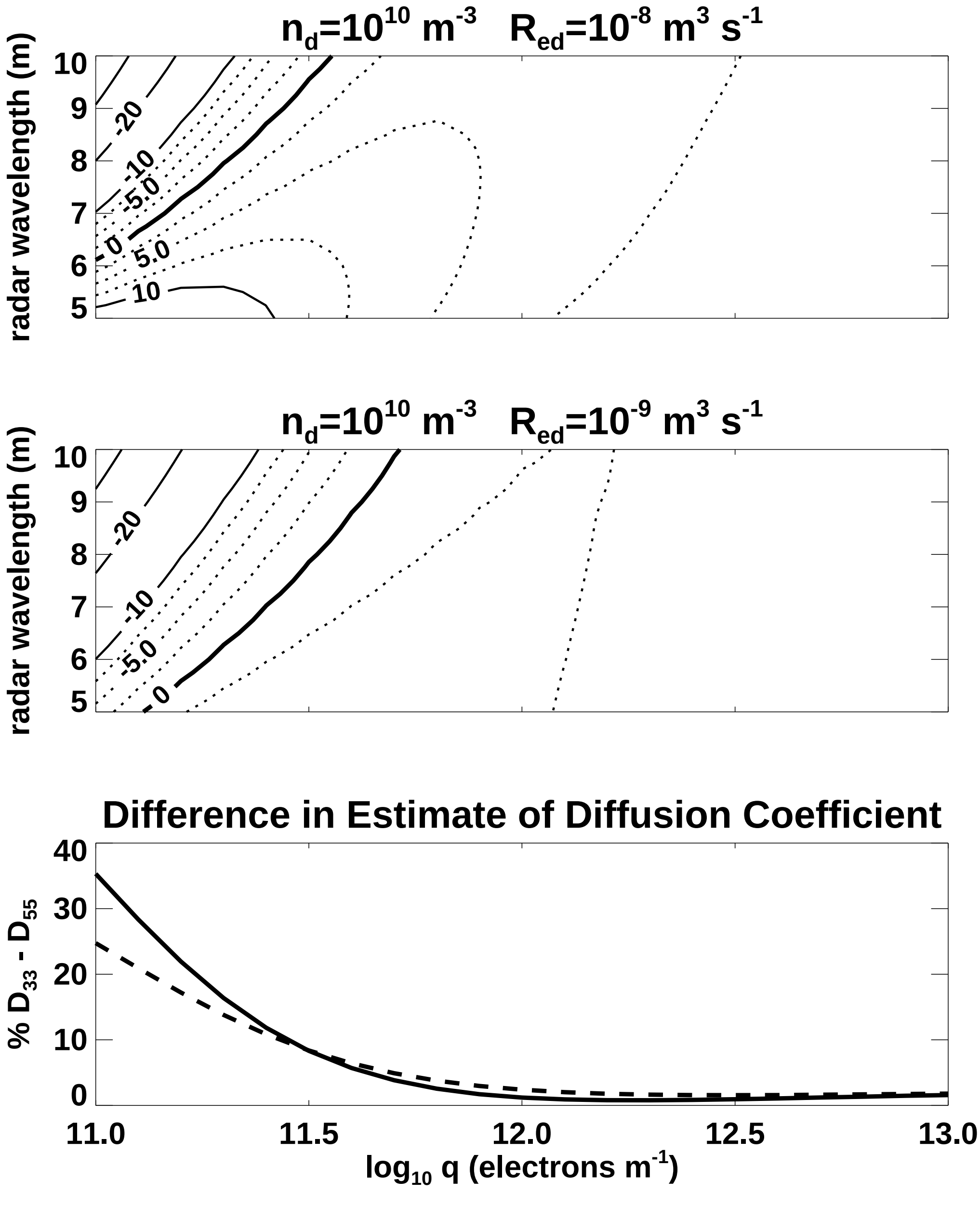

Figure 6.6: Top and center: Numerical simulation results showing percentage reduction in decay time for different absorbing aerosol regimes. Solid contours are 10% apart, dotted contours are 2.5% apart. Bottom: Percentage difference in diffusion coefficient estimates for 33 and 55 MHz radars for $n_d = 10^{10}$ m^{-3}, $R_{ed} = 10^{-8}$ m^3 s^{-1} (solid) and $n_d = 10^{10}$ m^{-3}, $R_{ed} = 10^{-9}$ m^3 s^{-1} (dashed).

to echo decay times were not predicted for aerosol densities less than about 10^{10} m^{-3} or capture rates less than about 10^{-9} m^3 s^{-1}.

Overall, the numerical simulations predict that low electron density meteor decay times for larger wavelength radars will be extended relative to those measured with short wavelengths. Shorter wavelengths may experience a reduction in decay time for some electron densities and aerosol configurations, but a comparison of the relative effect implies that higher wavelengths will be more affected. The result of the wavelength-specific modification of decay times for low density trails will result in differing diffusion coefficient estimates between radars with different wavelengths.

Large wavelength radars will produce higher estimates of the diffusion coefficient for low density meteor trails than those deduced for radars with short wavelengths that are observing the same trail, as is shown in the bottom panel of figure 6.6. The comparison of the predicted decay time reductions illustrated in the top panels of figure 6.6, suggests that radars with wavelengths of 6-7 m are least affected by the absorption of trail electrons by aerosols over a range of possible absorption regimes.

The precise effect on the decay times observed by a particular wavelength were dependent on the initial conditions of the absorbing particles and the exact electron density of the trail. The model predicts that absorption can reduce the echo decay time, as well as extending it in certain cases. The extension of echo decay times may seem counterintuitive in that a loss of scattering electrons is actually producing an increase in backscattered signal power. This occurrence can be explained in a similar manner to that of the case of complex trail chemistry described in subsection 6.1.3.

A snapshot of absorption during the diffusion process is shown in figure 6.7. It shows the free electron and the absorbing dust density at the e^{-1} decay time for a 55 MHz radar (about 0.06 s for the atmospheric parameters described). Absorption is strongest where the product $n_e n_d R_{ed}$ is maximum, which is initially at the center of the trail. The absorbing aerosol particles near the trail axis rapidly saturate, leaving no available absorbers near the axis. This produces a strong gradient in the available absorber density, n_d, that continues to move further out from the trail as more of the

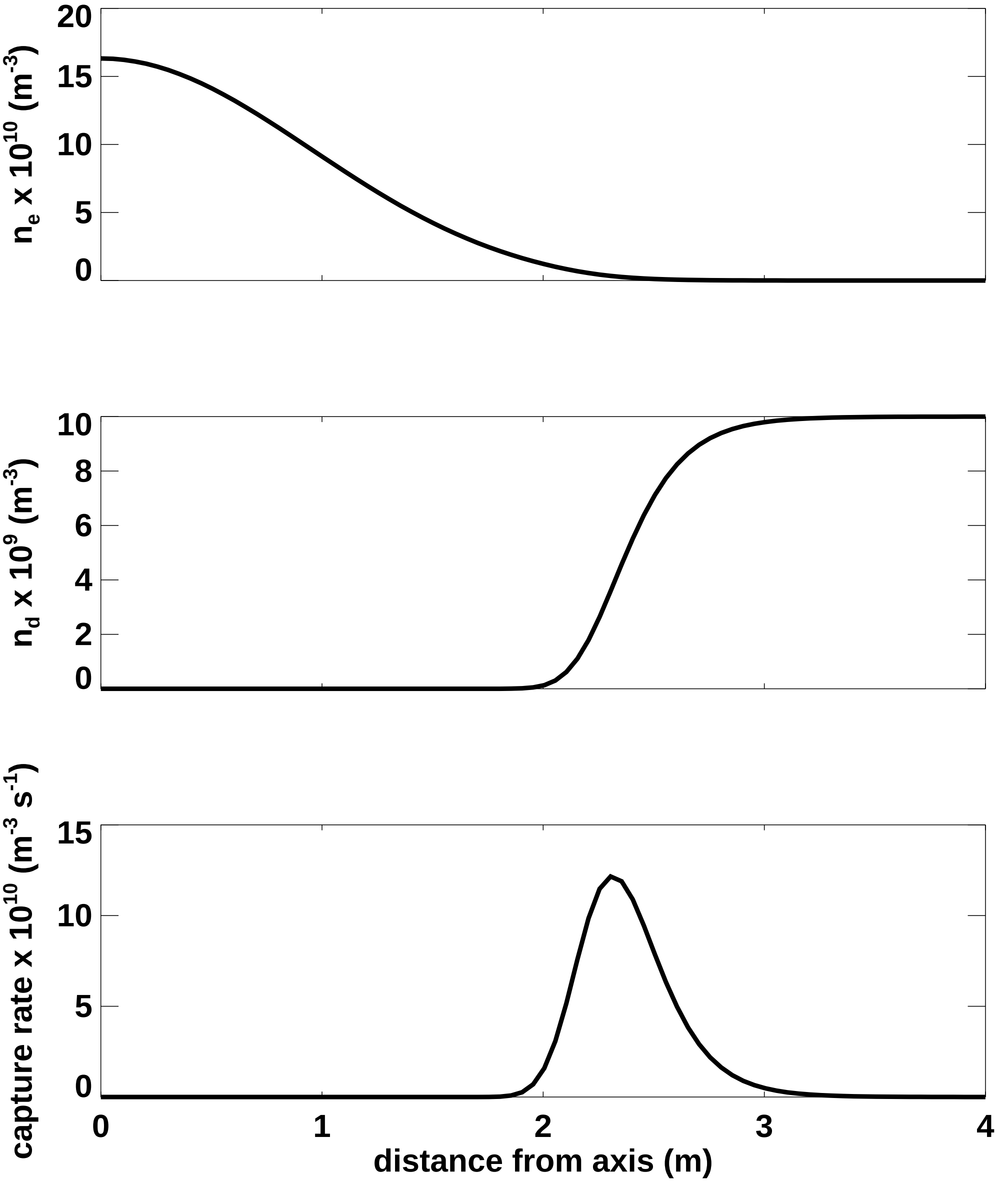

Figure 6.7: Predicted electron density (top), available absorber density (middle), and instantaneous electron capture rate (bottom) at the e^{-1} decay time for a 5.5 m radar. Atmospheric and meteor conditions are typical values for around 90 km of $D = 3.4$ m^2 s^{-1} and $r_0 = 1$ m.

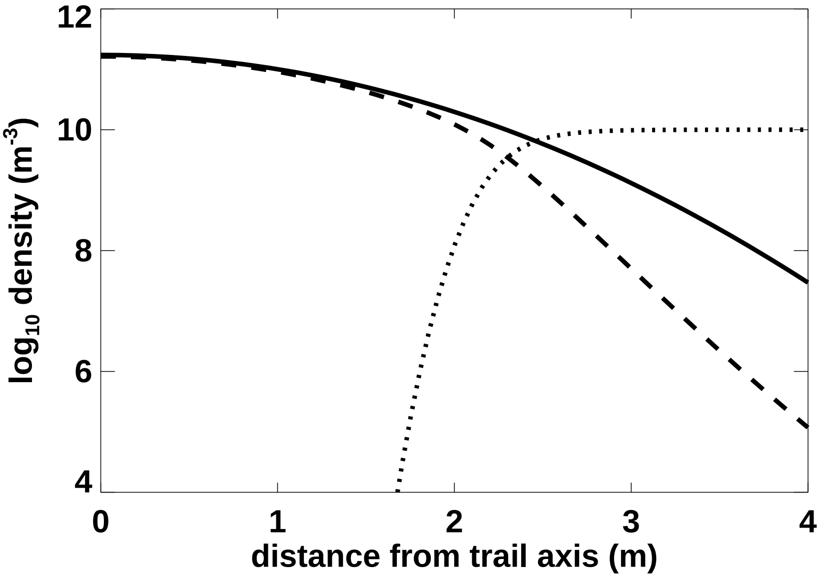

Figure 6.8: Comparison of the densities after 0.06 s of free electrons with diffusion only (solid), free electrons with absorption (dashed), and absorbers (dotted) for the absorptive case. Atmospheric and meteor conditions are typical values for around 90 km of $D = 3.4$ m^2 s^{-1} and $r_0 = 1$ m.

absorbing particles capture electrons from the trail.

Electrons diffusing out from the center of the trail are unaffected until they encounter the 'wall' of available absorber density, at which point they are captured and removed from the diffusion and scattering processes. As the density of electrons decreases significantly at the periphery of the trail, there occurs a point at which absorbing aerosols overwhelm the free electrons. A steep gradient then forms in the electron density at the outer edge of the trail, where active absorption is occurring, which is illustrated in figure 6.8.

When free electrons are absorbed from a meteor trail, the effect on the observed backscatter depends on the distance from the trail axis where the absorption occurs. If electrons are lost from the center of the trail, where the Bessel function is positive, the backscattered amplitude will be reduced. If electrons are absorbed further from the axis, they may be removed from an area where the contribution to echo amplitude is negative. In this case, the removal of electrons will result in an overall increase to the positive component of the integration used by equation 5.20 to determine the backscatter amplitude.

6.3 Comparison with observations

Figure 6.9 illustrates the difference observed between weak and strong echoes. The upper two panels show the percentage difference in diffusion coefficient estimates of echoes in the highest and lowest quartile of estimated electron density. Over the course of 2009, echoes in the 80-90 km region displayed a mean difference of 10.6% between the diffusion coefficient estmate made by the 33 and 55 MHz radars. Meteor detections with 25% lowest estimated electron density had an average difference in diffusion coefficient estimates of 15.2%. For strong echoes, this was reduced to an average deviation between estimates from the two radar frequencies of 6.1%. The deviations for the different quartiles did not change significantly over time.

Absent from the results shown in figure 6.9 is any clear seasonal trend. This seems to imply that solar modulation of meteoric smoke particle charge and the presence of polar mesospheric ice [Knappmiller et al., 2011] do not significantly change the wavelength dependence of diffusion coefficient estimates. The reason for the lack of seasonal effects remains unclear and will need to be addressed in future work.

Simultaneous detections of meteors made by co-located 33 and 55 MHz radars at Davis Station, Antarctica were used to search for differences in the diffusion coefficient estimates as a function of electron line density. An approximate estimate of the electron line density was constructed from the observed power of the echoes. Equation 5.7 can be rearranged to provide the relation

$$q \propto \left(P_R R_0^3\right)^{1/2} / \alpha_v \tag{6.8}$$

for a particular radar configuration and direction. The pulse bias attenuation term, α_d, can be neglected at lower altitudes, as it is close to unity when the echo decay time is much greater than the pulse repetition interval of the radars.

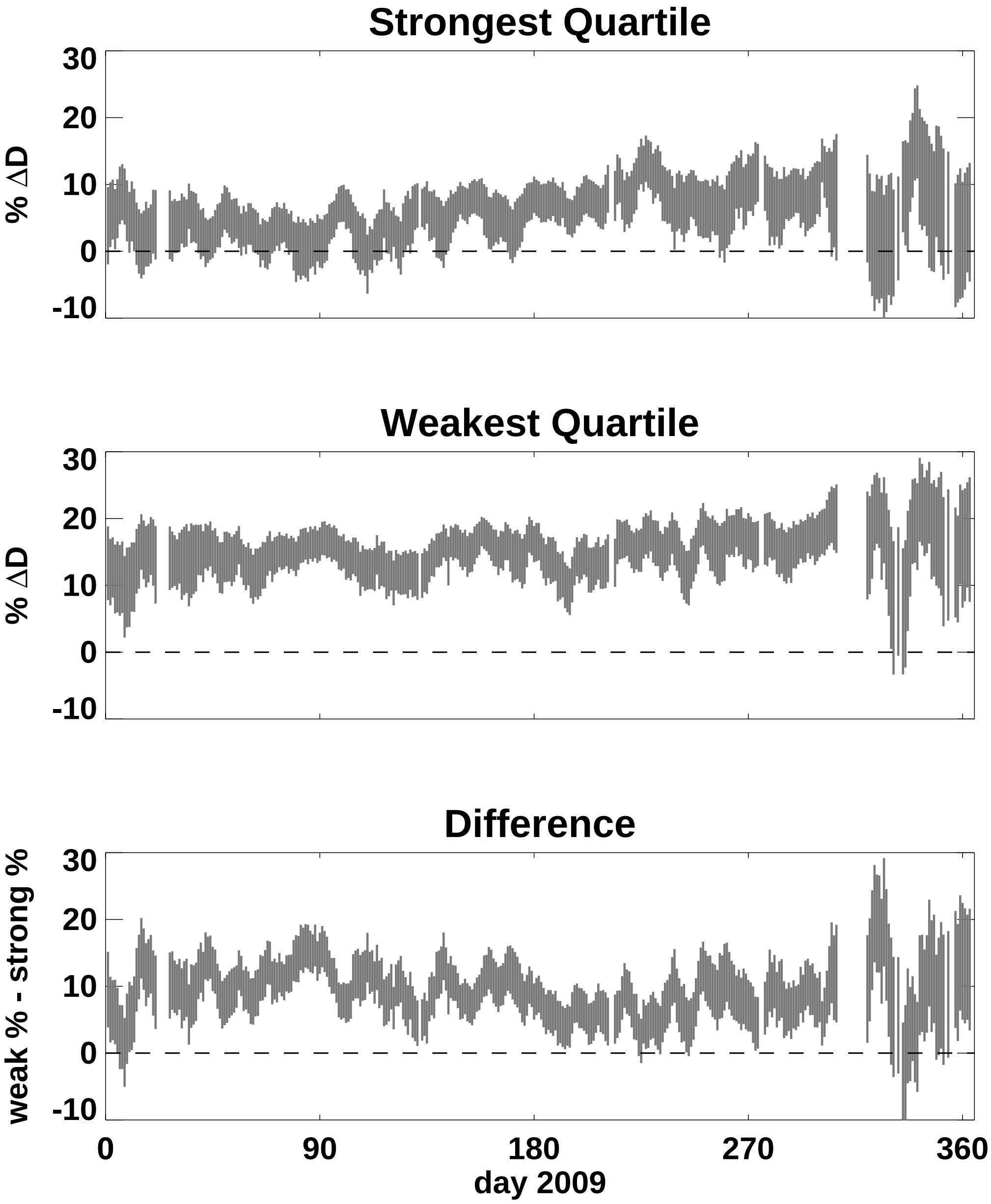

Figure 6.9: Comparison of the daily (7-day running mean) percentage difference in estimates of D made by co-located 33 and 55 MHz meteor radars at Davis Station, Antarctica during 2009 for meteors detected at 80-90 km. Vertical bars indicate 95% confidence interval.

The constant of proportionality is dependent on the wavelength of the radar, which is known, and several radar performance parameters, which are not known for the Davis Station radars. The right hand side of equation 6.8 was used as a proxy for q to determine the dependence of the diffusion coefficient estimate disagreement on electron density. The dependence of the received power on the gain pattern of the array was minimized by restricting meteors to a range of $40 - 60^{\circ}$ zenith angle.

The overall relation between electron line density and the deviation between the diffusion coefficient estimates of radars with different wavelengths is illustrated in figure 6.10. There is a clear correspondence between increasing trail electron density and decreasing disagreement between the 33 and 55 MHz radars. A comparison of figures 6.10 and the bottom panel of figure 6.6 shows a clear similarity in behavior of the simulations and observations. While this alone is not conclusive proof of aerosol absorption being responsible for the discrepancy in multi-frequency observations, it shows that the observed deviations are consistent with the results of the numerical modeling.

6.4 Summary

The use of meteor echo decay times to estimate the ambipolar diffusion coefficient relies on linear diffusion being the sole process responsible to trail evolution. In the event that the diffusion coefficient is not uniform across the width of the trail or scattering electrons are being lost from the trail, this assumption breaks down. Effects of non-linear diffusion should manifest as a discrepancy between the diffusion coefficient estimates for individual meteors as determined by radars with different wavelengths. This chapter has examined two possible mechanisms for non-linear diffusion in meteor trails and compared the predictions of numerical simulations of each case with observations.

If a meteor trail consists of more than one type of ion, diffusion will be non-linear, due to the dependence of ionic mobility on the reduced mass of the ions and background

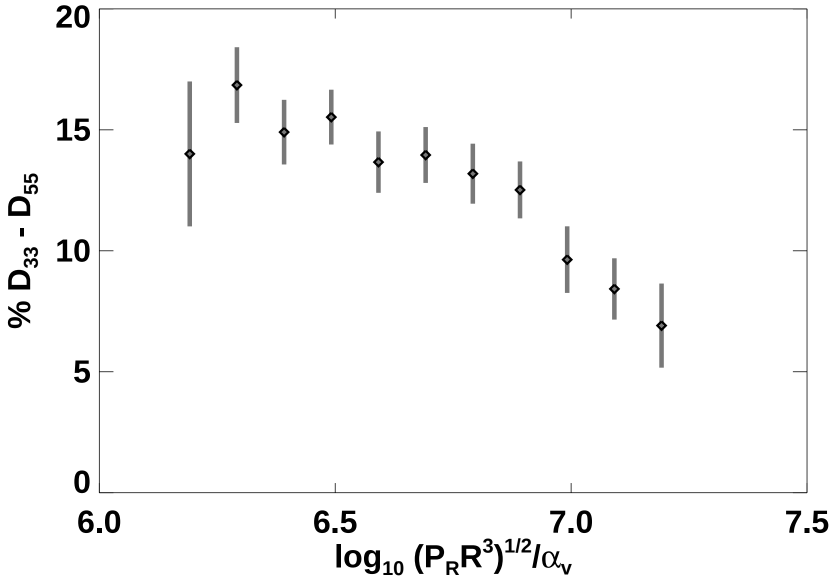

Figure 6.10: Difference in 55 and 33 MHz estimates of D as a function of estimated trail electron line density (see text for details) for simultaneous detections made by co-located radars at Davis Station, Antarctica during 2009 for meteors detected at 80-90 km. Vertical bars indicate 95% confidence interval.

gas. This is further complicated in that the initial distributions of ions may differ in size, due to a similar dependence of the initial radius on reduced mass. The presence of free electrons in the trail serves to moderate the differential diffusion of different ion species to an extent, but does not altogether prevent lighter ions from diffusing more quickly than heavy ions.

Numerical simulations showed that meteor trails with multiple species of ions sharing a common initial distribution are not significantly affected by differential diffusion, although in the later stages, gradients in the diffusion coefficient will form across the trail radius. Meteor trails where the different ion species each have an individual initial radius show a wavelength-dependent variation in the decay time as compared to linear diffusion with an average value of the diffusion coefficient. It was predicted that, under these conditions, smaller wavelengths will produce larger estimates of the diffusion coefficient than large wavelengths. This effect becomes more pronounced for trail compositions with greater differences in ion mass and closer to equal quantities of light and heavy ions.

Background aerosols in the form of dust particles or small ice crystals can absorb electrons from meteor trails, altering their scattering properties. The absorption of scattering electrons can extend or reduce the decay times of meteor echoes with increasing severity for trails with lower initial electron line density. The magnitude and direction of the decay time reduction also depends on the wavelength of the observing radar.

The effects of non-linear diffusion are apparent in the comparison of diffusion coefficient estimates made by different frequency radars observing the same meteors. In the case of differential diffusion of multiple ion species with individual initial radii, simulations predict that small wavelengths will produce diffusion coefficient estimates that are larger than those of large wavelengths by about $5 - 15\%$. For the case of aerosol absorption, the opposite is predicted. Aerosol absorption is predicted to cause deviations in the diffusion coefficient estimate between different wavelengths of up to 35%, depending on aerosol parameters and meteor trail line density. Furthermore, aersol absorption should cause a detectable dependence of the deviation between two radar's estimates on trail electron line density, which can be inferred from echo power.

Co-located 33 and 55 MHz radars at Davis Station, Antarctica provided data for comparison with the numerical simulations in the form of 224,971 meteor detections that were simultaneously observed by both radars. It was found that at all altitudes and times of year that the 33 MHz radar provided systematically higher estimates of the ambipolar diffusion coefficient. The magnitude of the discrepancy showed a clear dependence of the estimate on trail electron line density, which was also predicted by the numerical simulations of aerosol absorption during diffusion.

The comparison of the numerical simulations and observational data indicates that aerosol absorption is the primary mechanism responsible for deviations in the estimate of diffusion coefficient by radars with different operating frequencies. The predicted and observed effect is several times larger and of opposite sign than was predicted for differential diffusion. The latter may still occur in meteor trails, but the effect on anomalous decay times is outweighed by the effect of absorbing aerosols. The effect of absorption is diminished for meteor trails with high initial electron densities, indicating that it may be mitigated by restricting diffusion coefficient estimate data to those made for strongly scattering meteors.

Chapter 7

Meteor Shower Detection

The previous chapters have focused on the use of meteor radar as an atmospheric sensor. While this role occupies the bulk of efforts in the field, an obvious application of any meteor detection system is that of astronomy. Of particular interest is searching for meteor showers, which result when narrow filaments of debris have orbits that intersect the orbit of Earth.

This chapter will outline the methods used for detecting meteor showers with single station radars. The results of a two-year survey will be presented, including the orbital parameters of detected showers.

The position of a meteor shower is the radiant, so-called because meteors from the shower appear to radiate out from that point when viewed from the ground. This is due to the parallel trajectories of meteoroids in a stream large enough to completely encompass the viewer. When facing the direction of the incoming meteors, perspective produces the illusion that the paths originate from a single point.

It is helpful to review the coordinate systems used to describe different types of observations. Visual and radar detections of meteors are usually described using the horizontal coordinate system, which expresses a position in the sky in terms of azimuth from North and elevation from the horizon. This coordinate system is most useful for geophysical studies, as it describes the positions of meteors relative to fixed points on the surface of Earth.

Meteor shower radiants are usually described using the equatorial system, which provides a map of the celestial sphere that is not attached to any point on the surface of the Earth. The latitude term, declination, describes the angular displacement from the plane extending through Earth's equator. Right ascension, the expression of longitude, is measured from the direction to the Sun at the March equinox. Unless otherwise stated, coordinates of meteor shower radiants in this study are expressed in equatorial coordinates.

Single station interferometric meteor radars are designed primarily to observe the behavior of the atmosphere by measuring the radial component of the wind field and the diffusion-based decay time of underdense meteors. The underdense meteor provides coherent backscatter that decays in a predictable manner over time, but the specular reflection condition does not allow the trajectory of individual meteors to be directly ascertained. Instead, the directional information for the path of each meteor is limited to a plane of ambiguity perpendicular to the line of sight from the radar.

This limitation can be overcome with the use of additional receiving interferometers located away from the transmitter. The path of each meteor can then be reconstructed from the intersection of the planes of ambiguity produced by each receiver group. Alternatively, single outlying receiving antennas can provide time-of-flight information to reconstruct the trajectory of the meteoroid. The multi-static receiver approach has been used with considerable success by the Advanced Meteor Orbit Radar facility in New Zealand [Baggaley et al., 1994] and, more recently, the Canadian Meteor Orbit Radar in Canada [Jones et al., 2005].

Multi-station radars have the advantage of being able to completely resolve the trajectories of individual meteors detected simultaneously at multiple locations, but this comes at the price of reduced field-of-view. Trajectories of individual meteors require detections in the region defined by overlapping fields-of-view of different receiving antenna groups, which will be only a portion of the field of view for a single all-sky system. Furthermore, the simultaneous detection of a meteor by multiple receiving stations requires that the specular points for each station are located at points on the trail axis with detectable ionization. This condition can be overcome by locating the stations close together, but this results in a loss of angular resolution of the combined system.

7.1 Great circle method

Shower radiants can be extracted using single-station data by a statistical analysis. Morton and Jones [1982] present a method by which the activity of a radiant is described by the number of detections in a band perpendicular to the radiant. First, detections of meteors over a small period of time, usually one day, are translated from the horizontal coordinates of the radar to the equatorial coordinates of the celestial sphere. Detections are then counted in a band perpendicular to each possible radiant, as depicted in figure 7.1.

The number of detections perpendicular to each radiant can then be used to construct a map of the activity of all radiants on the celestial sphere. Such a method is essentially a convolution of detection density on the celestial sphere with a tophat function (the acceptance band).

Detections occurring in a great circle are perpendicular not only to the source radiant, but to the mirror of the source radiant, as well. A test for great circle concentrations does not take into account the sense of the radiant vector.

A simple test can be applied to meteors in the acceptance band to determine if they could have originated from the direction of the radiant of interest. If the radar zenith is in the same hemisphere as the radiant of interest at the time of detection, it is possible that the meteors in the acceptance band originated from the radiant of interest. If the radar zenith for a particular detection is in the opposite hemisphere from the radiant of interest, then either the meteor belongs to another radiant or is traveling up from the ground. Given the impossibility of the latter scenario, detections that occur when the radar zenith is in the opposite hemisphere from the radiant of interest can be discarded [Jones and Jones, 2006].

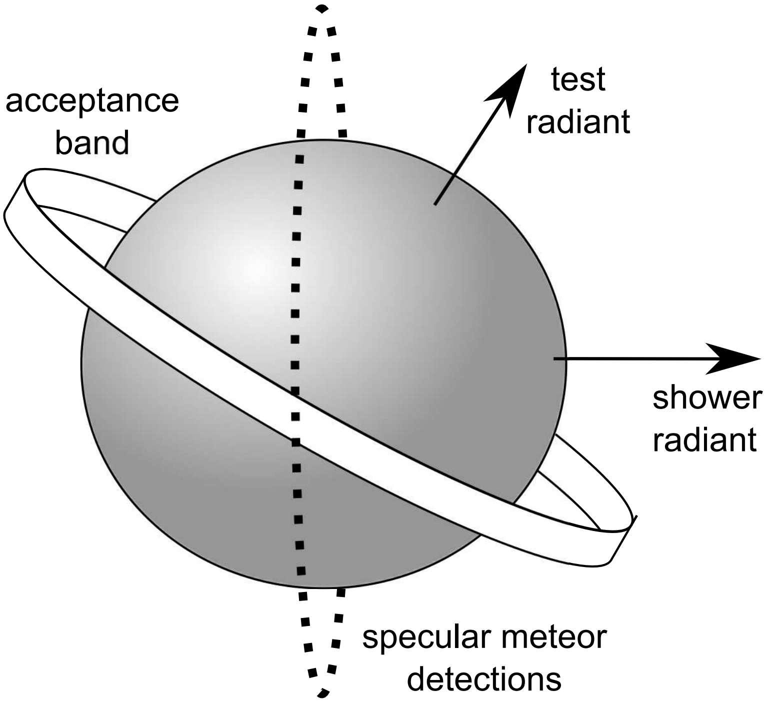

Figure 7.1: Geometry of great circle detection method, as viewed from a fixed point in equatorial coordinates. The sphere represents Earth rotating on its axis. The dotted line represents specular meteor detections from a stream approaching from the indicated direction. The white band is the acceptance band in which detections are counted for the radiant being evaluated.

7.1.1 Properties of the acceptance band

The tophat weighting function carries the advantages of simplicity and computational efficiency, as only the angular distance from the detections to the radiant of interest need to be calculated. The tophat function does, however, suffer from a significant weakness in that it will produce false radiant activity estimates around an active radiant. If the radiant of interest is offset from the active radiant, some of the detections will still lie in the acceptance band, as occurs in the example shown in figure 7.1. These detections will be falsely attributed to the radiant of interest, despite being due to an active radiant in another direction. The resultant image of the active radiant will be surrounded by a diffuse halo, potentially obscuring fine structure and merging adjacent active radiants, which can be seen in the top panel of figure 7.2.

Jones and Jones [2006] overcome the halo effect by applying a weighting function with negative rejection bands located on either side of the center of the acceptance band, given by

$$w(\theta) = \begin{cases} 1 & \text{for } |\theta| \leq \delta\theta \\ -1 & \text{for } \delta\theta > |\theta| \geq 2\delta\theta \\ 0 & \text{for } |\theta| > 2\delta\theta \end{cases} , \tag{7.1}$$

where θ is the angular separation from the center of the acceptance band. When the radiant of interest is aligned with the radiant of an actual shower, the acceptance band is aligned with the great circle of increased detection density. When the radiant of interest is offset from the active radiant, some detections will fall in the acceptance zone, but these will be canceled by negative contributions of the rejection bands to either side.

The three band method presented in equation 7.1 significantly reduces the halo effect present in images produced using a top hat weighting function, but does introduce an additional problem. Negative values can arise in the resultant radiant activity map, due to noise from sporadic background meteors. Also, a partial arc fragment of the great circle of an active radiant may occur in only one rejection band, producing an

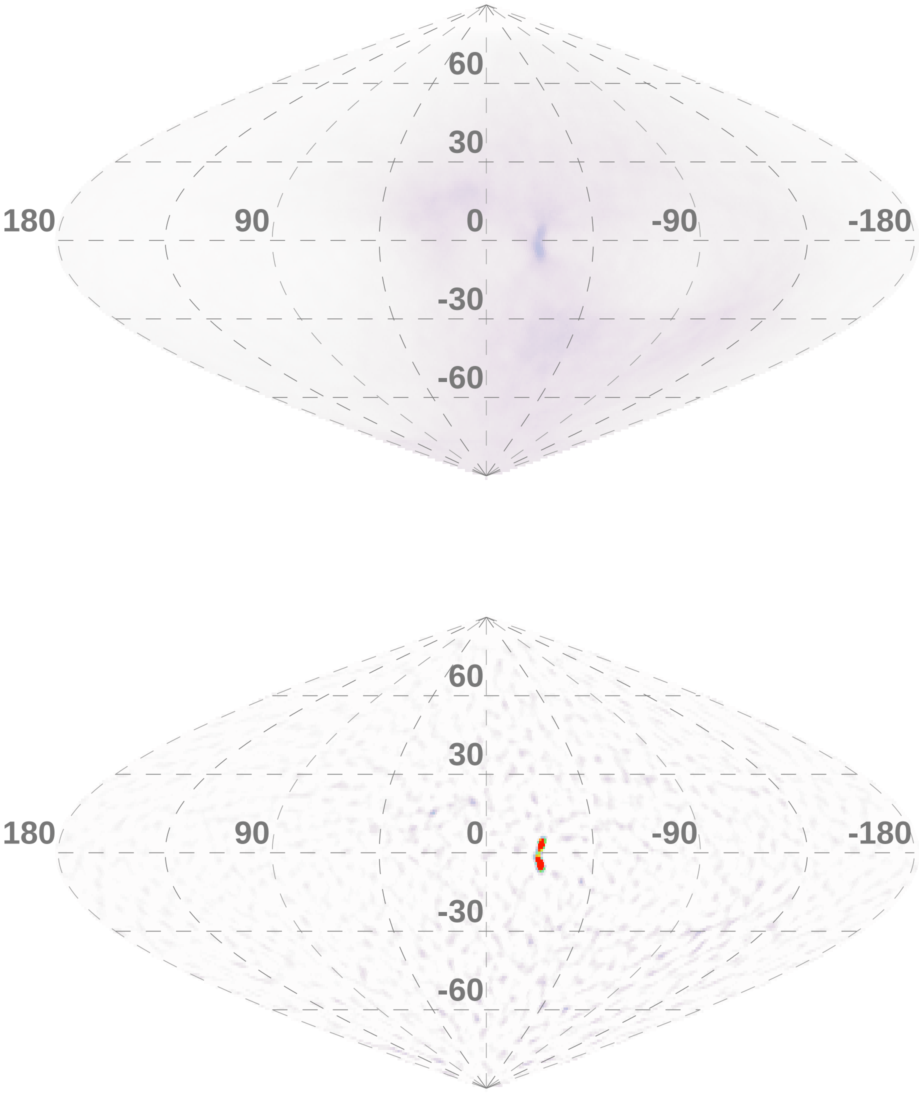

Figure 7.2: Radiant activity maps for Darwin, May 6, 2007, produced using a tophat weighting function (top) and a Jones and Jones weighting function (bottom). The two dark spots on map to the right are the η-Aquariid (below equator) and a newly discovered shower (above equator).

unphysical negative value for radiant activity. While positive values may indicate radiants with enhanced activity, negative values are an artifact of the weighting function used in the convolution. Negative values may be ignored for the purposes of shower detection, but they can provide some indication of the noise present in radiant activity estimates.

Jones and Jones [2006] improve the three-band weighting function by suggesting a polynomial weighting function given by

$$w(\theta) = \begin{cases} 1 - 6\left(\frac{\theta}{\delta\theta}\right)^2 + 5\left(\frac{\theta}{\delta\theta}\right)^4 & \text{for } |\theta| \leq \delta\theta \\ 0 & \text{for } |\theta| > \delta\theta \end{cases} . \tag{7.2}$$

This function minimizes spurious negative values, in addition to providing a narrow positive response region. The positive region of this weighting function is approximately one half of the supplied value of $\delta\theta$. The selection of an appropriate value of $\delta\theta$ depends on the accuracy of the radar being used for the survey and the size of the features being searched for. The response function of the Jones and Jones weighting function is such that the intensity profile of a point source in the resultant image will have a half-width full-maximum of approximately $\delta\theta/2$. The width of the weighting function must be chosen so that it contains all of the meteors from potential showers, as well as minimizing contamination from detections outside of the shower. In practice, 4° has been found to provide the optimal sensitivity of the method for detecting narrow showers [Holdsworth et al., 2008].

7.2 2006-2007 Meteor shower survey

The great circle method was used with the Jones and Jones weighting function described by equation 7.2 to search for meteor showers in records of detections from 2006 and 2007. The data were collected by 33 MHz radars located at Darwin, Australia and Davis Station, Antarctica. In total, the Darwin radar detected 8,800,600 meteors over 605 days of operation and the Davis Station radar detected 6,494,030 meteors during 727 days of operation. The locations of the two radars provided complete coverage of the southern hemisphere of the celestial sphere with detections at Darwin seen as far north as 50° declination.

Each data set was broken into 24-hour blocks for analysis. This is long enough to ensure a complete diurnal cycle, which will sweep the field of view of the observing radar across the maximum visible portion of the celestial sphere. It is also short enough that radiants are not blurred by the apparent radiant drift caused by the orbital motion of Earth. As Earth travels in an orbit around the Sun, the apparent radiant of a meteor shower changes as the orbital intercept angle changes. This produces a maximum drift in the radiants of meteor showers of about 1° per day.

A grid of candidate radiants to evaluate was created on the celestial sphere by first dividing the sky into latitudinal strips spaced at $\Delta\phi = 1^\circ$ of declination apart. Each strip, located at declination ϕ was then divided into equal segments of approximately 1° of arc. This produced a square grid of 41,252 approximately uniformly spaced points over the celestial sphere.

An activity map was then assembled by applying the great circle method with a 4°-wide Jones and Jones weighting function to each radiant in the assembled grid. As the weighting function modifies the count of meteors in the acceptance band, the result for each radiant is not a strict count of potential shower meteors, but rather a measure of the relative activity of the particular radiant.

The intensity of the relative activity was quantified using the signal-to-noise ratio of each particular radiant. It was found that the radiant activity map is spatially dominated by sporadic background meteors. The histogram of radiant activities produces an approximately Gaussian distribution. Background noise was defined as the activity at 2.5 widths of the Gaussian curve fit to the histogram of radiant activities. The SNR was then defined as the ratio of relative activity of the radiant of interest to the background noise estimate. It was found that a SNR of 2.0 was a sufficient threshold to indicate a possible shower, while striking a balance between the exclusion of background fluctuations and the preservation of sensitivity.

The suspected showers were manually sorted into shower systems, where the shower is present for more than one day of observation. Shower detections were deemed to be confirmed if they were members of a shower system with consistent drift in right ascension and declination, appeared at the same radiant at the same solar longitude in different years, or had a single detection with an SNR of greater than 2.5.

7.2.1 Velocity estimation

Once candidate showers were detected, an attempt was made to estimate the velocity of the shower meteors. Candidate shower meteors were selected using a 4°-wide acceptance band perpendicular to the suspected shower radiant. A histogram of the Fresnel transform velocities was then constructed using only meteors above the peak detection height. The high-altitude height discrimination was applied to remove the effects of deceleration from the velocity estimate, as the modeling described in Chapter 3 indicated that deceleration is negligible above the peak detection height.

An estimate of the background velocities was obtained from the average velocities in acceptance bands corresponding to the radiants at ±90° right ascension from the radiant of interest. This was then subtracted from the velocities of the radiant of interest to remove background contamination. A Gaussian curve was then fitted to the remaining distribution, as shown in figure 7.3. The velocity for the suspected shower was then defined as the center of the fitted curve, with the uncertainty in the estimate given by the width of the fitted curve.

7.2.2 Detected shower radiants

Using the criteria described in section 7.2, a total of 598 individual shower detections were made, shown in the top panel of figure 7.4. Of these, successful estimates of velocity were made for 522. Each shower detection represents the confirmed detection of a shower system during a 24-hour period at one location. When grouped into shower systems, it was found that the detected showers comprised 37 shower systems, summarized in the bottom panel of figure 7.4.

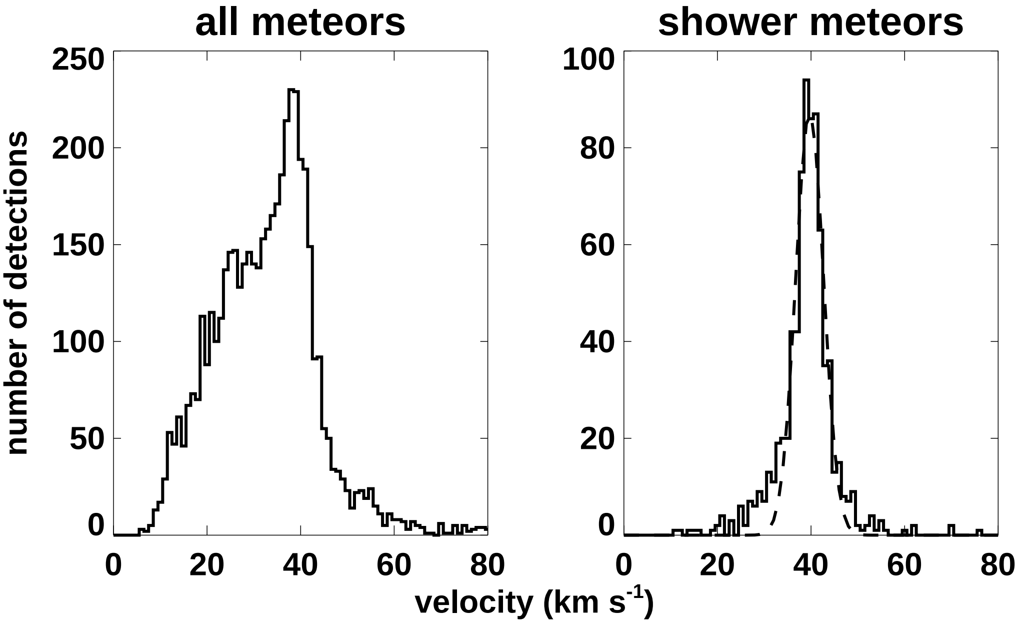

Figure 7.3: Distribution of velocities for all meteors (left) and Southern δ-Aquariid meteors (right) that were detected at Davis Station, Antarctica on July 29, 2007.

The identification of the detected shower systems presented a challenge, as there is no single authoritative catalog of known meteor showers. As such, a number of different sources were combined to assist in the identification of the detected shower systems.

The International Astronomical Union maintains a list of officially recognized showers [IAU], but the data are limited to single values of right ascension and declination and the velocity. The austerity of this information complicates the identification of persistent showers that occur over a number of days with gradually shifting locations. Listed showers in this catalog are evaluated by a panel with assistance from the International Meteor Organization for confirmation.

The International Meteor Organization, a network of professional and amateur meteor observers, publishes an annual calendar of expected meteor shower activity [International Meteor Organization, 2007]. Primarily geared towards the visual observer, it provides a more detailed description of individual showers than the IAU

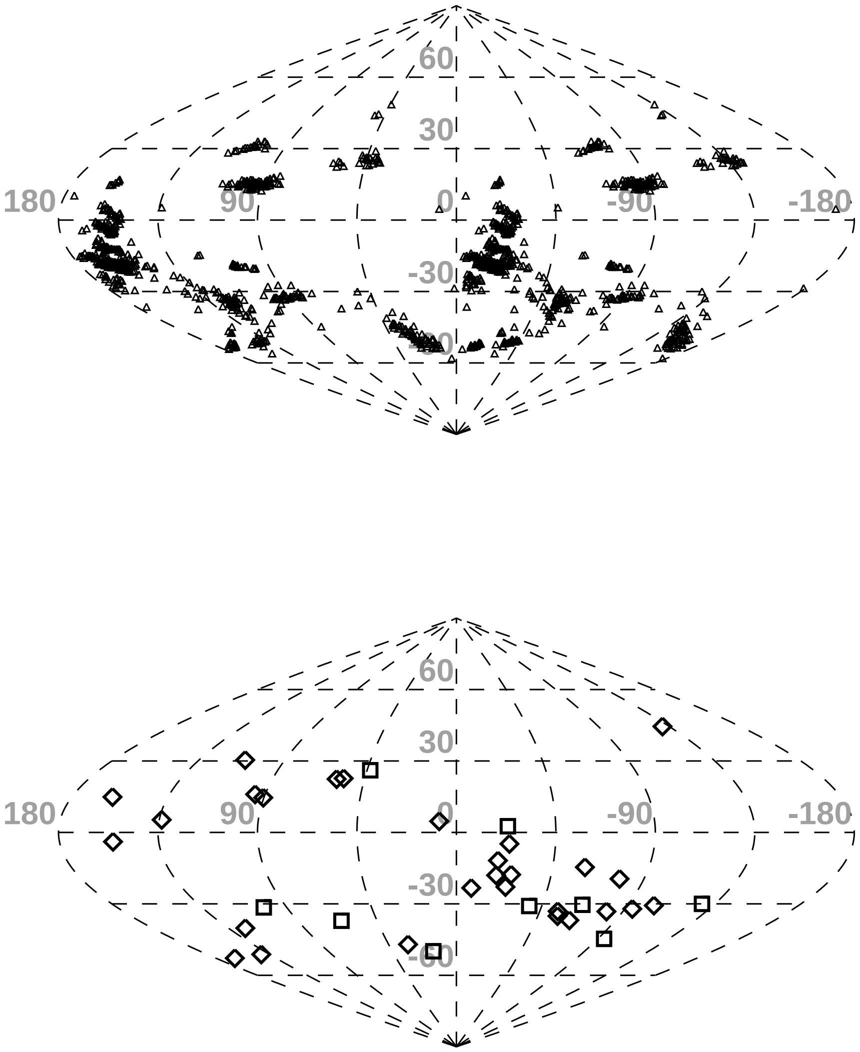

Figure 7.4: Top: All meteor showers detected at Darwin, Australia and Davis Station, Antarctica during 2006-2007. Bottom: Shower systems on date of peak activity. Diamonds are previously cataloged showers and boxes are new discoveries.

database, including radiant locations at 5 day intervals across the year, which are useful for identifying long-lasting showers whose radiants drift over the sky throughout their duration. A limited list of daytime showers is provided, having been obtained predominantly by observations using passive forward scatter radio techniques, but otherwise the showers listed in the annual calendars are the result of collated visual observations.

Several published articles contain useful summaries of recurrent shower activity. An often referenced work [Cook, 1973] summarizes a number of different visual and early radar surveys into a concise list of radiants, and includes orbital data where possible. Brown et al. [2008] published a summary of showers detected using the Canadian Meteor Orbit Radar during the 2002-2006 period, although the data is necessarily restricted to showers visible in the northern hemisphere. This paper does however have the benefit of having been produced using high precision radar data, which includes a number of daytime showers not present in visual observations. Jenniskens [1994] analyzed the results of a network of visual observers in Australia and the Netherlands who operated over the ten year period 1981-1991. This paper includes observations from the oft-overlooked southern hemisphere and provides orbital data for select showers.

One of the most detailed resources is the online database Meteor Showers Online [Kronk]. Comprising both an annual calendar and detailed descriptions of individual showers, this online database is based on the content of a previously published book [Kronk, 1988], which has been placed online and updated as new observations are made. The current status of showers is given, along with histories of observations and orbital data if reliable velocities are available.

The identities of the showers detected in this survey and summaries of their attributes are shown in table 7.1. Velocity estimates were successfully made for all of the shower systems, with the exception of the σ-Hydrids, which were only seen in one day during 2007 of the Darwin data, and then only at the lower bound of the SNR cutoff. The Darwin radar was not operating on the day of occurrence during 2006.

Of the 37 distinct shower systems detected, 9 were not present in the catalogs used

shower name	first date	last date	peak $\lambda_\odot$	peak R.A.	peak dec.	v km s^{-1}	Δv km s^{-1}
α Piscis Australids (B)	Jul-24	Jul-29	120.9	335.9	-22.9	39.8	4.2
α Puppids* (B)	Jan-6	Dec-30	276.3	140.9	-51.2	40.2	5.8
Day χ Sagittariids* (B)	Jan-2	Jan-11	286.7	281.7	-19.5	26.4	3.4
Day κ Leonids* (A)	Sep-22	Sep-28	174.0	161.0	14.9	40.0	5.9
Day Sagittariids Capricorinids* (B)	Jan-9	Feb-21	299.2	305.3	-33.1	25.6	3.0
η Aquariids* (A, B)	Apr-29	May-14	39.8	335.9	-4.8	60.6	7.9
η Carinids (B)	Jan-4	Jan-15	288.0	165.8	-52.8	37.7	4.9
Geminids (A)	Dec-2	Dec-13	261.0	110.8	30.4	35.1	2.1
July Phoenecids (A, B)	Jul-4	Jul-21	107.8	32.1	-47.0	39.2	4.3
Northern δ Aquariids (A)	Jul-23	Jul-31	117.3	334.0	-17.7	40.7	4.1
Northern Taurids (A)	Nov-8	Nov-8	225.8	55.3	22.7	29.2	2.3
November Orionids (A)	Nov-22	Dec-4	245.8	90.3	14.6	41.7	4.8
Orionids (A)	Oct-15	Oct-31	207.9	94.7	16.0	60.5	9.3
ϕ Sagittariids (B)	Jun-5	Jun-25	88.5	278.9	-33.2	26.8	3.6
Piscis Austrinids (A, B)	Jul-25	Aug-14	126.9	352.7	-23.3	38.7	5.2
Quadrantids* (A)	Jan-3	Jan-4	282.9	229.3	44.5	40.9	3.0
Sagittariids (A, B)	Jun-8	Jun-13	75.1	304.1	-35.1	36.4	3.6
Sextantids* (A, B)	Sep-26	Oct-4	188.1	155.7	-3.9	32.7	2.7
σ Hydrids (A)	Nov-12	Nov-12	229.6	133.9	5.3	-	-
Southern δ Aquariids (A, B)	Jul-17	Aug-14	120.9	341.1	-18.0	39.2	3.9
Southern ι Aquariids (A)	Jul-23	Aug-7	121.9	340.8	-11.8	40.1	3.7
Southern June Aquilids (B)	Jun-13	Jun-13	77.0	296.1	-36.9	34.5	7.2
Southern May Ophiuchids (B)	May-24	May-24	58.1	256.1	-30.7	28.5	6.8
Southern Piscids (A)	Sep-10	Sep-10	162.3	7.8	4.7	32.2	6.6
τ Capricorinids (B)	Jul-17	Jul-19	109.4	299.9	-14.6	27.6	4.8
θ Ophiuchids (A, B)	Jun-2	Jun-21	74.4	266.1	-32.1	27.5	4.2
ζ Perseids* (A)	Jun-3	Jun-15	67.4	58.6	22.4	31.4	7.1
ζ Puppids* (B)	Nov-3	Nov-6	222.8	125.0	-40.2	35.8	4.6
Unknown 1* (B)	Jan-14	Jan-18	297.9	293.9	-30.4	26.1	4.3
Unknown 2* (B)	Feb-6	Feb-9	319.5	231.7	-30.0	54.8	10.8
Unknown 3* (A)	Mar-19	Mar-31	358.7	266.0	-44.7	57.4	8.1
Unknown 4* (B)	Apr-29	Apr-30	34.7	16.2	-49.9	42.9	3.0
Unknown 5* (A)	Apr-29	May-14	40.5	336.7	2.6	60.3	8.6
Unknown 6* (A)	Jun-10	Jun-19	75.1	43.4	26.1	39.6	4.4
Unknown 7 (B)	Jul-1	Jul-10	102.1	321.6	-30.9	35.2	5.2
Unknown 8 (B)	Sep-9	Sep-9	161.6	65.2	-37.1	38.3	9.6
Unknown 9* (B)	Oct-8	Oct-21	198.9	102.2	-31.5	35.6	5.9

Table 7.1: Meteor showers detected at Darwin, Australia (A) and Davis Station, Antarctica (B) during 2006-2007. Daytime showers are indicated by *. Velocities are as estimated on the date of maximum activity. (Originally published in Younger et al. [2009])

for identification. One of the new discoveries was previously described by Holdsworth et al. [2008], who used some of the same detection data. The high rate of discovery ($\approx 24\%$) is primarily due to two factors relating to the use of radar as a detection method and the high angular resolution of the great circle implemented with a Jones and Jones type weighting function.

Historically, meteor showers have usually been detected by visual or photographic means. As such, meteor shower catalogs are dominated by showers occurring at night. For this study, daytime showers were defined as those with radiants within $\pm 90^\circ$ of the Sun and are indicated in table 7.1. Out of the 37 shower systems listed, 14 occur during daylight hours, including 7 out of the 9 new discoveries.

The angular resolution of the great circle method with a Jones and Jones method allows closely spaced showers to be distinguished. Such is the case with the η Aquariids and Unknown 7, which can be seen on the radiant map shown in figure 7.2. The similar location and velocity indicate that Unknown 7 is likely a sub-filament of the η Aquariid stream. The resolution of the method also allowed shower complexes, where multiple shower systems appear close together, to be studied. Particularly dense is the δ Aquariid complex occurring in July/August, which consists of the α Piscis Australids, Northern δ Aquariids, Piscis Austrinids, Southern δ Aquariids, Southern ι Aquariids, and τ Capricorinids.

7.2.3 Uncertainty in the velocity estimate

The uncertainties in the velocity estimates for detected showers provides an opportunity to empirically assess the precision of the Fresnel transform velocity measurement technique. Shower meteors are produced by debris in narrow filaments. All of the objects in the stream share a common orbit and thus have the same velocity. The rotation of Earth produces a maximum fluctuation in relative velocity of ± 0.46 km s^{-1} at the equator. Deceleration will introduce some variation to the observed velocities, but the height discrimination described in section 7.2.1 removes most of this effect. Any additional spread in observed velocities of shower meteors is then due to

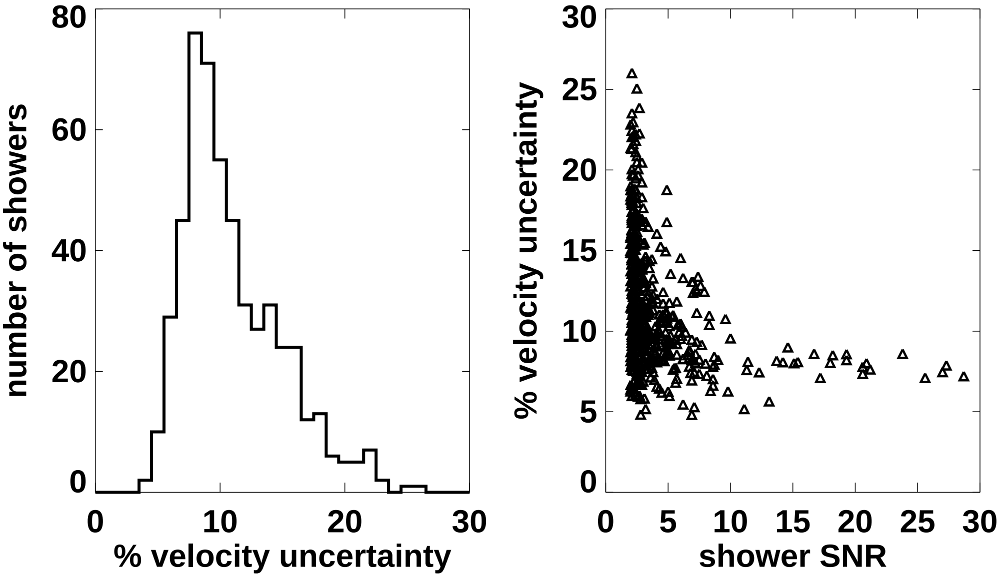

Figure 7.5: Left: distribution of relative uncertainty in meteor shower velocity estimates. Right: meteor shower velocity estimate uncertainty as a function of shower intensity.

uncertainty in the velocity measurement technique.

A distribution of velocity uncertainties, shown in the left panel of figure 7.5, was assembled from the uncertainty in the velocity estimates for all detected showers with successful velocity estimates. It was found that the relative uncertainty in the velocity estimate for most showers lies in the $5 - 10\%$ range, which is consistent with the findings of Holdsworth et al. [2007].

A further examination showed that the scatter in uncertainties was dependent on the SNR of the particular shower, as seen in the right panel of figure 7.5. Relative uncertainties in the velocity estimate above 10% were only seen for SNR$<$ 10, with uncertainties above 15% only occurring for showers with SNR$<$ 5. At high SNR values, the relative uncertainty in the velocity estimate appears to converge towards $\approx 8\%$.

7.3 Stream orbits

Meteor showers occur when the orbits of debris in narrow filaments intersect the orbit of the Earth. If the direction and velocity of the shower meteors is known, the orbit of the debris stream responsible for the shower can be determined. The results of the survey presented in section 7.2 provide an opportunity to determine the orbital elements of a number of showers, which will assist in describing the distribution of materials in Earth-intercepting orbits.

7.3.1 Orbital elements

Five quantities, shown in figure 7.6, allow the orbital trajectory of an object about a central focus to be fully specified. The eccentricity, e, and length of the semi-major axis, a, describe the size of an elliptical orbit. Three angles, comprised of the inclination from the ecliptic plane, i, the argument of the ascending node, Ω, and the argument of the perihelion from the ascending node, ω, specify the orientation of the orbit.

The ascending node is defined as the point at which the orbit crosses from below to above the ecliptic plane. The upper hemisphere of the ecliptic plane is defined as the side that contains the North pole of Earth. Using the the direction of the radiant and the relative velocity of detected showers, it is possible to calculate these terms for the parent streams of each shower.

Two terms are immediately known. The inclination of the orbit is the angular separation between the shower radiant and the ecpliptic plane. The argument of the ascending node is the argument of the orbit of Earth at the time of detection for showers with radiants below the ecliptic plane, or 180° added to the argument of Earth's orbit if the shower is detected at the descending node. Also needed to calculate the remaining terms is the distance from the Sun, r, which is simply the distance from Earth to the Sun at the time of detection.

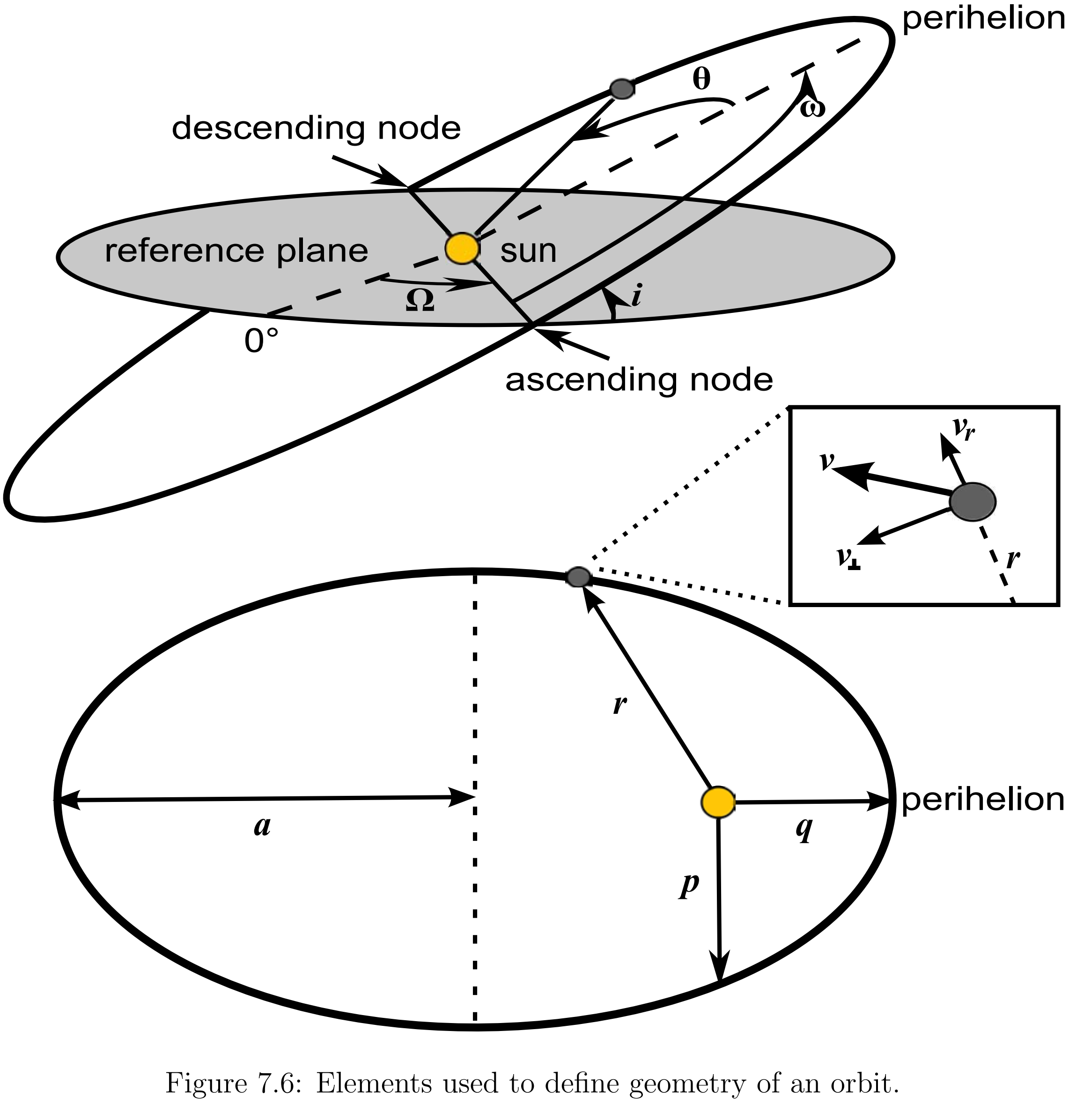

Figure 7.6: Elements used to define geometry of an orbit.

7.3.2 Infall effects

Before the orbital elements of a particular meteor shower can be calculated, the effects of the interaction with the gravitational field of Earth must be accounted for. Two sources of error occur due to the acceleration of meteors during the Earth infall process, acceleration and zenith attraction, the effects of which are demonstrated in figure 7.7. As meteoroids approach Earth, they are accelerated by gravity. For a body with initial orbital velocity v_∞, the velocity at atmospheric entry, v_a, is related to the initial velocity by

$$v_\infty = \sqrt{v_a^2 - \frac{2GM_\oplus}{r_a}}, \tag{7.3}$$

where G is the gravitational constant, $M_\oplus$ is the mass of Earth and r_a is the distance from Earth's center of mass at atmospheric entry, that is the radius of Earth added to the geometric height of the meteor at detection).

Zenith attraction is the result of the change in direction of a meteor due to gravitational attraction, which causes the path of falling objects to approach the normal to the local gravity equipotential surface. For an initial velocity, v_∞, and an atmospheric entry speed, v_a, the deviation from the original zenith angle ϕ is given by

$$\Delta\phi = 2\tan^{-1}\left(\frac{v_a - v_\infty}{v_a + v_\infty}\tan\frac{\phi}{2}\right). \tag{7.4}$$

The effect of zenith attraction varies throughout the detection of a shower, as the rotation of Earth changes the zenith angle of incoming meteors. This manifests in the radiant activity map as a broadening of the radiant.

Figure 7.7 shows that zenith attraction is most pronounced for slow meteors and even then only amounts to a deviation of a few degrees from the original angle. While infall velocity can be corrected to obtain the original orbital velocity of a meteor, zenith attraction is already built into the angle of arrival measurements used in the convolution method to search for shower activity. As such, it has not been compensated for in this study.

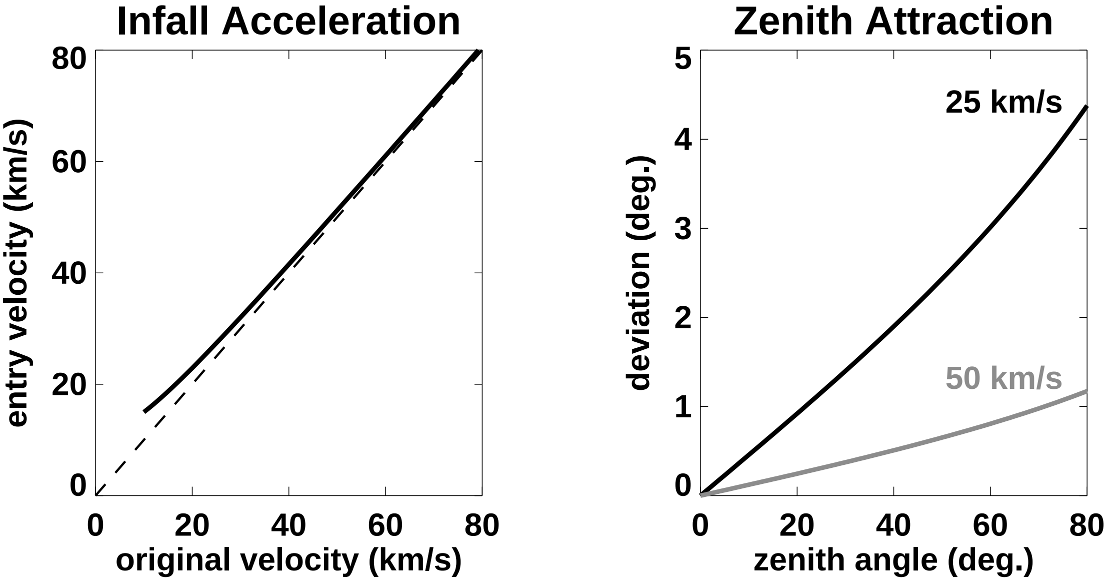

Figure 7.7: Left: Effect of gravitational acceleration on atmospheric entry velocity. The dashed line indicates no change Right: Change in angle between trajectory and local zenith due to gravitational attraction. Speeds given are pre-infall velocities.

7.3.3 Equations of orbital motion

Starting with the *vis-viva* equation, which is an expression of the conservation energy in an orbital system, these elements can be calculated [Chobotov, 2002]. The time of detection provides the necessary information to specify the position along the orbital path of Earth relative to fixed references. The radiant of the shower and the corrected pre-infall velocity of the shower meteors provide the direction and magnitude of the velocity vector of the shower at the time of detection. The known velocity vector of Earth can then be combined with the relative velocity vector of the shower to obtain v, the magnitude of the orbital velocity vector of the shower. The *vis-viva* equation is given by

$$v = \sqrt{\mu\left(\frac{2}{r} - \frac{1}{a}\right)}, \tag{7.5}$$

where r is the distance of the orbiting body from the focus of the orbit and a is the semi-major axis of the orbit. For a meteoroid detected at Earth, r is just the distance of Earth to the Sun, ≈1 AU. The standard gravitational parameter is $\mu = GM_{\odot}$, where G is the gravitational constant and $M_{\odot}$ is the mass of the central body in the system (here the Sun). Algebraic manipulation yields the semi-major axis from these known terms as

$$a = \left(\frac{2}{r} - \frac{v^2}{\mu}\right)^{-1}. \tag{7.6}$$

Kepler's laws of planetary motion provide the remaining orbital parameters necessary to reconstruct the orbits of the detected streams. The velocity component normal to the radial vector from the focus of the orbit to the object is given by

$$v_\perp = \frac{\sqrt{\mu p}}{r}. \tag{7.7}$$

This provides the length of the semi-latus rectum, p, which is the distance from the focus to the orbit when the argument of the orbit is 90°, making r perpendicular to the major axis. From the geometry of conic sections, we have

$$p = a\left(1 - e^2\right) \Rightarrow e = \sqrt{1 - \frac{p}{a}}, \tag{7.8}$$

which defines e using the the derived terms. Finally, the anomaly of the orbit, θ, at the time of detection can be found from

$$r = \frac{p}{1 + e\cos\theta}, \tag{7.9}$$

which is used with the argument of the ascending node and the radial component of orbital velocity, v_r, to determine the argument of the perihelion from the origin of the coordinate system. This is given by

$$\omega = \begin{cases} \theta & \text{for } v_r > 0 \\ \theta + 180^\circ & \text{for } v_r < 0 \end{cases}. \tag{7.10}$$

7.3.4 Orbits of detected shower streams

Equations 7.5 through 7.10 were used to calculate the orbits of the detected showers that had successful estimates of velocity. Of the 36 shower systems considered, orbital parameters were successfully calculated for 31 of the associated streams, which are shown in table 7.2.

The orbits that were not able to be calculated suffered from excessive uncertainties stemming from large velocity uncertainties and single day detections. The argument of the perihelion could not be resolved for two of the newly discovered showers. This term, however, is less important to the characterization of these orbits, given their nearly circular paths. Similarly, the α Puppids, η Carinids, and Unknown 2 have large uncertainties in the values of the perihelion argument, resulting from low eccentricity orbits.

Several orbits within the Aquariid complex have values of the ascending node that differ from accepted values by 180°. This is likely due to the proximity of the orbits to the ecliptic plane. As such, small errors in the inclination of the radiant can cause the ascending node to be mistaken for the descending node. Additionally, it is likely that deceleration biases in velocity estimates may have had a negative impact on the successful calculation of the orbital argument, which is used in conjunction with the ascending node to determine the argument of the perihelion.

The calculated orbits in table 7.2 can be categorized into four groups, as is evident in figure 7.8. Two groups fall into classic cometary orbits with high eccentricity and low inclination. The main population of 12 streams, including the δ Aquariid complex, have eccentricities of about 0.9 and inclinations of 10-40°. There is also an additional smaller population of 7 streams that have eccentricities of about 0.8 with inclinations of less than 10°.

With inclinations greater than 90°, streams with retrograde orbits travel around the Sun in the opposite direction of the planets. An example is the Orionid/η Aquariid stream, which was originally produced by comet 1P/Halley [McIntosh and Hajduk, 1983]. Two previously undetected showers that have retrograde orbits are similar in terms of inclination and eccentricity. They are not, however, the same stream, as their ascending nodes are separated by 46°.

The absence of low eccentricity orbits at low inclination is easily explained by the physical argument that this would require meteor streams to occupy a similar orbit to Earth, which would necessarily result in the rapid capture of meteors in such a stream.

shower name	Ω	ω	$\Delta\omega$	a (AU)	Δa (AU)	e	Δe	i	Δi
α Piscis Australids	306.4	138.0	6.4	2.82	1.31	0.936	0.030	32.3	23.6
α Puppids	95.0	82.2	40.2	1.70	0.12	0.432	0.046	71.2	1.7
Day χ Sagittariids	287.2	282.3	2.1	1.86	0.09	0.743	0.009	2.9	0.2
Day κ Leonids	179.5	325.6	2.8	2.72	1.01	0.955	0.009	20.0	2.3
Day Sagittariids–Capricorinids	119.7	273.6	5.0	2.03	0.10	0.734	0.014	9.3	0.2
η Aquariids	45.3	289.2	1.8	1.46	0.07	0.675	0.018	168.3	0.5
η Carinids	108.5	201.0	55.0	0.95	0.01	0.043	0.009	74.0	0.8
Geminids	261.5	143.2	2.6	1.32	0.09	0.884	0.004	18.0	0.5
July Phoenecids	293.3	63.8	4.3	1.38	0.07	0.346	0.035	73.5	0.6
Northern δ Aquariids	302.8	147.5	1.0	2.50	0.16	0.960	0.003	17.4	1.5
November Orionids	66.3	140.8	1.7	4.52	1.30	0.962	0.007	21.7	1.7
Orionids	24.4	108.8	7.8	1.42	0.45	0.617	0.113	163.0	0.8
ϕ Sagittariids	273.9	103.2	3.2	2.00	0.11	0.762	0.014	8.3	0.3
Piscis Austrinids	312.4	148.2	4.4	1.43	0.15	0.911	0.018	36.7	8.0
Quarantids	283.4	197.3	13.8	1.72	0.10	0.437	0.023	72.4	0.7
Sagittariids	260.6	155.6	1.3	1.00	0.04	0.905	0.008	46.1	3.0
Sextantids	8.6	326.1	1.7	1.09	0.03	0.858	0.007	23.9	1.0
Southern δ Aquariids	306.4	148.3	1.2	1.71	0.10	0.933	0.004	32.9	1.7
Southern ι Aquariids	307.3	156.4	1.5	1.64	0.06	0.962	0.003	12.0	0.7
τ Capricorinids	114.9	98.1	1.7	2.59	0.29	0.807	0.031	5.2	0.7
θ Ophiuchids	263.7	106.2	3.9	2.04	0.13	0.780	0.012	7.7	0.7
ζ Perseids	76.8	305.8	9.8	1.70	0.20	0.831	0.048	5.0	2.3
ζ Puppids	43.3	236.5	8.3	1.10	0.05	0.151	0.035	67.4	0.4
unknown 1	118.4	278.2	10.3	1.91	0.10	0.735	0.031	8.5	1.2
unknown 2	140.5	333.6	20.1	0.79	0.07	0.364	0.125	149.0	6.2
unknown 3	185.1	-	-	1.01	0.06	0.307	0.253	147.5	9.2
unknown 4	219.4	244.6	3.6	2.28	0.33	0.657	0.043	73.9	1.4
unknown 5	45.0	285.6	3.1	1.67	0.13	0.707	0.018	152.2	0.9
unknown 6	80.6	335.2	1.5	1.43	0.07	0.949	0.004	31.1	2.2
unknown 7	288.5	140.8	1.5	1.40	0.11	0.874	0.012	30.4	2.7
unknown 9	21.8	-	-	1.14	0.04	0.176	0.021	66.5	2.7

Table 7.2: Calculated orbital elements for detected showers, made from combined daily estimates. Ω = argument of the ascending node on the day of peak activity, ω = argument of the perihelion from the ascending node, a = semi-major axis, e = eccentricity, i = inclination relative to the plane of Earth's orbit. Errors indicate 95% confidence. (Originally published in Younger et al. [2009])

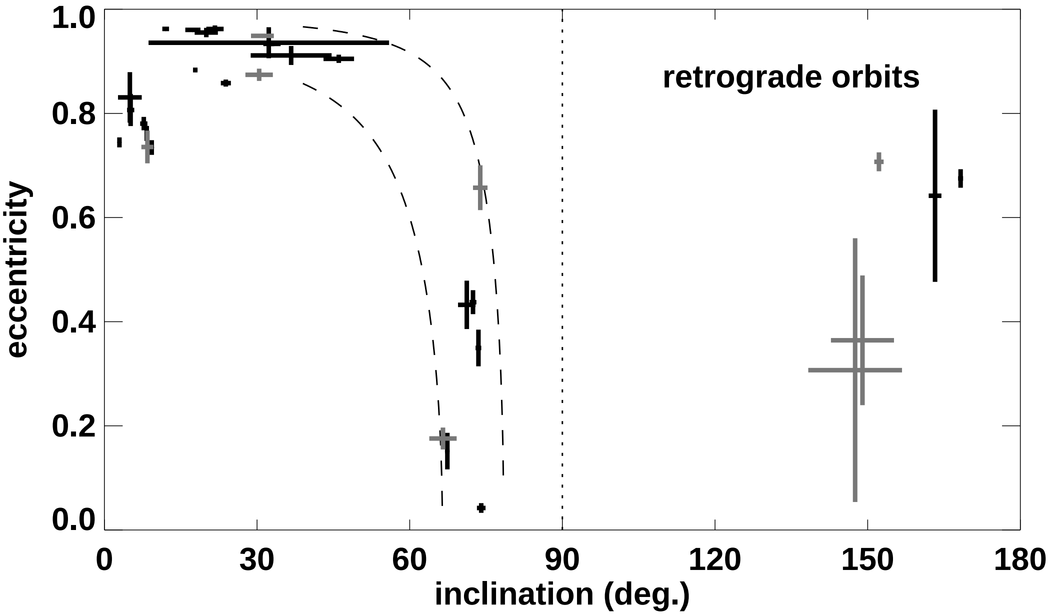

Figure 7.8: Calculated orbits of detected shower systems. Previously cataloged showers are dark, new discoveries are light. Error bars indicate 95% confidence. The dashed lines are Kozai resonance countours of $H_K = 0.4$ (left) and $H_K = 0.2$(right). (Originally published in Younger et al. [2009])

There is the possibility of debris streams with low eccentricity orbits at low inclination with mean orbital radii of less than or greater than 1 AU, but as their paths would not intersect Earth's orbit, they would not be detected as meteor showers.

All of the detected orbits are elliptical, which is to say that there are no extra-solar sources. Interstellar meteors are actually a common phenomena, and are routinely detected by capable systems [Baggaley et al., 1994]. These detections, however, are from what could be described as the interstellar sporadic background, as opposed to discrete filaments. The detection of a filament of debris would occur only once as the solar system passed through the stream, making such detections rare. Additionally, meteors in hyperbolic orbits have velocities in excess of 72 km s^{-1}, which is around the value that the Fresnel transform method of velocity estimation breaks down due to insufficient sampling frequency [Holdsworth et al., 2007].

7.3.5 Kozai resonance

The last group of orbits is a population of nearly circular orbits with inclinations in excess of 60°, making them almost perpendicular to the ecliptic plane. The orbits of these streams are positioned relative to the cometary orbits as to suggest that Kozai resonance is responsible for their orbital characteristics.

Kozai found that under some circumstances, small orbital perturbations can occur such that the Delaunay quantity, $H_K = (1 - e^2)\cos i$, is conserved [Kozai, 1962]. The result of this is that orbits undergoing perturbation can exchange eccentricity for inclination, shifting elongated orbits that are close to the ecliptic plane to highly inclined, nearly circular orbits.

Figure 7.8 shows several contours of H_K that seem to link the population of low eccentricity, high inclination orbits with the population of cometary orbits with high eccentricity and low inclination. While not conclusive, this relationship suggests that high inclination, low eccentricity meteor streams are the product of Kozai resonance acting on conventional cometary orbits. This may indicate the origin of the toroidal sources of sporadic meteors seen at high inclinations.

7.4 Summary

The inability of single station radars to determine the direction of travel of individual underdense meteors can be overcome using statistical methods to detect meteor showers. The specular reflection condition produces rings of perpendicular detections for showers when plotted on the celestial sphere. By searching for bands of increased detection density, meteor showers can be detected.

The great circle method for detecting meteor showers can be improved by applying a weighting function to the convolution. The Jones and Jones type weighting function increases angular resolution by compensating for false detection attribution when the radiant of interest is offset from an active shower radiant.

A survey of meteor detections collected during 2006-2007 at Davis Station, Antarctica and Darwin, Australia resulted in the detection of 598 individual meteor shower detections. When sorted, these shower detections comprise 37 different shower systems, of which 9 are not present in catalogs. Strong contributing factors to the high discovery rate are the high detection rate of the radars and the ability to detect daytime showers that would not be detected using conventional visual or photographic methods.

Meteoroid velocity was successfully estimated for 522 of the shower events from 36 of the shower systems. An analysis of the uncertainties of the velocity estimates allowed the precision of the Fresnel transform method to be evaluated. It was found that the Fresnel transform velocity can resolve meteor velocity to within ±8%.

Knowledge of the direction and velocity of meteor showers allows the orbits of the parent streams to be calculated. Orbital parameters were successfully determined for 31 of the 37 detected shower systems, including 8 of the newly discovered systems. The orbits of the detected showers were shown to belong to four distinct groups. It was shown that Kozai resonance is likely responsible for the occurrence of meteor streams at high inclinations with nearly circular orbits.

Chapter 8

Conclusions

This thesis describes research conducted across a range of topics involving interferometric VHF meteor radar. A logical progression was followed, beginning with a description of meteor radar operation and the formation of meteoric ionization, before moving on to discuss the nature of meteor radar echoes and the application of observable features to atmospheric and astronomical research.

In Chapter 1, a number of questions were posed as a summary of the goals of the original research described in this thesis. These questions, highlighted in italics, are presented again below with synopses of the answers found, which summarize the findings made throughout the course of the research described in this thesis.

8.1 Meteor Radar Performance

Of particular importance to any radar is the positional accuracy of the system. Meteor echoes are used to characterize the atmospheric conditions where they occur, so it is desirable to maximize the accuracy and precision of the positional component of meteor radar detections. The positional accuracy of a meteor radar depends on the accuracy of the measurements of range to the meteor and angle-of-arrival of the backscattered wavefronts. Range accuracy depends on the pulse length used. Angle of arrival accuracy depends on antenna spacing and the accuracy of phase difference measurements. At long ranges, near the horizon, uncertainty in the position of meteors is dominated by uncertainty in the angle-of-arrival.

What is the effect of mutual coupling of antennas on angle-of-arrival estimates of meteor radar echoes?

Systematic errors in the angle-of-arrival estimate first occur in the received signal flow in the form of mutual coupling between receiving antennas. The current induced by wavefronts incident on antennas gives rise to fields that induce currents in adjacent antennas. This produces errors in the estimates of the phase of incoming wavefronts that are dependent on the true angle-of-arrival. Modeling based on measurements of mutual coupling in a working array shows that mutual coupling produces small errors in the estimates of angle-of-arrival, but that these errors are mostly compensated for by the calibration process.

How can meteor echo decay times be used to infer phase measurement biases in a meteor radar receiver?

A method for calibrating meteor detection data was presented, using estimates of the ambipolar diffusion coefficient. Spherical shells were fit to diffusion coefficient and height data, under the assumption that meteor detections with the same echo decay time observed during a small time period all occur at the same height. It was found that this method is equivalent to hardware phase calibration routines that rely on the phase data of individual antennas. This new method allows older data sets to be re-calibrated, even when the original antenna phase data has been discarded.

8.2 Meteoroid Ablation

An understanding of the processes that take place during the ablation of a meteoroid in the atmosphere enables further investigations of the characteristics of meteor radar detections. The formation of meteor trails in the atmosphere was examined by numerically simulating the ablation and ionization processes of meteors with different initial conditions in different atmospheric environments. The predictions of the numerical simulations allowed an investigation into factors determining whether or not individual meteors are detected.

What is the distribution of initial meteoroid sizes that produce detected meteors?

The simulation results indicate that the size distribution of detected meteors is approximately Gaussian, with the peak initial size of detected meteoroids dependent on the sensitivity and wavelength of the observing radar. Using representative figures for the types of radars used in this study, it was found that the median initial diameter of detected meteors is in the 500-700 μm range. Knowlege of the initial size distribution of detected meteors will assist in the use of meteor radar observations to estimate the total meteor mass influx.

What role does sputtering play on the formation of meteoric ionization?

The simulations predict that sputtering plays a negligible role in the production of detectable ionized material in meteor trails. For the most extreme cases, sputtering only accounted for 1-2% of meteoroid mass loss. In light of this finding, it is acceptable to consider mass loss during meteoroid ablation to be entirely due to evaporation. This greatly simplifies the mathematics concerning the thermal properties of meteoroids during ablation.

8.3 Meteor Detection Height

Meteor radars routinely detect tens of thousands of meteors per day across a range of heights. The distribution of heights at which meteors are detected can provide information about the atmospheric density profile in the meteoroid ablation region. The simulation of a variety of meteor types allowed predicted meteor detection height distributions to be constructed for different atmospheric conditions. The predictions of the numerical simulations were then confirmed through comparison with observed meteor detection height distributions.

How does the density scale height affect the height distribution of detected meteors?

It was shown that the range of heights over which meteors are detected is an almost linear function of the density scale height of the atmosphere. This is due to the reduction in path length over which a meteoroid is actively evaporating in an atmosphere with a stronger density gradient.

How is the peak meteor detection height affected by changes in the height of constant density levels?

It was also shown that there is a correlation between the height of constant density contours in the atmosphere and the peak detection height of meteors. While there was more scatter in the relation between peak height and constant density level than between scale height and detection zone width, the general correlation indicates that the peak height of meteor detections can be used as an indicator of variations in atmospheric density. This is due to the overall vertical movement of the entire meteoroid ablation region of the atmosphere.

8.4 Underdense Echoes

Fresnel geometry is responsible for the pattern of backscattered intensity observed over time from meteor trails. Simple exponential decay is the result of radial diffusion increasing destructive interference in regions away from the trail axis. The evolution of backscattered intensity from underdense meteor trails over time was considered, starting with a review of standard echo theory. The ‘ideal’ case of an echo consisting of a Fresnel diffraction pattern decaying exponentially due to the diffusion of free electrons away from the trail axis was modified for different possible scenarios, in order to determine the effects on echo decay times.

What is the effect of non-constant meteor trail electron line density on the decay time of a meteor radar echo?

It was shown that variations in electron density along the meteor trail axis modify the amplitude of the Fresnel oscillations of the echo, but not the average intensity. The amplitude of the observed diffraction pattern produced by backscatter from a meteor trail is a convolution of the Fresnel functions, the electron line density, which is fixed along the trail, and the exponential decay function which moves with the head of the meteor along the trail. Therefore, the electron line density modulates the amplitude of the Fresnel oscillations, but does not affect the decay time of the echo.

How is the meteor echo decay time affected if the diffusion coefficient varies along the length of a meteor trail?

The case of a diffusion coefficient varying along the length of a meteor trail was shown to have a negligible effect on the decay time of the echo. This is due to the relatively narrow Fresnel zone region responsible for nearly all of the observed backscatter. All of the backscatter intensity, with the exception of the small amplitude Fresnel oscillations, is the result of scatter from the central Fresnel zones around the specular point. Hence, it is the diffusion coefficient at the specular point of the meteor trail that dominates the decay properties of the meteor radar echo.

What effect does fragmentation have on the decay time and diffraction pattern properties of a meteor echo?

It was shown that co-axial fragmentation obscures Fresnel oscillation features in the observed echo, but does not affect the decay time. The precise effect depends on the relative size of the fragments, the spacing between fragments, and the wavelength of the observing radar. Small spacings have the effect of smoothing the Fresnel oscillations, while larger spacings can produce irregular oscillations, including multiple sub-peaks prior to the peak echo intensity.

8.5 Anomalous Diffusion Phenomena

Simultaneous observations of the same meteors by co-located radars with different wavelengths have shown that the standard echo model assuming linear diffusion is not completely accurate. Having removed different properties of the meteor from consideration in the investigation of anomalous echo decay times, the diffusive processes themselves were then examined. Modifications to simple linear diffusion model were applied in the form of multiple ionic species and absorbing aerosols.

What is the decay time of the echo from a meteor trail composed of multiple ionic species?

It was shown that the presence of multiple ionic species in a meteor trail manifests in the the diffusion process in two ways. The different effective diffusion cross-section of different ions causes different ions to begin diffusing from different initial radii. Additionally, different ions diffuse at different rates. The effect of multiple ionic species on decay times depends on the initial distributions of the different species and the wavelength of the observing radar.

How are meteor echo decay times affected if each ionic species has a unique initial distribution?

Using numerical simulations of ion diffusion and resultant echo intensity, it was shown that differential diffusion has negligible effect on echo decay times when all ionic species have the same initial distribution about the meteor trail axis. When individual species have different initial radii, it was found that differential diffusion can produce higher estimates of the diffusion coefficient for shorter wavelengths than those produced using larger wavelengths.

What is the wavelength-specific effect of aerosol absorption on the decay time of meteor echoes?

Aerosol absorption was investigated by numerically simulating the diffusion of ionized material in an environment that included aerosols absorbing free electrons from the trail. Results of the simulations show that the effect of aerosol absorption is dependent on the aerosol parameters, the electron line density of the meteor trail, and the wavelength of the observing radar. The predictions indicate an increase in the deviation between the diffusion coefficient estimates from radars with different wavelengths for meteor trails with low electron line densities.

How do numerical predictions of aerosol absorption compare with the observations of co-located radars with different wavelengths?

The predictions of the numerical simulations of the impact of aerosol absorption on meteor echo decay times are consistent with the observations of co-located 33 and 55 MHz radars operating at Davis Station Antarctica. As such, it is possible that aerosol absorption is responsible to some degree for the disparity in diffusion coefficient estimates from radars with different frequencies.

8.6 Meteor Astronomy

Meteor radar usually focuses on the use of meteor detections for atmospheric research. The specular reflection condition restricts knowledge of the path of an individual meteor to a plane perpendicular to the line of sight from the radar. This ambiguity can be overcome by applying a statistical analysis to large numbers of detections, allowing for the detection of discrete meteor showers. The great circle method of meteor shower detection for single station radars with a Jones and Jones type weighting function was used to produce a survey of meteor showers.

What meteor showers can be detected using single station meteor radar observations *in the southern hemisphere?*

Meteor detections were collected from meteor radars at Davis Station, Antarctica and Darwin, Australia over 2006-2007. 598 individual shower detections were observed, comprising 37 different shower systems. Of these, 9 showers were not present in catalogs of shower activity. The large number of new discoveries is due in part to the ability of radar to detect meteor showers during daylight hours.

How can shower meteors be used to estimate the precision of the Fresnel transform velocity estimation technique?

The velocities of detected shower meteors were used to estimate the precision of the Fresnel transform velocity estimation method. The distribution of relative uncertainties in the velocity estimate of detected showers displays a sharp peak at 8%, which is consistent with previous estimates made by other means of the precision of the Fresnel transform velocity estimation method.

What are the orbital characteristics of debris streams responsible for meteor showers?

The velocity of shower meteors was used in conjunction with the radiants of the detected meteor showers to calculate the orbits of the debris streams responsible for the detected showers. Orbits were successfully calculated for 31 of the detected shower systems. It was shown that the detected meteor shower systems can be categorized into 4 distinct groups using orbital eccentricity and inclination. The presence of nearly circular high-inclination orbits is consistent with the application of Kozai resonance to highly elliptical low-inclination cometary orbits.

8.7 Future Work

Meteor radars have evolved from simple, labor intensive, low-count, systems used primarily for rough estimates of mesospheric winds to automated systems that detect tens of thousands of meteors every day. The uses of meteor radars have expanded, now encompassing wind measurement, atmospheric temperature, atmospheric density, and meteor astronomy.

The primary advantage of a meteor radar system is that it operates with a wide field of view, day or night, in all weather conditions. This is tempered by the limitations of range resolution on the order of 1 km and the need for external data or assumptions to produce an absolute measurement of atmospheric temperature or density.

As such, meteor radar is best suited to integration into a suite of sensors that can complement each other. Ideally, a co-located meteor radar and lidar can work in unison, with the lidar obtaining high-precision measurements when weather and lighting conditions permit, with diffusion coefficient data from the meteor radar being used to complete the atmospheric equation of state. The intermittent lidar measurements can be fed into a near-realtime atmospheric model that will complete the diffusion coefficient data of the meteor radar when lidar data is not available.

Meteor astronomy remains best conducted with dedicated multiple station systems, so as to completely specify the trajectories of individual meteors. Recent advances in the sensitivity of interferometric meteor radars mean that single station systems, however, are still of some considerable utility. With daily detections numbering in the tens of thousands per day and large amounts of computational power readily at hand, large scale surveys are simply a matter of implementing detection algorithms with existing data sets.

The progress presented in this thesis is also relevant to systems outside of purpose-built meteor radars. Medium frequency (MF) radars with transmitting frequencies of a few MHz were commonly used for meteor detection in the early days of meteor radar. Modern analysis techniques can improve the sensitivity, allowing the highest occurring meteor trails to be detected. At heights over 100 km meteor trail evolution is thought to be strongly influenced by the geomagnetic field. Additionally, HF over-the-horizon radars are becoming more common for ionospheric research and long range surveillance applications. Meteor detections from these systems present an opportunity for both calibration of the systems and further research into meteor phenomena.

Appendix A

Glossary of Mathematical Terms

Note: Where duplicate terms occur, an individual entry is provided for each definition. Terms are listed alphabetically and by their order of appearance.

α: bias in phase measurement

α: sputtering molecular mass ratio function

$\bar{\alpha}$: average polarizability

α_d: attenuation due to outward diffusion of the meteor trail

α_r: attenuation due to the initial radius of the meteor trail

α_v: attenuation due to the finite velocity of the meteor

β: ionizing efficiency

χ: phase difference between two antennas

χ': biased phase difference between two antennas

$\delta\theta$: width of radiant acceptance band weighting function

Δ: velovity-diffusion-range constant used to calculate α_v

ΔA: difference between echo amplitude at maximum gradient and maximum amplitude

Δh: width of the meteor detection region

Δt: time taken for echo amplitude to rise between maximum gradient to maximum amplitude

ϵ: emissivity

ϵ_0: permittivity of free space

ϕ: azimuth angle

γ: reduced energy of a collision

Γ: drag coefficient

η: aerosol Coulomb interaction term used to calculate R_{ed}

κ: dielectric constant

κ_n: accomodation coefficient

λ: wavelength of the radar

$\lambda_\odot$: solar longitude

Λ: heat transfer coefficent

μ_i: reduced molar mass of ion and atmospheric molecule

θ: zenith angle

θ: angle between incident path and surface normal

θ: anglular distance from the center of the acceptance band

θ: orbital anomaly

ρ_a: density of the atmosphere

ρ_{a0}: density of the atmosphere at a reference height

ρ_{a1}: density of the atmosphere at beginning of detectable ionization

ρ_i: density of constituent i

ρ_m: meteoroid density

σ: Stefan-Boltzmann constant

σ_h: uncertainty in the height estimate

τ: exponential time decay constant of the meteor echo

ω: argument of the perihelion from the ascending node

ω: argument of the ascending node

ψ: angle between angle of arrival and antenna pair baseline

Ψ: set of candidates for the angle of arrival

Ψ': set of biased candidates for the angle of arrival

a: screening length

a: density exponential dependance of initial radius

a: semi-major axis of orbit

A_{max}: maximum echo amplitude

A_R: backscatter amplitude/trail reflectivity

a_0: Bohr radius

b: velocity exponential dependance of initial radius

Bi: Biot number

c: adaptive time step

c: speed of light

C: Fresnel cosine integral

C_L: Langmuir constant

c_p: meteoroid heat capacity

d: distance between two antennas

d: mean diamter of gas molecules

D: ambipolar diffusion coefficent

e: orbital eccentricity

e: charge of an electron

$\mathbf{E}$: identity matrix

E: kinetic energy of an incident molecule

E_i: surface binding energy of constituent i

E_s: energy consumed per unit surface area by vaporization

E_{th}: threshold energy required to remove a molecule from the lattice

F: mass flux of meteors

g: acceleration due to gravity

G: maximum transferable fraction of energy in an elastic collision

G_R: gain of the receiving antenna

G_T: gain of the transmitting antenna

h: height above the ground

$H*$: density scale height of the atmosphere

h_0: reference height

h_1: height at beginning of detectable ionization

h_2: height at end of detectable ionization

H_K: Kozai parameter h_v: latent heat of vaporization

i: square root of -1

i: inclination of orbit

I: current

k: Boltzmann constant

K: free parameter

k_n: Knudsen number

l: mean free path

m: meteoroid mass

m_e: electron mass

$M_\oplus$: mass of Earth

M_1: mean molecular mass of incident molecule

M_2: mean molecular mass of sputtered target material

M_a: atmospheric molecule molar mass

M_i: ion molar mass

m_{mol}: mass per mole of meteoroid

n: number density of diffusing particles

n_a: number density of atmospheric molecules

n_d: number density of aerosol

n_e: number density of free electrons

n_i: number density of ions

N: meteor trail electron volume density

N_A: Avogadro's number

p: pressure

p: semi-latus rectum of orbit

P_h: power consumed heating the meteoroid

P_{in}: power input to the meteoroid by collisions with atmospheric molecules

P_{rad}: power lost due to radiation

P_R: backscatter power

P_{Rmin}: minimum power detectable by the radar receiver

P_T: transmitted power

p_v: vapor pressure

P_{vap}: power lost due to vaporization

q: electron line density of the meteor trail

q: argument of the perihelion of an orbit

q_{min}: minimum detectable electron line density

q_c: critical electron line density marking the transition from underdense to overdense

R: range from radar to meteor

R: universal gas constant

R: mean penetration length

R_0: range from meteor specular point to radar

r: particle radius

r_0: initial radius of the meteor trail

r_a: distance from the center of the Earth to atmospheric entry height

r_e: classical electron radius

R_e: radius of the Earth

R_{ed}: aerosol electron capture rate

R_p: mean projected range

s: cross-sectional area

s: meteor trail length, measured from specular point

S: Fresnel sine integral

$\mathbf{S}$: matrix of s-parameters

s_n: universal function of the reduced energy of a collision

S_n: nuclear stopping cross section

t: time elapsed

t_I: radar pulse repetition interval

T: temperature

T_a: temperature of the atmosphere

U_0: lattice energy

v: velocity of the meteor

v_a: velocity of meteor at atmospheric entry

v_r: radial component of orbital velocity

v_∞: velovity of meteor prior to infall

$v_\perp$: component of orbital velocity perpendicular to radial vector

V: voltage

V_A: potential of an electric field incident on an antenna

v_i: velocity prior to atmospheric entry

V_O: voltage observed on an antenna

v_{obs}: observed velocity

$\mathbf{Y}$: matrix of admittance parameters

x: meteor trail length in Fresnel zones, measured from the specular point

Y_i: sputtering yield for constituent i

Z: impedance

Z_1: atomic number of incident molecule

Z_2: atomic number of sputtered target material

Z_d: aerosol charge number

Appendix B

Published Paper: Geophys. Res. Lett., 35(L15812):1-4, 2008

GEOPHYSICAL RESEARCH LETTERS, VOL. 35, L15812, doi:10.1029/2008GL033763, 2008

Modeling and observing the effect of aerosols on meteor radar measurements of the atmosphere

J. P. Younger,[1] I. M. Reid,[1,2] R. A. Vincent,[1] and D. A. Holdsworth[2]

Received 25 February 2008; revised 2 July 2008; accepted 11 July 2008; published 13 August 2008.

[1] Measurements of the time taken for meteor radar echoes to decay can be used to estimate the ambipolar diffusion coefficient. If it is assumed that the decay of the radar echo is due strictly to the outward diffusion of ionized material in the meteor's trail, then echo decay is determined by temperature and pressure. However, dust particles or small ice crystals may absorb electrons from meteor trails, distorting their evolution and echo decay properties. A numerical method for modeling these processes is presented, with the prediction that absorbing aerosols can both decrease and increase the decay time of meteor radar echoes, depending on meteor, atmospheric, and radar parameters. This prediction is confirmed with observations taken using three 33 MHz and two 55 MHz radars at three locations in Australia and Antarctica, which display strong biases in the decay times of lower power echoes. It is suggested that both the accuracy and precision of atmospheric measurements are improved if only the highest power meteor echoes are used for estimates of the ambipolar diffusion coefficient.

Citation: Younger, J. P., I. M. Reid, R. A. Vincent, and D. A. Holdsworth (2008), Modeling and observing the effect of aerosols on meteor radar measurements of the atmosphere, *Geophys. Res. Lett.*, *35*, L15812, doi:10.1029/2008GL033763.

1. Introduction

[2] Radar echoes from underdense meteor trails have been used for over five decades to infer the properties of the 80–110 km region of the atmosphere through which they pass. Interest in climate change has added to the urgency of improving observation methods in the difficult to measure mesospheric region, where significant effects are expected to be seen. Current methods rely on the assumption that the evolution of a trail of ionized material left by an ablating meteoroid is governed entirely by diffusive processes. In this case, a trail's radar echo at a given frequency decays exponentially with time, at a rate determined by the local temperature and pressure. While absorption and recombination of electrons in the trail by ambient atmospheric molecules can be neglected due to the relatively large timescales involved, the presence of dust and ice particles in the upper atmosphere presents a substantial sink for free electrons in a meteor trail. Dust is present in the upper atmosphere due to the condensation of evaporated meteoric material and small meteoroids that are slowed to thermal velocities before ablation. In extremely cold conditions, ice crystals may nucleate on dust particles, which is seen in the development of Polar Mesospheric Summer Echoes [*Cho et al.*, 1994]. The loss of free electrons by attachment to aerosols can alter the trail's radio scattering behavior, causing deviation from the strictly exponential decay seen in underdense meteor radar echoes. Measurements of meteor diffusion coefficients gathered at Davis Station, Antarctica over 2006 showed a strong dependence on the frequency of the observing radar. Additionally, observations described by *Singer et al.* [2008] showed a correlation between the measured diffusion coefficient and the strength of the meteor trail echo. These results suggest that some other mechanism beyond ordinary diffusion is affecting the evolution of meteor trails in the mesosphere. We show that absorption by aerosols plays a dominant role in producing these discrepancies.

2. Meteor Radar Echoes

[3] After passage through the atmosphere, meteors leave a cylindrical trail of ionization with an approximately Gaussian density distribution about the axis. If the density of free electrons in the trail does not exceed the critical density of a given radar frequency, the meteor is classed as underdense and exhibits distinctive echo decay characteristics. The free electrons in the trail scatter incident radiation continuously throughout the body of the trail. *McKinley* [1961] shows that the amplitude of the scattered radiation given by

$$A \propto 2\pi \int_0^\infty n_e(r,t) r J_0\left(\frac{4\pi r}{\lambda}\right) dr, \qquad (1)$$

where $n_e(r, t)$ is the density of free electrons in the trail, r is the distance measured from the axis of the trail, t is the time since formation, λ is the wavelength of the incident radiation, and J_0 is a zero-order Bessel function.

[4] The ionized material in the trail diffuses outward at a rate determined by the local temperature and pressure, as described in the diffusion equation:

$$\frac{\partial n_e(r,t)}{\partial t} = D\nabla^2 n_e(r,t), \qquad (2)$$

where D is the ambipolar diffusion coefficient. If a Gaussian initial density distribution is used, an analytic solution is possible. The result of diffusion is then an exponential decay in the scattered signal with the time taken to decay by a factor of e^{-1} of

$$\tau = \frac{\lambda^2}{16\pi^2 D}. \qquad (3)$$

---

[1] Department of Physics, University of Adelaide, Adelaide, South Australia, Australia.

[2] ATRAD Pty. Ltd., Thebarton, South Australia, Australia.

0094-8276/08/2008GL033763$05.00

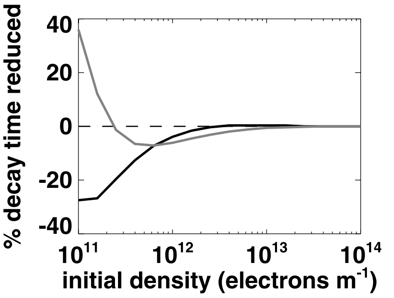

Figure 1. An example of model predictions of reduction in decay times for 33 MHz (light) and 55 MHz (dark) radar for various trail densities. 1.0 m initial radius trail with aerosol parameters $n_d = 5 \times 10^9$ m^{-3} and $R_{ed} = 10^{-8}$ m^3 s^{-1}.

[5] Thus, by measuring the decay constant of underdense meteor echoes, it is possible to infer D, which is a function of temperature and pressure.

$$D = \frac{2k}{e}\left(\frac{1.013 \times 10^5}{273.6}\right)\left(\frac{T^2}{p}\right)K_0, \tag{4}$$

where k is the Boltzmann constant, e is the charge of a single electron, T is the atmospheric temperature, and p is the pressure. K_0 is the ionic mobility of the meteoric constituents, with a typical value of about 2.5×10^{-4} m^2 s^{-1} volts^{-1} [*Chilson et al.*, 1996]. With the input of the missing term from another sensor or an atmospheric model, temperature or pressure can be estimated.

[6] So far, this model assumes that the development of the meteor trail is determined only by diffusion, with the overall free electron content remaining constant over time. It is known however that the upper atmosphere is populated by aerosols in the form of dust particles condensed from evaporated meteoric material and ice crystals that nucleate on the dust particles. *Havnes and Sigernes* [2005] considered the possibility that aerosols may absorb electrons from meteor trails, in which case the development of the trail is governed by a modified diffusion equation:

$$\frac{\partial n_e(r,t)}{\partial t} = D\nabla^2 n_e(r,t) - n_e(r,t)n_d(r,t)R_{ed}, \tag{5}$$

where n_d is the density of dust particles and R_{ed} is the electron capture rate of the dust particles. This equation no longer admits an analytic solution, so it must be handled numerically.

3. Numerical solution

[7] *Jones* [1995] considered the possibility of a non-Gaussian initial distribution of ionization about the trail axis and found that the Fourier transform of the density distribution of the trail decays exponentially with time, regardless of the shape. This result can be exploited to produce an iterative method for calculating the diffusion of ionized material in an absorptive environment. The process is written explicitly as

$$\begin{aligned} n_e(r, t + \Delta t) = & \int_0^\infty sa(s,t)e^{-Ds^2\Delta t}J_0(sr)ds \\ & - n_e(r,t)n_d(r,t)R_{ed}\Delta t \end{aligned} \tag{6}$$

with $a(s, t)$ the Fourier transform of $n_e(r, t)$. The integral calculates the diffusion of a radially symmetric trail deformed by absorption over a small time step Δt. The term being subtracted is a linear estimate of the free electrons absorbed over the same time step.

[8] Using this method, the density profile and corresponding scattered amplitude were calculated for a variety of dust conditions and meteor trail densities. Dust particle densities supplied to the model ranged from 5×10^9 to 5×10^{10} particles m^{-3} in keeping with current estimates of mesospheric dust from rocket observations described by *Amyx et al.* [2007]. Initial trail radii of 1.0, 0.75 and 0.5 m were used, along with typical meteor initial densities of 10^{11} – 10^{14} electrons m^{-1}. D was held fixed at a value of 2.0 m^2 s^{-1}, typical of conditions around 85 km.

[9] Of particular importance was the selection of the electron capture rate, R_{ed}, which is a function of electron temperature, particle radius, and particle charge. Following the calculations described by *Rapp* [2000], particles were assumed to be in the size range of 1–100 nm with a small or neutral charge. *Natanson* [1960] provides analytic approximations that give likely capture rates in the range of 10^{-10} – 10^{-8} m^3 s^{-1}, over which the solution was calculated.

4. Model Predictions

[10] Decay curves were constructed from the scattering amplitude over time for a 33MHz and a 55MHz radar, which were compared with the theoretical decay of trail echoes due to diffusion only. The results predicted that meteors with high initial electron line densities will be relatively unaffected by the presence of absorbing aerosols.

[11] Below about 10^{13} electrons m^{-1}, predicted decay times could be reduced when compared to the diffusion-only case, as also predicted by *Havnes and Sigernes* [2005]. In some cases, decay times could actually be larger than if free electrons had not been absorbed, as can be seen in the negative reduction in decay times in Figure 1. 55 MHz was most prone to extended decay times, with the effect occurring in conditions with high electron capture rates, although 33 MHz did sometimes show extended decay times over finite regions. Unsurprisingly, decay times suffered only minor reductions in environments with low particle densities and capture rates.

[12] The reason behind the rather counter-intuitive prediction of extended decay times lies in the physics of the formation of the meteor echo and the timing and location of the absorption of electrons from the meteor trail. Equation 1, which gives the amplitude of radiation scattered from a trail is a convolution of two terms: the radial density profile and a weighting function based on the distance from the trail axis and a Bessel function of wavelength and radial distance. The density profile is approximately Gaussian and the weighting function is periodic with increasing amplitude,

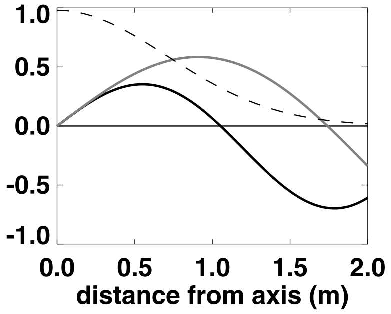

Figure 2. Weighting functions $rJ_0(4\ \pi r/\lambda)$ for 33 MHz (light) and 55 MHz (dark) radars. A Gaussian density profile with a 1.0 m radius (dashed) is shown for comparison.

which are shown together for comparison at the two wavelengths considered in Figure 2.

[13] Early in the trail's life, absorption occurs mostly at the center of the trail, where both the dust and electron densities are high. During this phase, the electron density is removed from a region where the weighting function is positive, lowering the scattered amplitude. As the dust in the center of the trail becomes saturated, the absorption process moves outward in an annular ring, while diffusion acts to move electron density from the center of the trail toward the edges. In the event that significant absorption occurs in the region where the weighting function is negative, a negative contribution will be removed from the final integration, resulting in an increase in scattered amplitude.

[14] Thus, under certain conditions, absorption can act to produce longer echoes than if diffusion was the only active process. In both cases, absorption is only significant for trails with densities approaching the absorbing aerosol density. Higher density trails may saturate the background absorbers, with little relative effect on the trail density profile.

5. Observations

[15] To investigate the model's predictions, records of meteor detections from three locations were used. Collocated 33 and 55MHz radars were operated over the course of 2006 at Davis Station, Antarctica (68°S). A 33 MHz radar was operated during 2006 at Darwin, Australia (12°S). Finally, a composite 7 month period was constructed from 2006–7 observations made with a 55 MHz radar at Buckland Park, Australia (35°S), with an additional month of data acquired when the Darwin 33 MHz radar underwent field testing at Buckland Park during September–October 2005. All radars were of a five-element interferometric design using ATRAD analysis software, as described by *Holdsworth et al.* [2004, 2008].

[16] The data were prepared by limiting detections to unambiguous underdense meteors detected between 15–75° off-zenith to remove grazing meteors at the top of the atmosphere and an overabundance of weak detections near the horizon. Additionally, only meteors below 90 km were considered, in order to avoid possible geomagnetic and other anomalous diffusion effects [*Dyrud et al.*, 2001; *Jones*, 1995]. An 80 km floor for the data provided adequate detections at both frequencies.

[17] Monthly data at each location and frequency were divided into the 25% weakest and 25% strongest signal power echoes using two applications of a median function. The mean decay times were obtained for 2 km height bins in each subset by fitting a Gaussian curve to the histogram of decay times with a bin width 0.1 $\log_{10}$ s. Figure 3 shows a typical month's diffusion coefficient profile, showing both extended and reduced decay times for lower power echoes when compared to higher power echoes.

[18] For the 55 MHz radars at Buckland Park and Davis Station, extended decay times were observed for weak meteors at all altitudes at all times. All 33 MHz detections obtained from the Darwin 2006 data and the month of 33 MHz testing at Buckland Park exhibited decreased decay times for weak meteors in the 80–86km region. This was repeated in spring and autumn in the 33 MHz observations from Davis Station, but extended decay times were observed for weak meteors at 33 MHz over the Antarctic winter and January-December.

[19] A comparison of monthly mean diffusion coefficients in 2 km altitude bins for 2006 obtained from 55 and 33 MHz meteor detections at Davis Station showed a converging agreement between the two frequencies' estimates when detections were limited to stronger echoes, as can be seen in Figure 4. In all locations, weak echo decay times below 85 km deviated from those of strong echoes by as much as 30%, which would produce a temperature bias in excess of 5 K in estimates for the entire data set when using the methods described by *Tsutsumi et al.* [1994] and *Cervera and Reid* [2000]. In no cases were the weak meteor biases found to depend on angle of arrival, meteor velocity, or time of day.

6. Discussion

[20] Two possibilities may account for the seemingly incongruous behavior of the Davis Station 33 MHz observations in summer and winter. Firstly, the model predictions do not take into account the possibility of multiple absorptions by a single particle, which would be the case in the summer months when large PMSE-related ice crystals could act as electron scavengers in the mesosphere. Secondly,

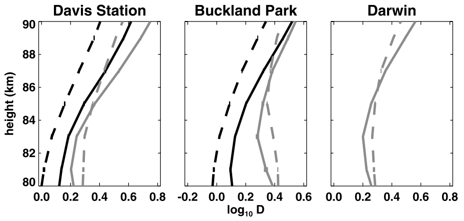

Figure 3. Mean ambipolar diffusion coefficient estimates for March 2006 (October/September for Buckland Park 33 MHz): 25% weakest meteor echoes (dashed) and the 25% strongest meteor echoes (solid) using 33 MHz (light) and 55 MHz (dark) radars. Error bars, where visible, are two standard errors.

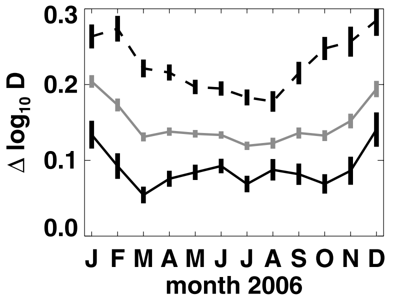

Figure 4. Difference in monthly mean diffusion coefficient estimates at 83 km for 2006 at Davis Station, Antarctica. $\Delta\log_{10}D$ is the difference in the logarithm of the 33 MHz and 55 MHz estimates of the ambipolar diffusion coefficient, obtained using the 25% weakest detections from each radar (dashed), all detections (light), and only the 25% strongest detections (dark). Error bars are two standard errors.

dramatic seasonal density variations were noted in the form of a mean detection altitude that was 3 km lower in winter than in summer at both frequencies. Such a change in local atmospheric parameters complicates comparisons of observations acquired at the same geometric height between different seasons. The clear prediction of the model was that meteors with low initial electron line density would be most affected by aerosols, with little to no effect on denser trails. This was seen in the dependence of the deviation between the Davis Station 33 and 55 MHz radars' estimates of *D* on the strength of the echoes being compared. This effect was sharply peaked in summer, when the polar mesosphere reaches the coldest temperature in the terrestrial environment. The attendant cessation of sublimation results in the formation of PMSE-related ice crystals in the mesosphere, which could be capable of absorbing significant numbers of free electrons.

7. Conclusions

[21] The observation of converging estimates of the ambipolar diffusion coefficient with increasing meteor strength, as well as frequency-dependent biases between weak and strong meteors, serve to reinforce the conclusion that underdense meteors with low initial electron line density are affected by absorptive processes related to the presence of dust and ice particles in the upper atmosphere.

[22] In light of these findings, future attempts to use underdense meteor radar echo decay times to estimate atmospheric temperature and pressure should rely on only higher power detections, corresponding to meteor trails with higher electron line densities. An advantage of such selectivity is that the statistical spread in results will actually be smaller, despite eliminating a large portion of gathered data, due to the removal of aerosol-introduced biases. Additionally, the estimates made will be more accurate, as the high power echoes are significantly less affected by absorption. Meteor observations taking into account absorptive phenomena will provide a valuable source of reliable observations to be used in conjunction with other sensors or as an absolute check of empirical models.

[23] **Acknowledgments.** We would like to express our sincere gratitude to Ray Morris and Damian Murphy of the Australian Antarctic Division for their input and the use of data collected at Davis Station, Antarctica. This research was conducted with financial support from ASAC grant 2529 and ARC grant DP450787.

References

Amyx, K., Z. Sternovsky, S. Knappmiller, S. Robertson, M. Horanyi, and J. Gumbel (2007), In-situ measurement of smoke particles in the wintertime mesosphere between 80 and 85 km altitude, *J. Atmos. Sol. Terr. Phys.*, *70*, 61–70.

Cervera, M. A., and I. M. Reid (2000), Comparison of atmospheric parameters derived from meteor observations with CIRA, *Radio Sci.*, *35*, 833–843.

Chilson, P. B., P. Czechowsky, and G. Schmidt (1996), A comparison of ambipolar diffusion coefficients in meteor trains using VHF radar and UV lidar, *Geophys. Res. Lett.*, *23*, 2745–2748.

Cho, J. Y. N., C. M. Alcala, M. C. Kelley, and W. E. Swartz (1994), Further effects of charged aerosols on summer mesospheric radar scatter, *J. Atmos. Sol. Terr. Phys.*, *58*, 661–672.

Dyrud, L. P., M. M. Oppenheim, and A. F. vom Endt (2001), The anomalous diffusion of meteor trails, *Geophys. Res. Lett.*, *28*, 2775–2778.

Havnes, O., and F. Sigernes (2005), On the influence of background dust on radar scattering from meteor trails, *J. Atmos. Sol. Terr. Phys.*, *67*, 659–664.

Holdsworth, D. A., I. M. Reid, and M. A. Cervera (2004), Buckland Park all-sky interferometric meteor radar, *Radio Sci.*, *39*, RS5009, doi:10.1029/2003RS003014.

Holdsworth, D. A., D. J. Murphy, I. M. Reid, and R. J. Morris (2008), Antarctic meteor observations using the Davis MST and meteor radars, *Adv. Space Res.*, *42*(11), 143–154.

Jones, W. (1995), Theory of the initial radius of meteor trains, *Mon. Not. R. Astron. Soc.*, *275*, 812–818.

McKinley, D. W. R. (1961), Meteor Science and Engineering, pp. 186–212, McGraw-Hill, New York.

Natanson, G. L. (1960), On the theory of the charging of amicroscopic aerosol particles as a result of capture of gas ions, *Sov. Phys. Tech. Phys., Engl. Transl.*, *5*, 538–551.

Rapp, M. (2000), Capture rates of electrons and positive ions by mesospheric aerosol particles, *J. Aerosol Sci.*, *31*(11), 1367–1369.

Singer, W., R. Latteck, L. F. Millan, N. J. Mitchell, and J. Fiedler (2008), Radar backscatter from underdense meteors and diffusion rates, *Earth Moon Planets*, *102*, 403–409.

Tsutsumi, M., T. Tsuda, and T. Nakamura (1994), Temperature fluctuations near the mesopause inferred from meteor observations with the middle and upper atmosphere radar, *Radio Sci.*, *29*, 599–610.

D. A. Holdsworth, ATRAD Pty. Ltd., 1/26 Stirling Street, Thebarton, SA 5013, Australia.

R. A. Vincent, I. M. Reid, and J. P. Younger, Department of Physics, University of Adelaide, Adelaide, SA 5005, Australia. (joel.younger@adelaide.edu.au)

Appendix C

Published Paper: Mon. Not. R. astr. Soc., 398: 350-356, 2009

J. P. Younger, I. M. Reid, R. A. Vincent, D. A. Holdsworth and D. J. Murphy. (2009)
A southern hemisphere survey of meteor shower radiants and associated stream orbits using single station radar observations.
Monthly notices of the Royal Astronomical Society, v. 398 (1), pp. 350-356, September 2009

Bibliography

H. H. Andersen and H. L. Bay. Sputtering yield measurements. In *Sputtering by Particle Bombardment*. Springer, Berlin, 1981.

D. Anderson, L. Smith, and J. Gruszynski. S-parameter techniques for faster, more accurate network design. Test & Measurement Application Note 95-1, Hewlett-Packard Company, 1997.

E. V. Appleton. On some measurements of the equivalent height of atmospheric ionized layers. *Proc. Roy. Soc.*, A126:542–569, 1930.

J. Baggaley. Meteoric ionization: the interpretation of radar trail echoes. *Radio Sci. Bulletin*, 329:6–20, 2009.

W. J. Baggaley. Determination of the initial radii of meteor trains. *Mon. Not. R. astr. Soc.*, 147:231–243, 1970.

W. J. Baggaley and T. H. Webb. Measurements of the ionization heights of sporadic radio-meteors. *Mon. Not. R. Astr. Soc.*, 191:829–839, 1980.

W. J. Baggaley, R. G. T. Bennett, D. I. Steel, and A. D¿ Taylor. The advanced meteor orbit radar facility: AMOR. *Q. J. R. astr. Soc.*, 35:293–320, 1994.

W. J. Baggaley, R. G. T. Bennett, and A. D. Taylor. Radar meteor atmospheric speeds determined from echo profile measurements. *Planet. Space Sci.*, 45(5):577–583, 1997.

C. A. Balanis. *Antenna Theory Analysis and Design Third Edition*. Wiley-Interscience, 2005.

P. M. S. Blackett and A. C. B. Lovell. Radio echoes and cosmic ray showers. *Proc. R. Soc. London*, 177:183–186, 1941.

J. Bohdansky. A universal relation for the sputtering yields of monoatomic solids at normal incidence. *J. Nuc. Instrum. Methods B*, 2:587–591, 1984.

J. Bohdansky, J. Roth, and H. L. Bay. An analytical formula and important parameters for low-energy ion sputtering. *J. Appl. Phys.*, 51:2861–2865, 1980.

V. A. Bronshten. *Physics of Meteoric Phenomena.* D. Reidel Pub. Co., 1983.

P. Brown, R. J. Weryk, D. K. Wong, and J. Jones. A meteoroid stream survey using the canadian meteor orbit radar: I. methodology and radiant catalogue. *Icarus*, 195 (1):317–339, 2008.

M. D. Campbell-Brown and J. Jones. Determining the initial radius of meteor trains: fragmentation. *Mon. Not. R. Astron. Soc.*, 343:775–780, 2003.

M. D. Campbell-Brown and D. Koschny. Model of the ablation of faint meteors. *Astron. Astrophys.*, 418(2):751–758, 2004.

Z. Ceplecha, J. Borovička, W. G. Elford, D. O. ReVelle, R. L. Hawkes, V. Porubčan, and M. Šimek. Meteor phenomena and bodies. *Space Sci. Rev.*, 84(3-4):327–471, 1998.

M. A. Cervera and I. M. Reid. Comparizon of atmospheric parameters derived from meteor observations with CIRA. *Radio Sci.*, 35(3):833–843, 2000.

J. Y. N. Cho, C. M. Alcala, M. C. Kelley, and W. E. Swartz. Further effects of charged aerosols on summer mesospheric echoes. *J. Atmos. Sol.-Terr. Phys.*, 58: 661–672, 1994.

V. A. Chobotov. *Orbital Mechanics Third Edition.* American Institute of Aeronautics and Astronautics, Reston, 2002.

B. Clemesha and P. Batista. The quantification of long-term atmospheric change via meteor ablation height measurements. *J. Atmos. Sol.-Terr. Phy.*, 68:1934–1939, 2006.

A. F. Cook. A working list of meteor streams. In *Proc. IAU Colloq. 13, Evolutionary and Physical Properties of Meteoroids, NASA SP-319*, 1973.

S. G. Coulson. Resistance of motion to a small hypervelocity sphere, sputtering through a gas. *Mon. Not. R. Astron. Soc*, 332:741–744, 2002.

B. T. Draine and E. E. Salpeter. On the physics of dust grains in hot gas. *Astrophys. J.*, 231:77–94, 1979.

B. T. Draine and B. Sutin. Collisional charging of interstellar grains. *Astrophys. J.*, 320:803–817, 1987.

L. P. Dyrud, M. M. Oppenheim, and A. F. vom Endt. The anomalous diffusion of meteor trails. *Geophys. Res. Lett.*, 28(14):2775–2778, 2001.

T. L. Eckersley. Irregular ionic clouds in the e-layer of the ionosphere. *Nature*, 140: 846–847, 1937.

W. G. Elford. Radar observations of meteor trails, and their interpretation using fresnel holography: a new tool in meteor science. *Atmos. Chem. Phys.*, 4:911–921, 2004.

W. G. Elford. Observations of the structure of meteor trails at radio wavelengths using fresnel holography. In *Proceedings of the Meteoroids 2001 Conference*, pages 405–411, Kiruna, Sweden, 2001. Swedish Institute of Space Physics.

W. G. Elford and L. Campbell. Effects of meteoroid fragmentation on radar observations of meteor trails. In *Proceedings of the Meteoroids 2001 Conference*, pages 419–423, Kiruna, Sweden, 2001. Swedish Institute of Space Physics.

C. D. Ellyett and J. A. Kennewell. Radar meteor rates and atmospheric density changes. *Nature*, 287:521–522, 1980.

E. Grün, A. Zook, H Fechtig, and R. H. Giese. Collisional balance of the meteoritic complex. *Icarus*, pages 244–272, 1985.

M. Harwit. *Astrophysical Concepts*. Wiley, New York, 1973.

O. Havnes and F. Sigernes. On the influence of background dust on radar scattering from meteor trails. *J. Atmos. Sol-Terr. Phys.*, 67:659–664, 2005.

N. Herlofson. The theory of meteor ionization. *Rep. Prog. Phys.*, 11:444–454, 1947.

R. J. Hill. Nonneutral and quasi-neutral diffusion of weakly ionized multiconstituent plasma. *J. Geophys. Res.*, 83, 1978.

W. K. Hocking, T. Thayaparan, and J. Jones. Meteor decay times and their use in determining a diagnostic mesospheric temperature-pressure parameter: methodology and one year of data. *Geophys. Res. Lett.*, 23:2977–2980, 1997.

D. A. Holdsworth. Angle of arrival estimation for all-sky interferometric meteor radar systems. *Radio Sci.*, 40(RS6010), 2005.

D. A. Holdsworth, I. M. Reid, and M. A. Cervera. Buckland park all-sky interferometric meteor radar. *Radio Sci.*, 39(RS5009), 2004a.

D. A. Holdsworth, M. Tsutsumi, I. M. Reid, T. Nakamura, and T. Tsuda. Interferometric meteor radar phase calibration using meteor echoes. *Radio Sci.*, 39(RS5012), 2004b.

D. A. Holdsworth, I. M. Reid, D. J. Murphy, and R. J. Morris. Meteor radar temperature estimation using the davis mst and meteor radars. In *As presented at the MST-11 conference in Gadanki, India*, 2006.

D. A. Holdsworth, W. G. Elford, R. A. Vincent, I. M. Reid, D. J. Murphy, and W. Singer. All-sky interferometric meteor radar meteoroid speed estimation using the fresnel transform. *Ann. Geophys.*, 25:385–398, 2007.

D. A. Holdsworth, D. J. Murphy, I. M. Reid, and R. J. Morris. Antarctic meteor observations using the davis MST and meteor radars. *Adv. Space Res.*, 42(1):143–154, 2008.

J. T. Houghton. *The Physics of Atmospheres.* Cambridge University Press, Cambridge, 1977.

D. M. Hunten, R. P. Turco, and O. B. Toon. Smoke and dust particles of meteoric origin in the mesosphere and stratosphere. *J. Atmos. Sci.*, 37:1342–1357, 1980.

IAU. IAU Meteor Data Center. `http://www.ta3.sk/IAUC22DB/MDC2007/`. maintained by the Astronomical Institute of the Slovak Academy of Sciences.

International Meteor Organization. 2007 meteor shower calendar. `http://www.imo.net/calendar`, 2007. compiled by A. McBeath.

P. Jenniskens. Meteor stream activity I. the annual streams. *Astron. Astrophys.*, 287: 990–1013, 1994.

J. Jones and P. Brown. The radiant distribution of sporadic meteors. *Planet. Space Sci.*, 42:123–213, 1994.

J. Jones and W. Jones. Meteor radiant activity mapping using single-station radar observations. *Mon. Not. R. Astron. Soc.*, 367:1050–1056, 2006.

J. Jones, A. R. Webster, and W. K. Hocking. An improved interferometer design for use with meteor radars. *Radio Sci.*, 33(1):55–65, 1998.

J. Jones, P. Brown, K. J. Ellis, A. R. Webster, M. D. Campbell-Brown, and Z. Krzemenski amd R. J. Weryk. The canadian meteor orbit radar (CMOR): System overview and preliminary results. *Planet. Space Sci.*, 53:413–421, 2005.

W. Jones. Theoretical and observational determination of the ionization coeffcient of meteors. *Mon. Not. R. Astron. Soc.*, 288:995–1003, 1997.

W. Jones. Theory of diffusion of meteor trains in the geomagnetic field. *Planet. Space Sci.*, 39(9):1283–1288, 1991.

W. Jones. Theory of the initial radius of meteor trains. *Mon. Not. R. Astron. Soc.*, 275:812–818, 1995.

T. R. Kaiser. Radio echo studies of meteor ionization. *Adv. Phys.*, 2(8):495–544, 1953.

S. Kakaç and Y. Yener. *Heat Conduction.* Hemisphere, New York, 1985.

M. C. Kelley, C. Alcala, and J. Y. N. Cho. Detection of a meteor contrail and meteoric dust in the earth's upper mesosphere. *J. Atmos. Sol-Terr. Phys.*, 60(3):359–369, 1998.

S. Knappmiller, M. Rapp, S. Robertson, and J. Gumbel. Charging of meteoric smoke and ice particles in the mesosphere including photoemission and photodetachment rates. *J. Atmos. Sol-Terr. Phys.*, 73(14-15):2212–2220, 2011.

Y. Kozai. Secular perturbations of asteroids with high inclination and eccentricity. *Astrophys. J.*, 67(9):591–598, 1962.

G. W. Kronk. Meteor Showers Online. `http://meteorshowersonline.com/`.

G. W. Kronk. *Meteor showers: a descriptive catalog.* Enslow Publishers, Hillside, 1988.

E. Kudeki and R. F. Woodman. A poststatistics steering technique for MST radar applications. *Radio Sci.*, 25(4):591–594, 1990.

I. Langmuir. The vapor pressure of metallic tungsten. *Phys. Rev.*, 11(5), 1913.

B. A. Lindbald. Meteor radar rates and the solar cycle. *Nature*, 259:99–101, 1976.

S. G. Love and D. E. Brownlee. Heating and thermal transformation of micrometeoroids entering the earth's atmosphere. *Icarus*, 89:26–43, 1991.

A. C. B. Lovell and J. A. Clegg. Characteristics of radio echoes from meteor trails: I. the intensity of the radio reflections and electron density in the trails. *Proc. Phys. Soc.*, 60:491–498, 1948.

F. J. Lübken, A. Müllemann, and M. J. Jarvis. Temperatures and horizontal winds in the antarctic summer mesosphere. *J. Geophys. Res.*, 109, 2004.

W. Magnus and F. Oberhettinger. *Formulas and Theorems for the Special Functions of Mathematical Physics.* Chelsea Pub. Co., New York, 1949.

L. A. Manning. The initial radius of meteoric ionization trails. 63(1):181–196, 1958.

H. S. Massey and S. D. Sida. Collision processes in meteor trails. 46:190, 1955.

H. S. W. Massey, E. H. S. Burhop, and H. B. Gilbody. *Electronic and Ionic Impact Phenomena Vol. III.* Clarendon Press, London, 1971.

A. Matsunami, Y. Yamamura, Y. Itikawa, N. Itoh, N. Kazumata, S. Miyagawa, K. Morita, and R. Shimizu. A semiempirical formula for the energy dependence of the sputtering yield. *Radiat. Eff. Lett.*, 57:15–21, 1980.

B. A. McIntosh and A. Hajduk. Comet halley meteor stream - a new model. *Mon. Not. R. astr. Soc.*, 205:931–943, 1983.

D. W. R. McKinley. *Meteor Science and Engineering.* McGraw-Hill, New York, 1961.

L. Megner, M. Rapp, and J. Gumbel. Distribution of meteoric smoke - sensitivity to microphysical properties and atmospheric conditions. *Atmos. Chem. Phys.*, 6: 4415–4426, 2006.

J. D. Morton and J. Jones. A method for imaging radio meteor radiant distributions. *Mon. Not. R. astr. Soc.*, 198:737–746, 1982.

H. Nagaoka. Possibility of disturbance of radio transmissions by meteoric showers. *Proc. Imp. Acad. Tokyo*, 5:233, 1929.

E. J. Öpik. *Physics of Meteor Flight in the Atmosphere.* Interscience Publishers Inc., New York, 1958.

F. I. Peregudov. On the effect of meteor velocities on the hour number in radio-echo detection of meteors. *Soviet Astr.*, 2:833–838, 1958.

J. M. Picone, A. E. Hedin, D. P. Drob, and A. C. Akin. NRLMSISE-00 empirical model of the atmosphere: Statistical comparisons and scientific issues. *J. Geophys. Res.*, 107(A12):1468, 2002.

J. A. Pierce. Abnormal ionization in the e region of the ionosphere. *Proc. Inst. Radio Engn.*, 26:892–908, 1938.

Y. I. Portnyagin. Effective diffusion cross section of meteoric atoms in the atmosphere. *Geomagn. and Aeron.*, 6:540–543, 1966.

Y. I. Portnyagin and V. S. Tokhtasyev. Effective diffusion cross section of meteor atoms and ions in the atmosphere for an extended region of interaction energies. *Geomagn. and Aeron.*, 14:67–71, 1974.

M. Rapp. Capture rates of electrons and positive ions by mesospheric aerosol particles. *J. Aerosol Sci.*, 31, 2000.

F. J. M. Rietmeijer. Interplanetary dust and carbonaceous meteorites: constraints on porosity, mineralogy, and chemistry of meteors from rubble-pile planitesimals. *Earth Moon Planets*, 95:321–338, 2004.

L. A. Rogers, K. A. Hill, and R. L. Hawkes. Mass loss due to sputtering and thermal processes in meteoroid ablation. *Plan. Space Sci.*, 53:1341–1354, 2005.

T. R. Scavo and J. B. Thoo. On the geometry of Halley's method. *Am. Math. Mon.*, 102(5), 1995.

P. Sigmund. Theory of sputtering. I. sputtering yield of amorphous and polycrystaline targets. *Phys. Rev.*, 184(2), 1969.

A. M. Skellet. The effect of meteors on radio transmission through the kennelly-heavyside layer. *Phys. Rev.*, 37:1668, 1935a.

A. M. Skellet. The ionizing effect of meteors. *Proc. Inst. Radio Engn.*, 23:132–149, 1935b.

D. I. Steel and W. G. Elford. The height distribution of radio meteors: comparison of observations at different frequencies on the basis of standard echo theory. *J. Atmos. Terr. Phys.*, 53(5):409–417, 1991.

A. G. G. M. Tielens, C. F. McKee, C. G. Seab, and D. J. Hollenbach. The physics of grain-grain collisions and cas-grain sputtering in interstellar shocks. *Astrophys. J.*, 431:321–340, 1994.

F. Verniani. An analysis of the physical parameters of 5759 faint radio meteors. *J. Geophys. Res.*, 78(35):8429–8462, 1973.

R. A. Vincent, S. Kovalam, I. M. Reid, and J. P. Younger. Gravity wave flux retrievals using meteor radars. 37(L14802):1–5, 2010.

T. Vondrak, J. M. C. Plane, S. Broadley, and D. Janches. A chemical model of meteoric ablation. *Atmos. Chem. Phys.*, 8:7015–7031, 2008.

A. Voors. NEC based antenna modeler and optimizer. `http://home.ict.nl/ arivoors/`.

R. A. Watson Watt, A. F. Wilkins, and E. G. Bowen. The return of radio waves from the middle atmosphere. *Proc. Roy. Soc.*, A161:181–196, 1937.

S. P. Wyatt and F. L. Whipple. The poynting-robertson effect on meteor orbits. *Astrophys. J.*, 111:134–141, 1950.

J. P. Younger, I. M. Reid, R. A. Vincent, and D. A. Holdsworth. Modeling and observing the effect of aerosols on meteor radar measurements of the atmosphere. *Geophys. Res. Lett.*, 35(L15812):1–4, 2008.

J. P. Younger, I. M. Reid, R. A. Vincent, D. A. Holdsworth, and D. J. Murphy. A southern hemisphere survey of meteor shower radiants and associated stream orbits using single station radar observations. *Mon. Not. R. astr. Soc.*, 398:350–356, 2009.

“In closing, gentle reader, I’d like to thank you. ‘Whats that?’ you say? Me thanking you? No, it’s not a misprint, for you see, I enjoyed writing this book as much as you enjoyed reading it. The End.”

Charles Montgomery Burns
Will There Ever Be A Rainbow?